

Katholieke Universiteit Leuven

**Groep Biomedische Wetenschappen en
Groep Wetenschap en Technologie**

Departement Tandheelkunde, Mondziekten en Kaakchirurgie

Centrum voor Orale Beeldvorming

Departement Elektrotechniek (ESAT)

Afdeling ESAT-PSI, Centrum voor Spraak- en Beeldverwerking

Departement Medisch Diagnostische Wetenschappen

Afdeling Radiologie



Geometrical and dosimetical aspects of low-dose CT in dentomaxillofacial radiology

Miet LOUBELE

Jury:

Promotor: Prof dr. R. Jacobs

Copromotor: Prof dr. ir. P. Suetens, Prof. dr. R. Hermans

Voorzitter: Prof. A. De Laat

Secretaris: Prof. dr. ir. F. Maes

Leden: Prof. dr. P. Demaerel,

Prof. dr. H. Thierens, (Ugent),

Prof. dr. P. van der Stelt (ACTA Amsterdam)

Leuven, 17 september 2008

Doctoraal proefschrift in de Medische Wetenschappen

© Katholieke Universiteit Leuven – Faculteit Ingenieurswetenschappen en Geneeskunde
Kasteelpark Arenberg 10, B-3001 Heverlee (Belgium)

Alle rechten voorbehouden. Niets uit deze uitgave mag worden vermenigvuldigd en/of openbaar gemaakt worden door middel van druk, fotokopie, microfilm, elektronisch of op welke andere wijze ook, zonder voorafgaande schriftelijke toestemming van de uitgever.

All rights reserved. No part of this publication may be reproduced in any form by print, photo print, microfilm or any other means without permission from the publisher.

ISBN 978-90-5682-974-2
Wettelijk depot D/2008/7515/84

Voor mijn boma, Guillaume Loubele

Dankwoord

Ik zou van deze gelegenheid willen gebruik maken om iedereen te bedanken die op welke wijze dan ook heeft bijgedragen tot de goede afloop van dit werk. Allereerst wil ik prof. Paul Suetens bedanken die mij de mogelijkheid bood om te werken in de groep Medische Beeldverwerking en om copromotor te zijn van dit proefschrift. Verder wil ik prof. Reinilde Jacobs danken om promotor te zijn van dit eindwerk en prof. Robert Hermans om copromotor te zijn van dit eindwerk. Prof. Antoon De Laat om voorzitter te zijn van mijn jury en prof. Paul van der Stelt, prof. Hubert Thierens, prof. Philippe Demaerel, en prof. Frederik Maes om deel uit te maken van mijn jury en voor het grondig nalezen van mijn tekst. Mijn dank gaat ook naar prof. Dirk Vandermeulen, wijlen prof. Johan Van Cleynenbreugel, Dominique Delaere, Bart De Dobbelaer, Annitta Demessemaeker, Patricia Waeghe, Stijn De Buck, Dirk Loeckx, Pieter Bruyninckx, Johannes Keustermans, Maarten Depypere, Gert Merckx, Lennart Scheys, An Elen, Janaki Raman, Dieter Seghers, Thomas Fabry, Annemie Ribbens, Dirk Smeets, Jeroen Hermans, Liesbet Roose, Pieter De Groeve, Filip Schutyser, Kris Verstreken, Wouter Mollemans, Kevin Suetens, Tinne Van Delm, Gabriel Kiss, Yves Lambelin, Peter Claes, Qian Wang, Emiliano D'Agostino, Gert Peeters, Jeroen Wouters, Sven De Greef, Siddy Srivastava en Frederik De Keyzer: de huidige en vroegere onderzoekers van de groep Medische Beeldverwerking.

Bij dit doctoraat heb ik echter niet alleen samen gewerkt met mensen van mijn eigen onderzoeksgroep maar ook met mensen van verschillende andere groepen. Daarom gaat mijn dank ook naar Walter Coudyzer van radiologie voor de vele scansessies. Philip Coudzos en Herman Pauwels, voor de snelle reacties op de mails gericht naar Pacsrad. Prof. Ria Bogaerts en prof. Hilde Bosmans bij de hulp in het bepalen van de dosimetrie. De medewerkers Olivia Nackaerts, Maria Eugenia Guerrero, Liang Xiang en Roland Vanderbiesen van het Oral Imaging Center, prof. Daniel van Steenberghe en Jurgen Jacobs, Koen Michielsen, Kim Lemmens, Joris Nens, Frederica Zanca, Octavian Dragusin, Kristien Smans en Ann-Catherine Carton van het LUCMFR wil ik ook danken. Kathleen Denis van de Xios Hogeschool Limburg, Ivo Lambrichts van de Universiteit Hasselt en Christian Lamoral wil ik ook bedanken.

Special thanks also goes out to prof. Stuart White of the UCLA for giving me the possibility to stay at the ULCA to perform more experiments. I also would like to thank Eric T. Iwamoto of the Golden State X-ray Lab, Willia, Cambell of SmartScan Imaging (Orange, California, USA) for the use of their MercuRay, Arun Singh and the employees of Imaging Sciences for the use of their i-CAT during my stay at their factory and George Zuni-ga of the technical service department of the School of Dentistry at UCLA .

Tenslotte wil ik ook nog mijn ouders, familie, vrienden en mijn vriend bedanken Yves voor de steun tijdens mijn doctoraat.

Table of contents

Dankwoord	7
Table of contents	9
Preface.....	11
Glossary	13
 Chapter 1 Introduction.....	 15
1.1 The use of 3-D imaging in oral rehabilitation	15
1.2 Cone-Beam Computed Tomography.....	16
1.3 CBCT scanners in dentomaxillofacial radiology.....	24
1.4 Radiation dose	28
1.5 State-of-the-art of validation of bone related image measurements	30
1.6 Main contribution of this thesis	32
 Chapter 2 Radiation dose versus image quality for low-dose CT protocols of the head for maxillofacial surgery and oral implant planning.....	 35
2.1 Abstract	35
2.2 Introduction	36
2.3 Material and methods	36
2.4 Results	42
2.5 Discussion	45
2.6 Conclusion.....	46
 Chapter 3 Assessment of bone segmentation quality of cone-beam CT versus multi-slice spiral CT: a pilot study.....	 47
3.1 Abstract	47
3.2 Introduction	48
3.3 Material and methods	48
3.4 Results	54
3.5 Discussion	57
3.6 Conclusion.....	61
 Chapter 4 Assessment of bone segmentation quality of CT scanners using laser scanning	 63
4.1 Abstract	63
4.2 Introduction	63
4.3 Material and Methods.....	64
4.4 Results	68
4.5 Conclusion.....	68
 Chapter 5 Geometric accuracy and radiation dose in 3-D scanners in dentomaxillofacial radiology	 71
5.1 Abstract	71
5.2 Introduction	71
5.3 Material and Methods.....	73
5.4 Results	88
5.5 Discussion and conclusion	98

Chapter 6 Discussion	101
6.1 Technology of CBCT scanners	101
6.2 Evaluation of methods for dose measurements	103
6.3 Choice for an optimal threshold value.....	104
6.4 Evaluation of the different phantoms	106
6.5 Clinical implications	110
Chapter 7 Summary	117
Chapter 8 Samenvatting.....	121
References.....	125
Curriculum Vitae	131
List of Publications	131

Preface

This thesis is based on the following papers

Chapter 2:

Loubele M., Jacobs R., Maes F., Schutyser F., Debaveye D., Bogaerts R., Coudyzer W., Vandermeulen D., Van Cleynenbreugel J., Marchal G., Suetens P., 2005 Radiation dose versus image quality for low-dose CT protocols of the head for maxillofacial surgery and oral implant planning *Radiat Prot Dosimetry* **117** 211-216

Chapter 3:

Loubele M., Maes F., Schutyser F., Marchal G., Jacobs R., Suetens P. 2006 Assessment of bone segmentation quality of cone-beam CT versus multi-slice spiral CT: a pilot study *Oral Surg Oral Med Oral Pathol Oral Radiol Endo.* **102** 225-34

Chapter 4:

Loubele M., Maes F., Vandermeulen D., Denis K., Jacobs R., White SC., van Steenberghe D., Van Bael A., Loeckx D., Lambrichts I., Suetens P. 2006 Assessment of bone segmentation quality of CT scanners using laser scanning *International journal of computer assisted radiology and surgery*, **1** supplement, 400-402, June 2006 (20th international congress and exhibition on computer assisted radiology and surgery - CARS 2006, June 28 - July 1, 2006, Osaka, Japan)

Chapter 5:

Loubele M., Bogaerts R., White SC, Maes F., Bosmans H., Sanderink G., Jacobs R., Coudyzer W., Marchal G., Suetens P. 2007 Comparative study of image quality and radiation dose of MSCT and CBCT scanners in dentomaxillofacial radiology, *Internal report KUL/ESAT/PSI/0703*, K.U.Leuven, ESAT, February 2007, Leuven, Belgium

Loubele M., Maes F., Jacobs R., van Steenberghe D., White SC, Suetens P. 2008 Comparative study of image quality for MSCT and CBCT scanners for dentomaxillofacial radiology applications *Radiat Prot Dosimetry*, **129** 222-226

Glossary

1-D	One-dimensional
2-D	Two-dimensional
3-D	Three-dimensional
AEC	Automatic Exposure Control
A-Si	Amorpheous Silicon
CBCT	Cone-Beam computed tomography
CCD	Charged Coupled Device
CNR	Contrast to Noise Ratio
CT	Computed Tomography
CTDI	Compted Tomography Dose Index
D	Organ dose
D_i	Mean dose of an organ situated in slice i of the Rando Alderson phantom
DICOM	Digital Imaging and Communications in Medicine
ESP	European Spine Phantom
f_i	Fraction of an organ situated in slice i of the Rando Alderson phantom
FOV	Field Of View
FPD	Flat Panel Detector
FWHM	Full width at half maximum
FWTM	Full width at tenth maximum
HU	Hounsfield Unit
ICRP	International Commission on Radiation Protection
kV	Kilovoltage
kVp	Kilovoltage peak
LiF	Lithium Fluoride
mA	Miliampere
mAs	Miliampere x seconds
MMI	Maximisation of mutual information
MSCT	Multi-Slice Computed Tomography
MTF	Modular Transfer Function
PSF	Point Spread Function
SEM	Stochastic Expectation Maximisation
TLD	Thermoluminescent Dosemeter
μ_A	Linear attenuation coefficient
W_T	Tissue weighting factor. Not every organ is as sensitive for the effects of radiation. Organs that are more sensitive to radiation have a higher tissue-weighting factor. The sum of all W_T is 1.

Chapter 1

Introduction

1.1 The use of 3-D imaging in oral rehabilitation

In oral implant surgery, small titanium screws are inserted in the jawbone. On these endosseous implants, a prosthetic suprastructure is mounted. This technique provides a good rehabilitation for edentulous patients, on the condition that good osseointegration is obtained. Thereto a good surgical technique is needed, taking into account quality and quantity of the available bone as well as biomechanical and aesthetical aspects. There are also vulnerable anatomical structures in the jaw that have to be avoided at all cost, such as the alveolar nerve in the mandible. Consequently a thorough preoperative planning is mandatory to perform a successful surgery (Verstreken 2003).

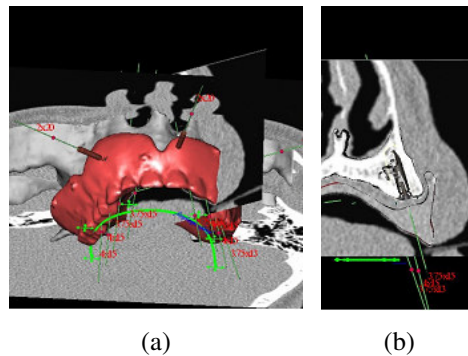


Figure 1.1 Example of dedicated software for the placement of oral implants: reformatted 3-D slices together with a bone model and a model of the prosthesis are shown. (Courtesy Filip Schutyser, Medicim NV, Sint-Niklaas, Belgium)

To make this planning there is the tendency is to use three-dimensional (3-D) radiographic images (Verstreken *et al* 1996 and Suetens *et al* 2002). For the manipulation of these 3-D images dedicated software has been developed (Figure 1.1). With such software reformatted images or slices perpendicular to the alveolar ridge can be calculated. Besides these reformatted images, a bone model derived from the 3-D images can be shown. This model is derived from the 3-D images using a segmentation algorithm for extracting the bony tissues and applying the marching cubes algorithm (Lorensen and Cline, 1987) for generating a triangulated model of the bone surface. With the aid of the

3-D bone model and the reformatted images, the clinician can determine the number of implants and the position of these implants. To determine the appropriate position of the implants it is important that the derived bone models are very accurate and that the clinician can perform accurate measurements of the bone thickness at various places. Therefore, it is important that the scanners provide accurate images.

Initially conventional single and later, multi-slice computed tomography (MSCT) scanners were used (Gahleitner *et al* 2003) for the planning of oral implants. Nevertheless, there are some constraints for the widespread use of MSCT in oral implant planning. These are the relatively high radiation dose (Cohnen *et al* 2002) that is involved with the acquisition of such images and the long waiting lists for dental CT scans. Therefore alternative CT protocols for bone visualization and modelling that would lower the effective radiation dose for the patient, without significant loss of image quality were being explored. Examples of these alternatives are modified protocols on MSCT scanners (Hein *et al* 2002, Imhof *et al* 2003a) or the introduction of other hardware, such as the cone-beam CT (CBCT) (Guerrero *et al* 2006, Scarfe *et al* 2006). The introduction of the CBCT has revolutionized the way images are taken in dentomaxillofacial imaging. The manufacturers claim that these scanners offer images acquired at a lower radiation dose than conventional CT but with the possibility for the clinician to design a good pre-operative plan for the placement of oral implants. This hypothesis will be tested in this thesis.

1.2 Cone-Beam Computed Tomography

1.2.1 Introduction

In this paragraph the principle of CBCT scanners is explained together with some important parameters that determine the accuracy of image based measurements in images derived from CBCT scanners. Some of these parameters are determined by the design of the machine and other parameters can be changed according to the used protocol for imaging the patient. Due to the limitations of the hardware of the scanner and the limitations of the reconstruction algorithm, some features might arise in the images that are not present in the object that is imaged. These features are denoted artefacts and will be further studied in the last part of this section.

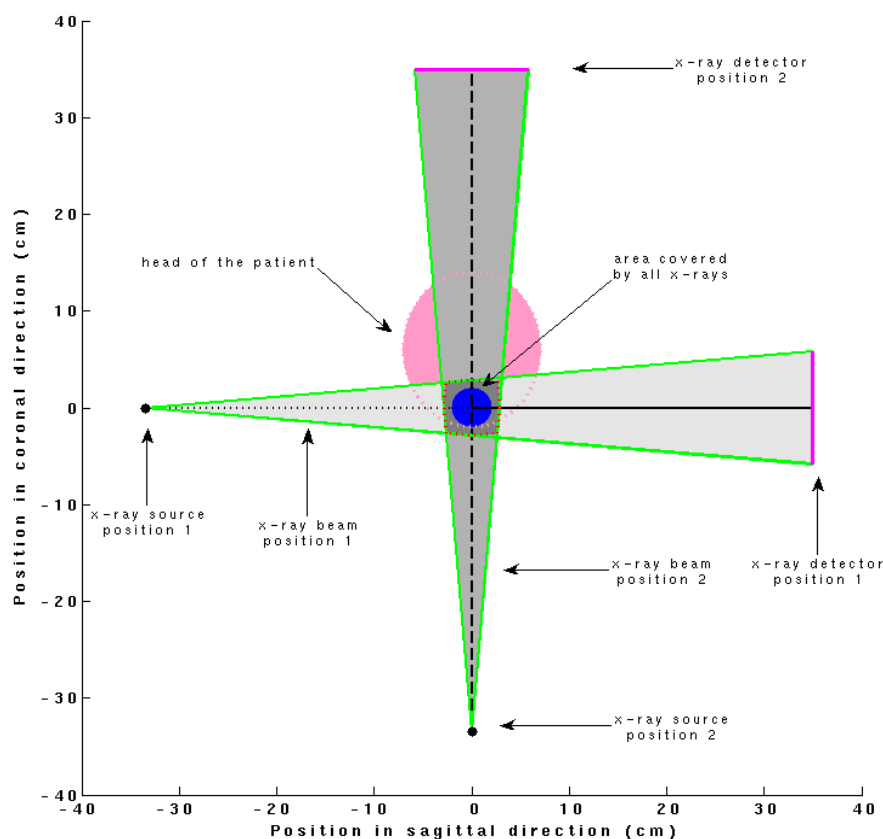


Figure 1.2 Illustration of the geometry of the Accuitomo 3D CBCT scanner (Morita, Kyoto, Japan).

1.2.2 Principle

In Figure 1.2, the principle of a CBCT scanner is explained based on an axial plane through the head of the patient. Both an X-ray source and a detector are fixed on a rotating gantry. The X-ray source may release X-rays on a continuous or a pulsed way. During the exposure of the X-rays, the gantry will rotate. This makes it possible for the detector to collect basis images, which can be seen as radiographs taken at different angles. After the collection of all the base images, a reconstruction algorithm calculates a 3-D volume. It should be noted that not the complete part of the head that is exposed will be shown in the final image. Due to a combination of the size of X-ray beam and positioning of the X-ray beam to the patient, it will be possible to acquire different sizes of Field of Views (FOV). In Figure 1.2, we illustrate how it may be possible to acquire only a small

FOV in the head of the patient. To illustrate this, the X-ray beam is drawn at 2 perpendicular positions. Although the X-ray beam in position 2 covers a large part of the patient's head, only a small part of the beam will be considered (see Figure 1.2) for the reconstruction of the image because the area scanned by all X-ray beams is smaller. This area is indicated by a darker shade of grey. The resulting part that is only used for the reconstruction of the 3-D volume is indicated in blue in Figure 1.2.

1.2.3 Parameters influencing accuracy of bone related measurements

1.2.3.1 Hounsfield Units

The images, which are reconstructed by the algorithm of the CT scanner, are not given by the attenuation coefficients for each point in the volume but by the CT number which is expressed in Hounsfield Units (HU). The HU of a material A are calculated with Formula 1.1. (Suetens 2002)

$$HU_A = \frac{\mu_A - \mu_{H_2O}}{\mu_{H_2O}} \cdot 1000 \quad (1.1)$$

In Formula 1.1, μ_A represents the linear attenuation coefficient of material A and μ_{H_2O} represents the linear attenuation coefficient of water. With this definition, the HU of air and water are respectively -1000 and 0. The linear attenuation coefficient depends on the energy of the X-ray beam. Because in practice the energy of an X-ray beam is not mono-energetic but consists of a continuous energy spectrum, the CT number also depends on the energy and differs for each scanner. Traditional MSCT scanners are optimised for soft-tissue imaging; the CT numbers of soft-tissue and fat do not vary (Figure 1.3) for different energies. Therefore, one can speak of one scale of HU for this kind of scanners. However, if we look at the anatomical structures, which are of interest in dentomaxillofacial imaging (Figure 1.4), one can see that the Hounsfield Units of these structures vary a lot for different energies (Figure 1.3). This implies that a global scale of HU for scanners does not exist for dentomaxillofacial imaging. A similar structure consisting of, for example, dentine can have a CT number that varies significantly depending on the energy of the X-ray beam, which depends on the kilovoltage peak (kVp) of the X-ray beam (Figure 1.3). An MSCT scanner works mostly at a kVp value of 120 kV and dental applica-

tions work at a value up to 80 kVp. This means that one has a mean energy of 60 kV for MSCT and around 40 kV for dental applications.

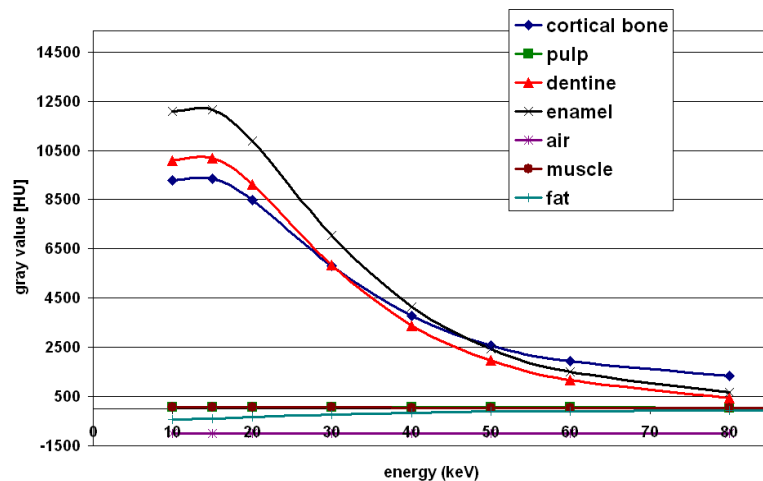


Figure 1.3 Hounsfield units for different anatomical structures. The calculations are performed based on ICRU 44, Herkströter *et al* (1990) and Hubell and Seltzer (1996).

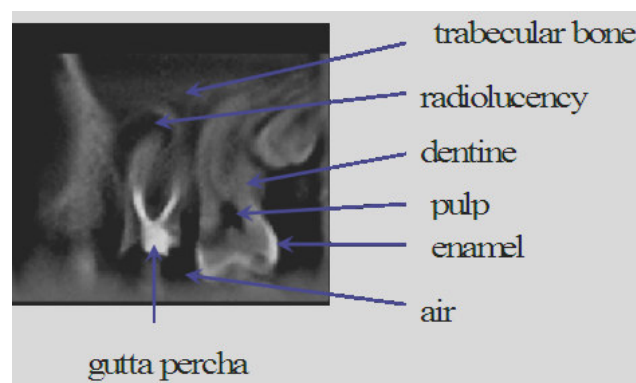


Figure 1.4 Different parts of a tooth are illustrated on a sagittal slice of the Accu-tomo 3D CBCT scanner.

1.2.3.2 Resolution

The resolution of an image gives an idea about the smallest structures that can be distinguished. The resolution should not be expressed by the voxel size but as the full width at half maximum (FWHM) and full width at tenth maximum (FWTM) of the point spread function (PSF). This PSF can, for example, be derived by imaging a phantom with a very thin wire (Figure 1.5) (Beutel *et al* 2000). The meaning of the FWHM is that if two small

dots are placed at this distance, or smaller from each other, they cannot be distinguished and are shown as one global dot (Suetens 2002).

Another way of calculating the resolution is by deriving the number of line pairs visible in a bar phantom. This is expressed by the Modular Transfer Function (MTF). A typical value for the MTF for a CT scanner is 3.5 (lp/cm) (NHS 2005) and for a CBCT scanner dedicated for dentomaxillofacial imaging is 14 lp/cm (Araki *et al* 2004). Important factors, which can influence the resolution, are the size of the beam width of the X-rays, the position in the scanned object, the sample distance and the reconstruction algorithm (Suetens *et al* 2002).

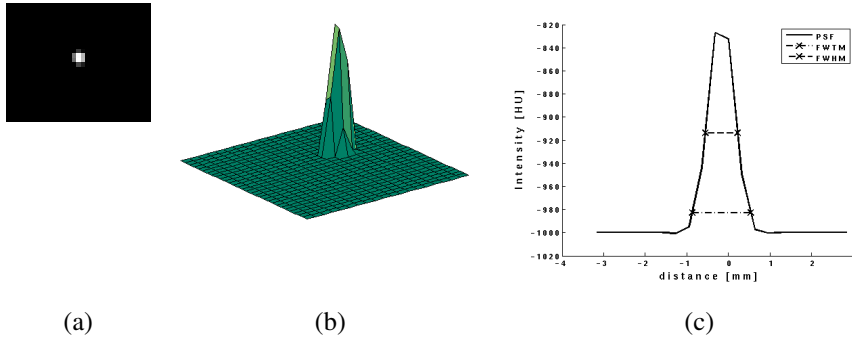


Figure 1.5 A wire is imaged as a blurred dot (a) with the PSF shown in (b). When profiles are generated out of the PSF (c), FWHM and FWTM can be calculated.

1.2.3.3 Contrast-to-Noise ratio

When a structure consisting of one material is imaged, the gray values of this structure are not all the same everywhere in the image due to image noise. The four types of noise, which can be distinguished in CT, are quantum noise, statistical noise, electric noise and round-off noise that results from the limited dynamic range of the scanner. The main contribution is from quantum noise, which is due to the statistical nature of X-rays (Suetens 2002). The contrast is the difference in the brightness between different regions. This can be calculated using the following formula:

$$C = \frac{|B_s - B_o|}{|B_o|},$$

B_o being the brightness of the smallest object and B_s is the brightness of its surroundings. When the computer processes an image, the mean intensity of a structure can be used as the brightness B_s . When a radiologist is analysing the image, environmental factors like

the darkness of the room and the display device also need to be taken into account. The contrast in CT scanners is determined by the HU and by the window level settings of the screen on which the image is visualized. The emission and detection of light and all other electromagnetic waves are stochastic processes. For image processing however, it is important how noise influences the detection of neighbouring structures. Therefore, a third quality measure is the difference in the signal-to-noise ratio (SNR_{diff}).

$$SNR_{diff} = \frac{mean(B_s - B_o)}{std(B_o)}$$

1.2.4 Image artefacts

As mentioned before the energy of an X-ray is not mono-energetic but consists of a continuous spectrum. Standard reconstruction algorithms do not take into account these physical properties of X-rays. Another shortcoming occurs in the implementation of an algorithm. For the implementation of a reconstruction algorithm in a scanner, it is only possible to take a finite number of projections into account. Due to these shortcomings, features in the reconstructed image of a scanned object that are not present in the actual object may appear. These features are called coined artefacts.

1.2.4.1 Aliasing artefacts

It is practically not achievable to acquire an infinite number of projections for the reconstruction algorithm. This under sampling can cause aliasing artefacts (Figure 1.6). This can be noticed as dark streaks in the reconstructed image. These occur due to an under sampling of the projections. If an infinite number of projections could be acquired, these could be removed. This is however not possible.

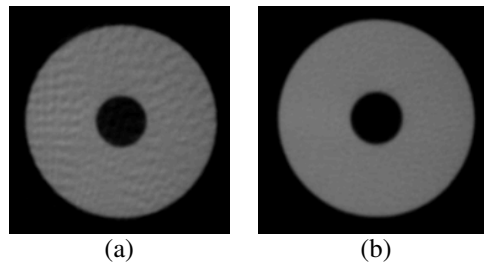


Figure 1.6 Reconstruction of an image of a phantom acquired with 166 basis images (a) and with 599 basis images (b) on the i-CAT scanner. Therefore there are more aliasing artifacts in (a) presented as dark lines.

1.2.4.2 Beam Hardening

When an X-ray passes through material, the lower energy X-ray photons are first absorbed. The resulting beam has a higher energy and therefore gets less attenuated. Therefore, the CT-number calculated by the reconstruction algorithm will be an underestimation of the real attenuation coefficient. This artefact, known as the beam hardening artefact is illustrated in Figure 1.7 (a).

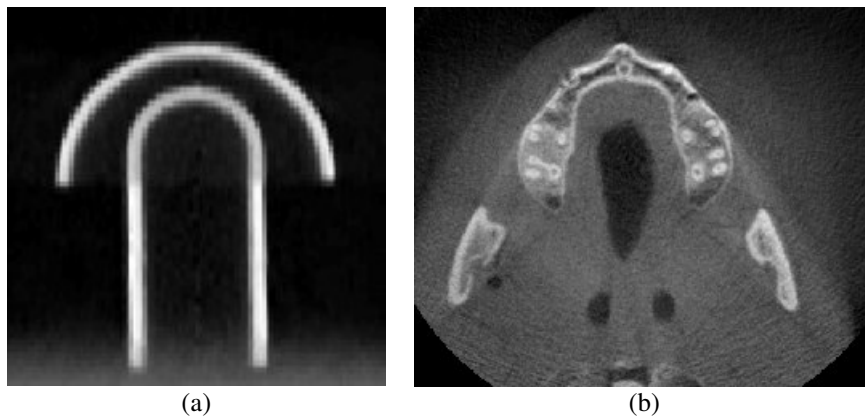


Figure 1.7 Sagittal image (a) of a phantom. This image illustrates the beam hardening artefact (a). The thin white structures should have the same intensity everywhere in the image but this is not the case due to the beam hardening artefact. Figure (b) presents the influence of scatter on imaging a phantom. Due to the scatter the border between the soft-tissue and air is not very well visible.

1.2.4.3 Scatter

Not all photons that arrive at the detector follow a straight path from the X-ray tube. Typically about 1% of the incident radiation is due to Compton scatter (Suetens 2002). Scatter also influences the CT-number; due to the scatter the attenuation coefficients will be underestimated. In CBCT, this phenomenon will produce an intensity inhomogeneity of the CT-number (Carlsson 1999), (Figure 1.7 (b)). Also the cupping artefact and reduced contrast detect ability can be noticed. Due to the larger size of the detector and the larger size of the X-ray beam in CBCT in relation to MSCT, there is more scatter in CBCT images. However this is not a major issue in dentomaxillofacial radiology, because the focus is in high-contrast anatomy like the interfaces between bone, soft-tissue

and not the low-contrast anatomy like the differentiation between different soft-tissues (Alspaugh).

1.2.4.4 Truncated view artefact

A truncated view artefact is produced whenever any part of the patient or imaged object is present in some but not all of the views obtained for a slice. Although this artefact may not create a severe visual disturbance in the image, it can alter the CT numbers in a manner that will compromise the accuracy of quantitative analyses. The truncated view artefact can be noticed as a white edge at the border of the image in Figure 1.8 (a) or a darker area at the top and the bottom of the image in Figure 1.8 (b). (Lehr 1983)

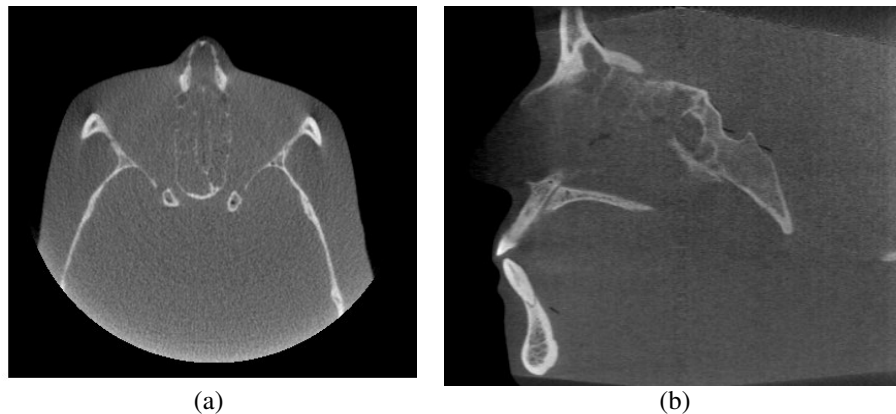


Figure 1.8 An axial (a) and sagittal (b) view of a phantom scanned with the i-CAT CBCT scanner. The white border in (a) and darker border in (b) show the truncated view artefact.

1.2.4.5 Limited dynamic range of the detector

The CBCT scanners in dentomaxillofacial imaging focus on the imaging of hard density structures (Figure 1.9). These are structures with high HU (Figure 1.3 and 1.4). Because the range of the detector is only limited, it is not possible to capture all intensities which correspond to air and high-density structures. Therefore in CBCT scanners for dentomaxillofacial applications, the focus is on the visualisation of high-density structures, and there is a loss of the visualisation of soft-tissues.

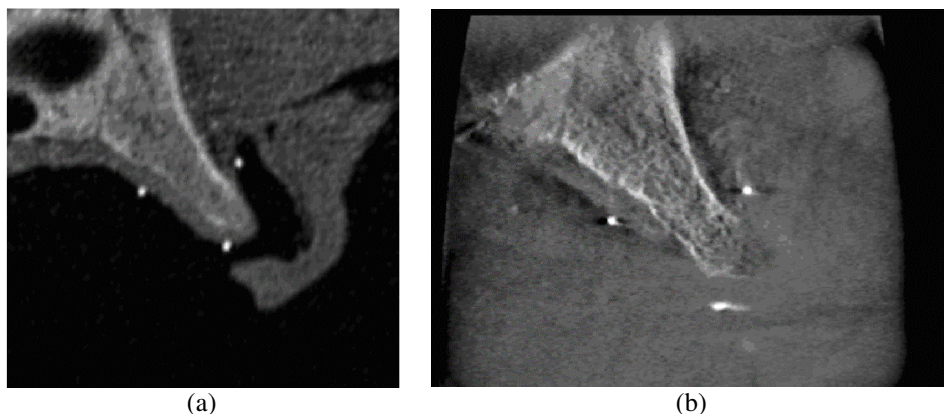


Figure 1.9 A cadaver specimen is scanned both with a computed tomography scanner, Sensation 16 (a) and a CBCT scanner, Accuitomo 3D (b). For the CT scanner, it is possible to see the transition between soft-tissue and air. For the Accuitomo 3D it is not possible to see this transition because of the limited dynamic range of the detector.

1.3 CBCT scanners in dentomaxillofacial radiology

Different manufacturers have launched their CBCT scanner for the dentomaxillofacial field (Mozzo *et al* 1999, Arai *et al* 2001, Sukovic *et al* 2003 and Araki *et al* 2004). Because these scanners come from different manufacturers, they may have different technical specifications. Therefore it is useful to analyse the specifications of these scanners (Table 1.1) before properties like image quality or radiation dose are studied. A proper knowledge of the specifications may help in understanding results acquired in later studies. The four scanners, which are described in Table 1.1, are the scanners that were studied in this thesis. These were the models that were available in the winter of 2006 at our institute or collaborating universities. After 2006 there was a massive growth of the different available CBCT scanners. But these scanners will not be discussed in this thesis.

Table 1.1 Properties of the evaluated CBCT scanners

	i-CAT	NewTom 3G	MercuRay	Accuitomo 3D
<i>Current (mA)</i>	5.5	15 ³	10 or 15	1-10
<i>Potential (kVp)</i>	120	110	60-120 (step 20 kV)	60-80 kV (step 1 kV)
<i>Scanning time (s)</i>	10, 20, 40	36	10	9, 18
<i>Exposure time (s)</i>	1.92, 3.67, 7.188	5.4	10	8.31, 16.02
<i>Exposure time of one frame (ms)</i>	12	15	33	30
<i>Current x exposure time for one frame (mAs)</i>	0.066	0.208 ³	0.347-0.521	0.030-0.300
<i>Basis images</i>	160, 306, 599	360	288	512
<i>Current x exposure time (mAs)</i>	10.56, 20.2, 39.53	75 mAs ³	100 or 150	8.31-83.1 or 16.02-160.2
<i>Focal spot (mm)</i>	0.5	0.5, 1.5	0.6	0.5
<i>Type of exposure</i>	Pulsed	Pulsed	continuous	continuous
<i>Parameters selected by the operator</i>	Scanning time and scan height	Size of the FOV	kV, mA for 1 frame, size of the FOV	Scanning time, kV, mA for 1 frame
<i>Patient positioning</i>	Sitting	Supine	sitting	Sitting
<i>Source to rotational Centre distance (cm)</i>	48.069	66.3	82.0	33.5
<i>Rotational center to detector distance (cm)</i>	20.51	28.5	29	34.9
<i>Source to sensor Distance (cm)</i>	68.58	94.8	111.00	68.4
<i>Detector type</i>	Flat panel	CCD 12-bit	CCD 12-bit	CCD 8-bit
<i>Detector size (cm)</i>	20 x 25	Ø 15.24, 22.86 or 30.4	Ø 12 to 29	Ø 10.16
<i>Detector size (pixel)</i>	960 x 768	1000 x 1000	1024 x 1024	240 x 320
<i>FOV dimensions (cm)</i>	16 x 21, 16 x 13, 16 x 8, 16 x 6	10 x 10, 13 x 13, 18 x 18	51.2 x 51.2, 102.4 x 102.4, 150 x 150, 193.5 x 193.5	4 x 3
<i>Voxelsize in plane (mm)</i>	0.2-0.4	0.16-0.42	0.1-0.4	0.125
<i>Min reconstruction increment (mm)</i>	0.2 ²	0.4 ¹	0.1 ²	0.125 ¹
<i>Suggested prize⁴</i>	£ 97.000	£ 146.000	£ 159.400	£ 103.600

¹This is the minimal slice increment that can be selected. ²For these scanners, only cubical voxels are possible and the smallest dimension of cubical voxel is given.

³The NewTom 3G works with automatic exposure control (AEC), therefore in this table the value with maximum exposure is given.

⁴These are the price indications of 2005 given by Kau *et al* 2005. Please note that this is a snapshot.

1.3.1.1 X-ray exposure

The properties of the X-ray exposure of a CBCT scanner are mainly determined by the energy of the X-ray beam, which is determined by the tube voltage and the tube current. The tube voltage is expressed by the kVp. It is important to note that there are scanners which work at a rather low kVp range like the Accuitomo 3D (60-80 kVp) and scanners which work at a higher kVp range like the i-CAT (120 kVp).

The tube current is expressed in miliampere (mA). For CBCT scanners, different basis images or frames are captured. This means that different radiographs are acquired. To acquire such a radiograph the X-ray tube must be turned on during a certain amount of time. This is called the exposure time for one frame. To capture the next basis image, the gantry must rotate over a certain angle, determined by the number of basis images. During this rotation the X-ray beam still releases X-rays in case of continuous exposure or does not release X-rays in case of pulsed exposure. This means that for CBCT scanners with pulsed exposure, there is a difference between the scanning and the exposure time. Mainly due to the combination of continuous exposures and high mA per frame, large miliampere x seconds (mAs) values are achieved for the MercuRay (100 mAs or 150 mAs) and the Accuitomo 3D (8.31 mAs to 160 mAs). It is also important to note that there is a large variability between the different scanners.

When the operator uses the scanner, there are three levels of freedom offered. 1) He has complete freedom; he can choose all kind of kVp and mAs settings. 2) The operator has less freedom; he can choose between different protocols with different mAs or kVp values. These settings are programmed in by the manufacturer defined dedicated protocols. 3) He has no freedom at all when automatic exposure control is programmed on the scanner; it means that the user of the scanner does not have any freedom for the selection of the tube settings. The tube settings are then defined by the scanner based on two scout views of the patient: one in lateral and one in coronal position. This is the case for the NewTom 3G.

1.3.2 X-ray detector

The X-ray detector captures the X-rays. This detector is an image intensifier with a charged coupled device (CCD) or a flat panel detector (FPD) (Guerrero *et al* 2006). The first type of detector works as follows: a phosphor screen converts the X-rays into visible

light. The emitted light hits a photo cathode and the energy of the photons releases electrons from this cathode. A large potential difference between the cathode and the output accelerates the ejected electrons. The resulting electron beam is directed into a small phosphor screen by electrostatic or magnetic focusing and converted to light photons again. This focusing makes the system suitable to be coupled to a camera without any loss of light. The main advantage of an image intensifier system is that it is capable of producing dynamic image sequences in real time at video rate (Suetens 2002).

The second type of detector is the flat panel detector in which the sensor elements are produced in a thin film of amorphous silicon (a-Si). The flat panel detector consists of a scintillator screen and a photo sensor array composed of arrayed photodiodes and switching devices. The scintillator converts an X-ray beam into an optical signal that is converted to an electrical signal by a photodiode, which is in turn read out by the switching device array. The flat panel detector does not generate veiling glare or distortion in the image and has a smaller detector pitch than an image intensifier detector. Besides the type of the detector, also the size of the detector and the number of pixels for the detector are important factors (Suetens 2002).

The first CBCT scanners for dentomaxillofacial applications were made with Image Intensifiers (Accuitomo 3D and NewTom 9000). The i-CAT was the first scanner, which introduced the flat panel detector. Nowadays, the general trend is to use a flat panel detector for CBCT scanners.

1.3.3 Size of the X-ray beam

The size of the X-ray beam in combination with the diameter of the X-ray detector determines the size of the FOV that is acquired by the CBCT device. The size of the X-ray beam is determined by the size of the detector, by the selected protocol and by the distance between X-ray source and detector. This distance can be divided into the distance between X-ray source and rotational centre of the scanner and the distance between the rotational centre and the X-ray detector. To ensure that the skin dose on the patient is reduced, the distance between the rotational centre and the X-ray source should be large. To reduce patient scatter and have a high signal to noise ratio, the distance between the rotational centre and the detector should be small. A last asset is to have the distance between the X-ray source and the detector as small as possible such that a compact scan-

ner can be built that can be easily placed in a common dental practice. This is mainly achieved by the Accuitomo 3D and the i-CAT.

1.3.4 Reconstruction parameters

The studied reconstruction parameters are: reconstruction filter, FOV and resulting voxel size. Because not a lot of information is available about the reconstruction algorithms of the different scanners, this is omitted here. Most scanners offer the ability to use different FOV such that various clinical indications can be imaged without the unnecessary exposure of healthy tissue. These are clinical indications for oral implants, Temporo Mandibular Joint (TMJ) imaging, orthodontic applications and maxillofacial indications.

1.3.5 Patient positioning

For CBCT scanners, there are two possibilities for the patient positioning. The patient may lie down or be seated during image acquisition. Most scanners have a model in which the patient can sit during image acquisition. This is more comfortable for the patient and also helps in making the scanner more compact, so it can be placed in the dental practice.

1.4 Radiation dose

1.4.1 The need for radiation dose assessment

When an X-ray passes through the body of a patient it releases energy and may cause possible biological damage. This can lead to auto repair of the damage, to cell destruction or to initiation of uncontrolled cellular division (Suetens *et al* 2002). To evaluate the harm of ionisation exposure, the International Commission of Radiation Protection (ICRP) has set up some guidelines that consist of quantities to measure the radiation dose and to express the harm of radiation dose (ICRP 2007).

The released energy of the X-ray to the body is expressed as the *absorbed dose* in Gray (Gy). One Gy is an absorbed dose of one joule of energy per kilogram of irradiated material. The absorbed dose is independent of the type of radiation. Alpha particles for example can cause more damage than X-rays. To take into account the nature of the radiation, the absorbed dose needs to be converted to the radiation weighted dose or equivalent dose by multiplying the absorbed dose with a radiation weighting factor (ICRP

2007). For X-rays this factor is 1. The radiation weighted dose is expressed in Sievert (Sv) (Suetens 2002).

For protection means, the radiation weighted dose to the tissues needs to be evaluated. Not all the organs are equally sensitive to radiation; therefore to calculate the complete harm of an X-ray to the body or the effective radiation dose, tissue weighting factors need to be applied which take into account the sensitivity of the different organs to radiation dose. The weighted sum of the radiation dose with their respective tissue weighting factors is called the effective radiation dose (ICRP 2007).

The tissue weighting factors are determined by the ICRP and are updated on a regular basis based on epidemiological studies such as the Life Span Study (LSS) cohort of the atomic bomb survivors (Brenner *et al* 2003).

There is international agreement that intermediate and high doses of ionising radiation (this means doses of more than 100 mSv) produce deleterious consequences in humans including but not exclusively cancer (Brenner *et al* 2003). At lower doses, however, the situation is not that clear but no evidence exists of a threshold value below which no damage occurs. Therefore the non-threshold linear model (NLT) is used (Brenner *et al* 2003). The radiation dose levels of CBCT scanners vary between 40 μ Sv and 400 μ Sv (Ludlow *et al* 2003 and Ludlow *et al* 2006).

A study performed by Aroua *et al* (2004) in Switzerland in 1998 showed that 43% of the total number of X-ray examinations which were performed in Switzerland in all the modalities of diagnostic and interventional radiology were coming from dentistry. Despite the high use of dental X-rays, they were only responsible for 1% of the radiation dose, which the Swiss population received. This study was performed, however, before the introduction of CBCT in dentistry. Therefore, the largest contributions to the radiation dose of dental exposures were derived from panoramic exposures, periapical exposures and long bitewing. The last two are both intra-oral exposure types. When some of these radiographic modalities will be replaced by CBCT, the exposure derived from dental applications may increase. It is also important to note that children are a sensitive group receiving a lot of dental radiographs. Therefore, there is a need for a better assessment of the radiation dose levels for CBCT.

1.4.2 Quantification of radiation dose

The effective dose cannot be measured directly. In this dissertation a Rando Alderson Phantom (Alderson Research Laboratories, Long Island City, NY, USA) was used. Such a phantom consists of a human skeleton embedded in soft-tissue simulating material taking into account the differential density of average organs. The phantom is divided into several slices. Radiation dose can be measured by putting thermoluminescent dose-meters (TLD) at the positions of the organs, which are sensitive to radiation dose. After an exposure of the phantom and a read out of the TLDs, the effective radiation dose can be calculated.

Because measurement of the effective radiation dose through the use of a Rando Alderson phantom is a very time consuming procedure, technical methods have been developed to estimate the effective radiation dose. Based on tabulated conversion factors, the effective radiation dose can be estimated from technical parameters (McNitt-Gray 2002).

The technical parameter, which is mostly used in computed tomography, is the Computed Tomography Dose Index (CTDI) displayed on the console of MSCT scanners. The CTDI is measured in dedicated cylindrical phantoms with the use of an electrometer and an ionisation chamber with a length of 10 cm. Because the CTDI is shown on the console of MSCT scanners, the change in dose can be evaluated by varying the different parameters like tube current, tube voltage, collimation and table feed, which all influence the radiation dose to the patient. The CTDI however cannot be used as a measure for the radiation dose in CBCT scanners.

1.5 State-of-the-art of validation of bone related image measurements

In general, four different imaging-based methodologies can be applied for the evaluation of the accuracy of image based measurements (Van Cleynenbreugel *et al* 1997): the use of software phantoms (De Man *et al* 1999), hardware phantoms (Van Cleynenbreugel *et al* 1997, Prevrhal *et al* 1999, Marmulla *et al* 2001, Kang *et al* 2003, Loubele *et al* 2006), cadaver studies (Aamodth *et al* 1999, Cavalcanti *et al* 1999, Cavalcanti *et al* 2004, Kobayashi *et al* 2004, Lascalea *et al* 2004, Egger *et al* 2005) and in-vivo measurements (West *et al* 1997). Each method has its own criteria to establish the relationship between a known gold standard and its measurement by an imaging modality. In practice, however, establishing a 3-D geometric gold standard with sufficient accuracy and detail is not

straightforward for complex shaped anatomical objects and even impossible for clinical patient images acquired in vivo. While phantom studies allow a direct access to the objects under study for geometric characterization, their validity for in vivo imaging is necessarily questionable.

For evaluation of the accuracy of CBCT, different studies have been performed. Three studies will be discussed in further detail (Kobayashi *et al* 2004, Marmulla *et al* 2001, Lascala *et al* 2004). Marmulla *et al* 2001 used a geometrical object to evaluate the accuracy of the Newtom 9000 DVT. The purpose of that study was to evaluate the geometrical distortion of the NewTom 9000. The geometric deviations, which were found in this study, were below the resolution power of the NewTom 9000. The conclusion of this study was that the digital volume tomography of the NewTom 9000 presented images that were geometrically correct and, from a geometrical point of view, suitable for 3-D implant planning.

Kobayashi *et al* (2004) used five cadavers with edentulous mandibles to evaluate the accuracy of the Dental 3D CT (PRS 9000 [prototype]; Asahi Roentgen, Kyoto, Japan) and the RADIX-Prima (Hitachi Medical, Tokyo, Japan). The accuracy was measured at seven different anatomical sites on a cadaver mandible by selecting slices by manually searching for the holes drilled into the mandible at various sites: Distances were measured by indicating a point in the hole and a point on the alveolar ridge. The ground truth was acquired by making slices through the hole in the mandible and measuring the distances with a calliper. This study showed that the CBCT device was a useful tool for preoperative evaluation in dental surgery because the relatively small field size of its images limits the patient's exposure to radiation.

Lascala *et al* (2004) used a similar approach to evaluate the accuracy of the NewTom 9000 (Quantitative Radiology, Verona, Italy). Metal markers were put on different landmarks on dry skull. The skulls were immersed in water and direct calliper measurements between markers were compared to radiographic measures using dedicated software (Quantitative Radiology, Verona). The conclusion of their study was that, although the CBCT image underestimates the real distances between skull sites, differences are only significant for the skull base and therefore it is reliable for linear evaluation measurements of other structures more closely associated with dentomaxillofacial imaging.

The study of Kobayashi *et al* (2004) and Lascala *et al* (2004) are representative studies that evaluate the accuracy of scanners used in dentomaxillofacial imaging. Common for these studies are the bone thickness measurements both on the dry skull and the radiographic data performed by observers and the use of markers to indicate the sites that need to be measured.

1.6 Main contribution of this thesis

In literature, a comparative report on image quality and radiation dose of different CBCT devices is lacking. Because most studies are performed on the evaluation of image quality based on cadaver skulls, it is not possible to compare the results of different studies. The study of Kobayashi *et al* (2004) and Lascala *et al* (2004) also need much user interaction, making these studies time consuming and suffering from inter-and intra-observer agreement.

Based on the observations there is a need for a standardized protocol making it possible to evaluate image quality and radiation dose of different CBCT scanners. In this dissertation, methods will be searched for that can help for the development of such a standardized protocol. The focus will mainly lie on the improvement of the assessment of image quality and to balance these results with the radiation dose. To reach this overall aim, a more automated method was used for the evaluation of image quality. The most important issues are discussed in the following paragraphs.

1.6.1 Software design

In this thesis, software is further developed which was designed in our research group (Van Cleynenbreugel *et al* 1997), for the evaluation of the accuracy of image based measurements. This software generates a geometrical model based on the technical drawings of a phantom. This model is registered with a 3-D CT-image of the phantom based on maximisation of mutual information (MMI) (Maes *et al* 1997). Based on this registration, similar positions in the geometrical model and the CT-image can be found and so at corresponding places the thickness of different structures can be measured and compared with the sizes derived from the geometrical description.

This software was first applied to the European Spine Phantom (ESP). But for the evaluation of bone segmentation accuracy for dentomaxillofacial scanners, more realistic models of relevant anatomical structures need to be implemented in the software.

These extensions were performed in Chapter 3 for models derived from CT scanners, in Chapter 4 for a model derived from a laser scanner and in Chapter 5 for models derived from medical physics phantoms.

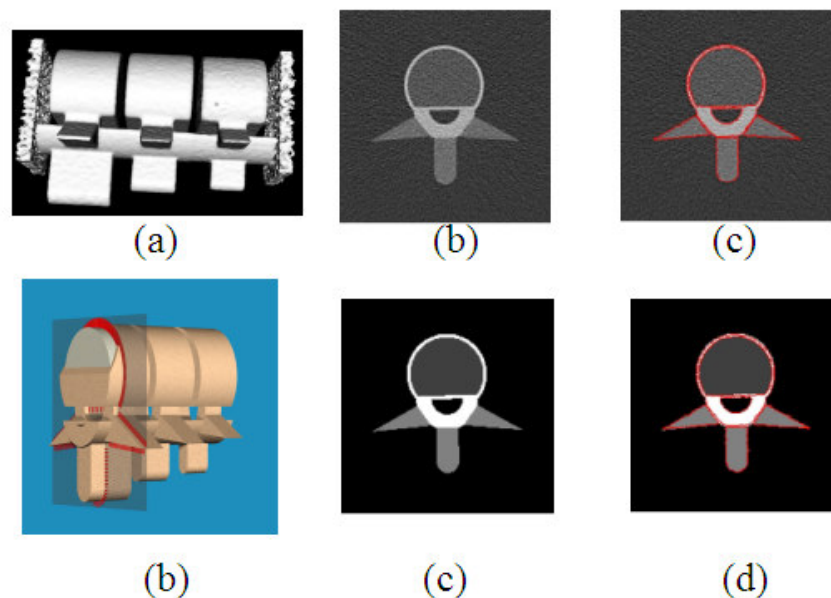


Figure 1.10 The ESP-phantom, presented as a 3-D model generated from a CT-image (a) and as model generated from the 3-D geometric description (d). Thanks to the registration, slices at corresponding places can be selected in the CT-image (b) and the geometric model (e). Thanks to this registration at the corresponding places the interesting structures can be segmented (c) and compared (f). (Courtesy Frederik Maes and Johan Van Cleynenbreugel)

1.6.2 Search for an optimal phantom

As mentioned in 1.6.1 there is a need for more realistic phantoms for the evaluation of CBCT scanners for dentomaxillofacial applications. An appropriate phantom was not available at the start of this dissertation; therefore also a search was performed for more appropriate phantoms towards this thesis. Standard skull phantoms (chapter 2), a dedicated skull phantom (chapter 4) and phantoms for quality assurance testing (chapter 5) testing were evaluated during this dissertation.

1.6.3 Protocol for comparative evaluation of different scanners

The final goal of this dissertation was to compare different CBCT scanners for dentomaxillofacial applications and also to compare them with a similar protocol on an MSCT scanner. The final result of this study is presented in chapter 4.

1.6.3.1 Outline of the thesis

- Presentation of software for automated image quality assessment (Chapter 3)
- Proposal for optimisation of image quality versus radiation dose on MSCT scanners (Chapter 3)
- Extension of software for automated image quality assessment to different phantoms (Chapter 3, 4 and 5)
- Evaluation of image quality versus radiation dose of four different CBCT scanners and one MSCT scanner (Chapter 5)

Chapter 2

Radiation dose versus image quality for low-dose CT protocols of the head for maxillofacial surgery and oral implant planning.

2.1 Abstract

Objectives: The goal of this study was to design a spiral CT protocol for 3-D visualisation of the skull with an effective dose as low as achievable for indications of 3-D image based dental implant planning, maxillofacial surgery planning and postoperative evaluation. For this purpose, the tube voltage and current of the X-ray tube were decreased.

Material and Methods The effective radiation dose of the low-dose CT protocol with 80 kV and 28 mAs was compared with the radiation dose of a routinely used CT protocol for the head with 120 kV and 90 mAs on a multi-slice spiral CT scanner. The semi-anthropomorphic European Spine Phantom (ESP) was scanned with a voxel size of 0.49 mm x 0.49 mm x 0.4 mm. The total effective dose was determined by measuring effective organ doses using an anthropomorphic Rando Alderson phantom, loaded with 91 TLD 100 lithium fluoride dosimeters at 9 different organs. In order to obtain an upper estimate for the above-mentioned examinations, we scanned the complete head of this phantom. The bone was segmented based on an optimal threshold value. Before segmentation, the noise in the low-dose images was reduced with an anisotropic diffusion filter. The absolute accuracy of this segmentation algorithm was measured by comparison with the geometric ground truth provided by the ESP.

Results: The effective dose for the routinely used CT-protocol for the whole head was 1.5 mSv and for the low-dose protocol was 0.16 mSv, which is in the order of the dose of a radiographic image of the skull. The mean difference between the ground truth and the thickness measured on the clinical protocol was smaller than 0.1 mm and the standard deviation was smaller than 0.24 mm. For the low-dose protocol, the mean difference was smaller than 0.3 mm with a standard deviation below 0.4 mm.

Conclusions: The tests on the ESP indicate that the accuracy of the measurements on the low-dose CT is still acceptable. Further tests on a more realistic head phantom and cadaver studies are needed.

2.2 Introduction

For the planning of maxillofacial and oral implant surgery (Schutyser *et al* 2000, van Steenberghe *et al* 2002), multi-slice CT is commonly used. Since conventional CT protocols are generally associated with high radiation dose levels, a number of studies have attempted to work with low-dose CT protocols for planning purposes (Hein *et al* 2002, Hagtvedt *et al* 2003, Imhof *et al* 2003a, Imhof *et al* 2003b). Lowering the radiation dose can be done by decreasing mAs or kV, increasing the pitch, using thicker slices or using a larger focus (Imhof *et al* 2003a, Imhof *et al* 2003b).

The aim of this study was to determine the parameters for a low-dose multi-slice CT protocol of the head that allows segmentation of the facial bones with sufficient accuracy for oral implant and maxillofacial surgery planning. For this purpose, a CT-protocol with lower kV and mAs and higher pitch was used. Then the effective radiation dose and the image quality were evaluated.

2.3 Material and methods

2.3.1 Radiation dose assessment

The effective radiation dose was measured using an anthropomorphic Rando Alderson Phantom. The phantom represents an average man and consists of a human skeleton embedded in tissue-equivalent material. It consists of 36 slices, each with a thickness of 2.5 cm. Each slice has a 3cm spaced grid of holes for insertion of thermoluminescence dosimeters (TLD). For the dose measurements, TLDs of type TLD-100 (Lithium Fluoride (LF) : Mg, Ti) and TLD-100H (LiF: Mg, Cu, P) were used. In this study, 87 TLDs were put in the upper nineteen slices. During pilot experiments with multi-slice CT scans of the head, the contribution to the effective dose of the organ doses situated between slice 20 and 36 were found negligible (only 1.45%). The location of sensitive organs and tissues was determined by visually comparing the slices of the phantom to an atlas of cross-sectional anatomy (Cahill and Orland, 1984). The number of TLDs used for measuring the mean absorbed dose per anatomic region or organ is shown in Table 2.1.

After radiographic exposure, the TLDs were analysed with a fully automated Harshaw 6600 reader[®] (Bicron NE, Solon, OH). Calibration was performed with an ALCYON cobalt-60 radio therapeutic unit (General Electric CGR MeV, Buc, France). The effective organ doses were calculated based on the measured organ doses and the tissue

weighting factors according to International Commission of Radiation Protection (ICRP) 60 (1992) (The calculation according to the new ICRP 2007 guidelines can be found in Chapter 5). The brain and salivary glands were regarded as the only remainder organs that contribute substantially to the effective radiation dose. For the salivary glands, the tissue weighting factors described by Golikov and Nikitin (1989) were used. The mean radiation dose D of an organ was calculated following Huda and Sandison (1984)

$$D = \sum_i f_i \cdot D_i,$$

where f_i is the fraction of the total organ mass in slice i of the Rando Alderson phantom, D_i is the average radiation dose to the fraction of the organ situated in slice i , *i.e.*, to the part of this organ lying within Rando section i . For the fractions f_i the values defined in Golikov and Nikitin (1989) and Huda and Sandison (1984) were used. For the thyroid gland, the mean organ dose was measured as the average of the 9 TLDs. The mean dose of the salivary glands was calculated as the mean of the parotid, submandibular glands and sublingual glands.

Table 2.1 Organs in anatomic regions situated in the upper nineteen slices of the Rando Alderson phantom in which TLDs are placed for measuring the mean organ doses.

Organ/anatomic region	Number of TLDs
Skeletal/red bone marrow	22
Oesophagus	9
Lungs	18
Thyroid gland	9
Brain	13
Salivary gland	8
Skin	10

For the dose measurements, the whole head was scanned. In this way, the effective dose for CT-protocols for all possible maxillofacial surgeries was overestimated. First, a topogram was made with 50 mAs and 120 kV. In order to reach sufficiently high radiation dose levels for the TLDs and to lower the influence of the topogram on the dose values, each scan protocol was repeated 10 times without changing the position of the phantom in the CT scanner.

2.3.2 CT protocols

CT scanning of the Rando Alderson phantom for 3-D visualization of the head region was performed using a multi-slice CT scanner (Siemens Sensation 16, Erlangen, Germany). Scanning was performed using different acquisition protocols in order to allow comparison between a routinely used clinical protocol and a low-dose protocol (see Table 2.2) for the associated scanning parameter settings). The low-dose CT protocol used in this study was derived from a protocol on the Siemens Sensation 16 aimed for maxillofacial surgery planning.

The low-dose CT protocol was defined as the one that gave the lowest $CTDI_{vol}$ for this scanner by lowering the mAs and the kV and increasing the pitch. The $CTDI_{vol}$ displayed on the scanner console was used for this optimisation procedure. The low mAs and kV settings were only possible if the pitch was increased. Although the use of thicker slice thickness makes it possible to reduce further the radiation dose (Imhof *et al* 2003a and Imhof *et al* 2003b), this parameter was not changed in the current protocol because of the accuracy demands for surgical planning purposes.

Table 2.2 Parameters of the protocol used for indications of maxillofacial surgery (clinical) and the low-dose protocol (low-dose) on the Siemens Sensation 16.

	Clinical	Low-dose
Slice thickness (mm)	0.75	0.75
Slice collimation (mm)	0.75	0.75
Slice increment (mm)	0.4	0.4
Table feed (mm/rot)	6	12
Pitch p ()	0.5	1
Current (mAs)	90	28
Potential (kV)	120	80
Rotation time (s)	0.75	0.75
Scan length (mm)	225	227
Scan time (s)	29.48	14.19
Reconstruction filter	H60s	H60s
$CTDI_{vol}$ (mGy)	20.16	2.5

2.3.3 Image Quality

Because the CT images are used for maxillofacial surgery and oral implant planning purposes, image quality can be assessed by quantifying the segmentation accuracy of bone structures. The segmentation quality is evaluated based on two phantoms, the European Spine Phantom (ESP) (Kalender *et al* 1995) and a skull phantom. The ESP phantom is a geometrically defined semi-anthropomorphic phantom (Figure 2.1). It contains a

spine insert consisting of three vertebrae of increasing bone mineral density and thickness of cortical structures. It is made of water- and bone-equivalent solid materials. Furthermore, the geometry is guaranteed to be known up to 0.1 mm (Kalender *et al* 1995).

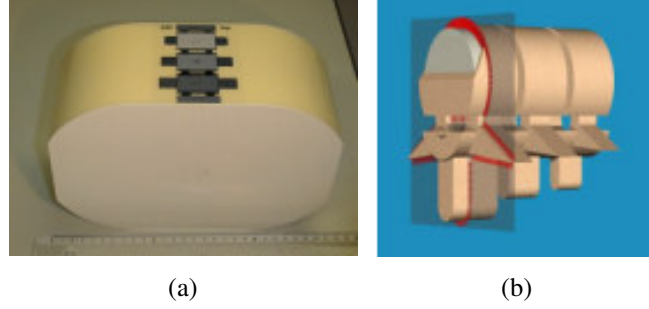


Figure 2.1 The ESP phantom (a) and a virtual model of the ESP phantom (b).

For evaluating the segmentation accuracy based on the ESP, the CT-images were first registered to a CAD-model of the ESP by maximization of mutual information of corresponding voxel intensities (Maes *et al* 1997). This method leads to a rigid transformation that maps every location in the geometrical phantom description space into the image volume space. As a result, measure lines defined at particular positions of interest in the phantom description can be mapped through the transformation in the image volume space to generate one-dimensional (1-D) density profiles. Measure lines perpendicular to model edges are considered.

The resulting 1-D profiles are block and step edges respectively. 1-D segmentation based on an optimal threshold (Prevhal *et al* 1999) can be applied to calculate the location of the edge points on these profiles. The optimal threshold is defined as the 50% value of the plateau values at either side of the edge. The plateau values are estimated as average values for all measure lines defined on the same structure. A number of measure lines (N_l) were defined on a number of axial planes (N_p) for the three cortical walls ($N_l = 255$, $N_p = 21, 23, 23$) and the three processi spinosi ($N_l \times N_p = 60 \times 25, 40 \times 17, 32 \times 14$).

For each measure line the distance between the measured edge position and the edge position on the model is calculated. For the first cortical wall and the three processi (Figure 2.2 till Figure 2.4), the thickness is measured on each measure line as an extra quality measure. For each structure, mean, standard deviation and 95% percentile for the absolute differences are calculated from the $N_l \times N_p$ measurements.

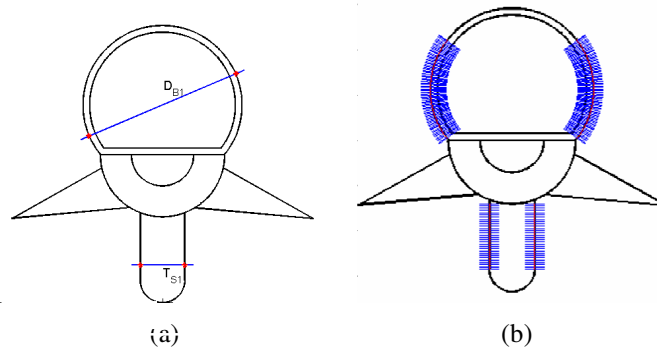


Figure 2.2 Figure (a) illustrates a line used for the measurement of the thickness of the diameter of the arch (D_{BI}) and for the measurement of the thickness of one of the spinosi processi. Figure (b) illustrates the distribution of the measure lines for the thickness of the arch.

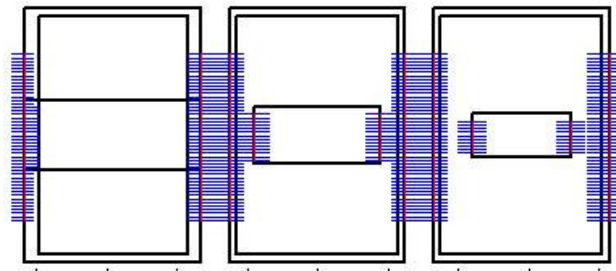


Figure 2.3 Illustration of the distribution of the measure lines in coronal view of the geometrical model of the ESP phantom.

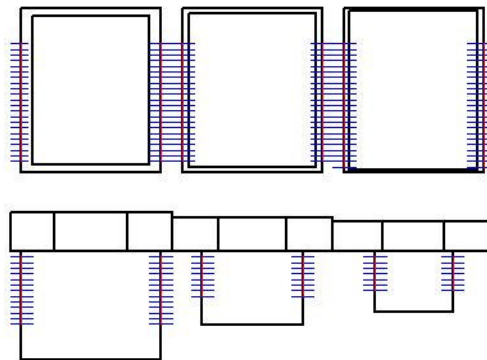


Figure 2.4 Illustration of the distribution of the measure lines in sagittal view of the geometrical model of the ESP phantom.

The skull phantom is a complete dry adult skull embedded in plastic. In the absence of an accurate geometric description of the skull phantom, image quality is assessed by quantifying differences between segmentations of the skull obtained with the low-dose imaging protocol (Figure 2.5 (b)) and a reference clinical protocol (Figure 2.5 (a)). The skull is segmented based on a threshold using marching cubes (Lorensen and Cline; 1987) resulting in a triangular mesh. The optimal threshold value cannot be calculated based on the measure lines because no geometrical description of the skull phantom is available. Therefore the threshold is calculated based on the intensity histogram of the image. We assume that the intensity histogram of the image can be modelled as a mixture of two Gaussian distributions: soft-tissue and bone (Baillard and Barillot, 2000). The parameters of these two distributions can be calculated with a Stochastic Expectation-Maximization (SEM) algorithm (Dempster *et al* 1976).

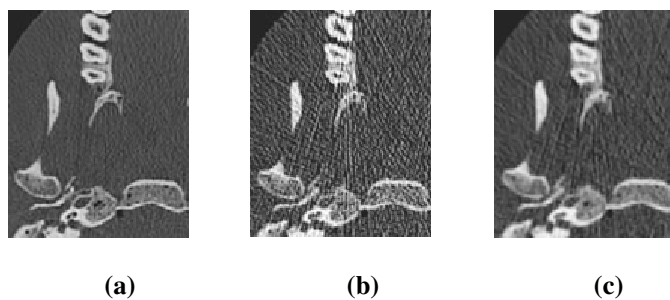


Figure 2.5 Axial slices of the skull phantom acquired with (a) a clinical protocol and (b) a low-dose protocol are shown. Figure (c) illustrates the use of anisotropic diffusion filtering, which makes it possible to reduce the image noise, while the edges are preserved.

The image intensity for which the two Gaussian functions give the same probability is used as the bone threshold for the marching cubes algorithm. Before segmentation of the skull in the low-dose CT images, noise in these images is also reduced with an edge-preserving non-linear anisotropic diffusion filter (Ibáñez *et al* 2003), (Figure 2.5 (c)). Differences in segmentation are evaluated by calculating the distance between each point on the reference segmentation surface (derived from the clinical protocol) and the closest point on the other surface (derived from the low-dose protocol) (De Groeve *et al* 2001). No additional surface registration is required, since both surfaces are obtained from images of the skull phantom scanned in the same position. Again mean, standard deviation and 95% percentiles of the absolute differences are calculated.

2.4 Results

2.4.1 Radiation dose assessment

Table 2.3 shows the calculation of the effective dose for the clinical protocol and the low-dose protocol. The effective dose for the low-dose protocol was 12.7% of the effective dose of the clinical protocol. For both protocols, the largest contribution to the effective dose comes from the red bone marrow, the thyroid, the brain and the salivary glands because these were positioned in the primary beam. The thyroid was positioned in the primary beam because the chin was included into the primary beam due to the construction of the phantom.

Table 2.3 Calculation of effective doses for a CT-scan of the whole head acquired with the clinical protocol for maxillofacial indications and the low-dose protocol

	W_T	Absorbed dos (mGy)		Absorbed dose x W_T	
		Clinical	Low-dose	Clinical	Low-dose
Gonads	0.2	0	0	0	0
Red bone marrow	0.12	2.96	0.30	0.36	0.04
Colon	0.12	0	0	0	0
Lung	0.12	0.44	0.05	0.05	0.01
Stomach	0.12	0	0	0	0
Bladder	0.05	0	0	0	0
Breast	0.05	0	0	0	0
Liver	0.05	0	0	0	0
Oesophagus	0.05	0.44	0.05	0.02	0
Thyroid	0.05	6.74	1.23	0.34	0.06
Skin	0.01	1.22	0.06	0.01	0
Bone surface	0.01	2.83	0.29	0.03	0
Remainder					
Brain	0.025	13.11	1.39	0.33	0.03
Salivary glands	0.025	14.31	1.69	0.36	0.04
Total (mSv)				1.50	0.18

W_T : tissue weighting factor (Gijbels *et al* 2003).

2.4.2 Image Quality

The image quality results based on the ESP phantom are shown in Table 2.4 and Table 2.5. Table 2.4 shows the mean, standard deviation and 95% upper limit of the absolute distances between measured and exact edge position for the clinical protocol, the low-dose protocol and the low-dose protocol with reduced noise by anisotropic diffusion filtering. Table 2.5 shows the mean, standard deviation, minimum and maximum, and the 95% confidence interval of the measured thickness of the first cortical wall and the three processi of the ESP. The largest error was obtained for the third cortical wall of the ESP, which is the smallest structure with a thickness of 0.5 mm, which is below the accuracy limit for detection for segmentation purposes. For the other cortical walls and the three processi, the maximum of the 95% upper limit increases from 0.41 mm to 0.95 mm when the low-dose protocol is used. This value is found for the first processus that has a thickness of 10 mm.

An edge-preserving anisotropic diffusion filter (Ibáñez *et al* 2003) applied to the images could reduce the noise. With this filter it is possible to reduce the 95% percentile of the distances between edges of the CAD-model and the edges of the CT-image of the third cortical segmentation wall from 1.23 mm to 0.92 mm, and the maximum 95% percentile of the two other cortical walls and the three processi reduced from 0.95 mm to 0.7 mm. This made it possible to segment the bone equivalent material in the ESP phantom with submillimeter accuracy for the low-dose protocol with the parameters given in Table 2.2. Because the tests with the ESP phantom indicate that bone can be segmented with an accuracy of 0.5 mm in the CT-images acquired with the clinical protocol, the facial bone segmentation in the clinical protocol could be used as a ground-truth for evaluating segmentation accuracy of the skull in low-dose images. Table 2.6 shows that the 95% upper limit for the distances between the segmentation of the skull in the clinical protocol and the low-dose to which post-filtering is applied, is below 1 mm. This makes it still possible to segment bone in these images with submillimeter accuracy.

Table 2.4 Results of the measurements of the absolute distances between the edges of the CAD model and the segmented edges of CT-images of the ESP phantom along the different measure lines for the different protocols. For each structure, the mean absolute distance, the standard deviation of the absolute distance and the 95% percentile of the absolute distance are shown.

		Clinical	Low-dose	Low-dose + filtering
Cortical wall 1	Mean (mm)	0.10	0.29	0.28
	Std (mm)	0.08	0.24	0.20
	95% (mm)	0.38	0.70	0.58
Cortical wall 2	Mean (mm)	0.09	0.27	0.29
	Std (mm)	0.07	0.23	0.21
	95% (mm)	0.21	0.62	0.58
Cortical wall 3	Mean (mm)	0.26	0.44	0.44
	Std (mm)	0.12	0.38	0.30
	95% (mm)	0.44	1.23	0.92
Processes 1	Mean (mm)	0.16	0.42	0.33
	Std (mm)	0.13	0.30	0.22
	95% (mm)	0.41	0.95	0.70
Processes 2	Mean (mm)	0.10	0.37	0.25
	Std (mm)	0.08	0.28	0.18
	95% (mm)	0.26	0.90	0.58
Processes 3	Mean (mm)	0.15	0.30	0.26
	Std (mm)	0.24	0.27	0.30
	95% (mm)	0.35	0.82	0.70

Table 2.5 Results of the thickness measurements of the first cortical wall and the three processi spinosi of the ESP phantom along the different measure lines for the different protocols. For each structure, the model thickness, the mean thickness, the standard deviation of the thickness and the 95% percentile of the thickness are shown.

		Model thickness	Clinical	Low- dose	Low-dose + filtering
<i>Cortical wall 1</i>	<i>Mean (mm)</i>	1.50	1.41	1.52	1.65
	<i>Std (mm)</i>		0.13	0.34	0.20
	<i>95% (mm)</i>		0.34	0.68	0.5
<i>Processus 1</i>	<i>Mean (mm)</i>	10.00	9.99	10.00	9.97
	<i>Std (mm)</i>		0.21	0.55	0.37
	<i>95% (mm)</i>		0.4	1.14	0.68
<i>Processus 2</i>	<i>Mean (mm)</i>	8.00	7.98	7.91	7.90
	<i>Std (mm)</i>		0.17	0.62	0.33
	<i>95% (mm)</i>		0.34	1.3	0.65
<i>Processus 3</i>	<i>Mean (mm)</i>	6.00	6.05	5.90	5.93
	<i>Std (mm)</i>		0.15	0.48	0.24
	<i>95% (mm)</i>		0.30	1.00	0.50

Table 2.6 Result of the calculation of the absolute distances between the segmentation of the facial bones in the clinical protocol and the low-dose protocol with reduced noise by the use of anisotropic diffusion filtering

Low-dose + Filtering	
Mean (mm)	0.33
Std (mm)	0.32
95 % (mm)	1.00

2.5 Discussion

Lowering kV and mAs and increasing the pitch gives a reduction of the effective dose from 1.5 mSv for a clinical head scan protocol to 0.18 mSv for the low-dose protocol. The effective dose of the low-dose protocol is similar to the effective dose for an X ray of the head (Suetens *et al* 2002). This dose reduction with acceptable image quality was possible because only the bone surface is of interest for indications of maxillofacial surgery and oral implant planning, and not the contrast of the different soft tissues, which can be needed for diagnostic purposes. The reduction of the effective dose increases the amount of noise in the images. This increased noise level can be measured as a rise in the standard deviation of the absolute distances and the thickness, and a rise of the 95% upper limit of the absolute distances and the absolute thickness error calculated on the ESP phantom (Table 2.4 and Table 2.5). The largest error is obtained for the third cortical wall of the ESP, which has a thickness of only 0.5 mm, is the smallest structure, and is below the accuracy limit for detection for segmentation purposes. For the other cortical walls and the three processi, the 95% upper limit increases from 0.41 to 0.95 mm. The noise could be reduced by applying an edge preserving anisotropic diffusion filter to the images (Ibáñez *et al* 2003). With this filter, it is possible to reduce the 95% percentile of the distances between edges of the CAD-model and the edges of the CT-image of the third cortical segmentation wall from 1.23 to 0.92 mm, and the maximum 95% percentile of the two other cortical walls and the three processi reduced from 0.95 to 0.7 mm. This makes it possible to segment the bone in the ESP phantom with submillimeter accuracy for the low-dose protocol with the parameters given in Table 2.2.

Because the tests with the ESP phantom indicate that bone can be segmented with an accuracy of 0.5 mm in the CT images acquired with the clinical protocol, the facial bone segmentation in the clinical protocol can be used as a ground-truth for evalu-

ating the segmentation accuracy of the skull in the low dose images. Table 3.6 shows that the 95% upper limit for the distances between the segmentation of the skull in the clinical protocol and the low-dose to which post-filtering is applied is <1 mm. This makes it still possible to segment bone in these images with sub-millimetre accuracy.

2.6 Conclusion

The effective dose of the low-dose protocol is only 12% of the effective dose of a standard head protocol. The tests on the ESP indicate that the accuracy of the measurements on the low-dose CT is still acceptable for the purpose of maxillofacial surgery planning and image-based oral implant planning.

Chapter 3

Assessment of bone segmentation quality of cone-beam CT versus multi-slice spiral CT: a pilot study

3.1 Abstract

Objectives: To develop a method to quantitatively assess the quality of jawbone models generated from cone beam computed tomography (CBCT) by comparison with similar models obtained from multi-slice spiral computed tomography (MSCT).

Material and methods: Three case studies were performed involving images of anthropomorphic head phantoms and real patients acquired with 3 CBCT (NewTom 9000 DVT, Accuitomo 3D and I-CAT) and 2 MSCT scanners (Somatom VolumeZoom and Lightspeed). Bone was segmented from the CBCT and MSCT images using a global threshold. CBCT versus MSCT segmentation differences were assessed by comparing bone thickness measurements at anatomically corresponding sites, identified automatically by CBCT to MSCT image registration.

Results: There was a statistically significant difference between the MSCT and CBCT segmented bone thickness, varying from 0.05 ± 0.47 mm (I-CAT) up to 1.2 ± 1.00 mm (Accuitomo 3D, posterior maxilla).

Conclusions: An automated, reproducible and observer independent method has been developed to assess the quality of CBCT bone models using MSCT as clinically established method of reference. Our validation method is generally applicable in cases where no geometric ground-truth is available.

3.2 Introduction

For successful bone surgical planning and simulation, it is important that the geometric accuracy of the bone models is established. While the accuracy of bone segmentation has already been studied extensively for MSCT (Egger *et al* 2005, Aamodt *et al* 1999, Prevrhal *et al* 1999, Van Cleynenbreugel *et al* 1995, Loubele *et al* 2006a), so far only few studies have assessed the accuracy of CBCT (Marmulla *et al* 2005, Kobayashi *et al* 2004, Lascala *et al* 2004). In the approach presented in this paper, we assess the quality of bone models derived from CBCT in the context of oral surgical planning by comparison with similar models derived from corresponding MSCT data sets. Geometric differences between bone models constructed from MSCT and CBCT are evaluated for measurements of bone thickness collected at a large number of anatomically corresponding sites in both models, which are automatically identified by CBCT to MSCT image registration (Maes *et al* 1997). The proposed validation procedure does not require an absolute geometric ground-truth to evaluate the quality of CBCT imaging, but instead uses MSCT as a clinically established method of reference. Moreover, our approach is completely automated and is observer independent, which yields reliable and reproducible results. The developed approach is illustrated on four different datasets acquired with three different CBCT scanners, involving both phantom and patient images.

3.3 Material and methods

3.3.1 Image datasets

Four different datasets were used in this pilot study involving three different CBCT scanners: the NewTom 9000 DVT (Quantitative Radiology, Verona, Italy), the I-CAT (Imaging Sciences International, Hatfield, PA, USA) and the Accuitomo 3D (J. Morita, Kyoto, Japan). Each dataset contains one or more CBCT images, acquired with one of these three scanners, and a reference image, acquired with MSCT.

Dataset 1, provided by the Karolinska Institutet, Sweden, consists of a CBCT 3-D image dataset of the maxilla of an anthropomorphic Rando head phantom (Alderson Research Laboratories, Long Island City, NY, USA) acquired with the NewTom 9000 DVT and a corresponding MSCT image acquired with the Somatom VolumeZoom (Siemens, Erlangen, Germany). No geometrical ground truth of the bone objects of interest

was available in this study, as the nature of the Rando phantom does not allow for physical measurements.

Dataset 2 was acquired at our institute and consists of images of a different Rando head phantom acquired with the Accuitomo 3D and with the Somatom Volume-Zoom. Because of the small imaging volume of the Accuitomo 3D (about 4 cm in diameter and 3 cm in height), four different CBCT images were acquired, namely of (1) the frontal and posterior region of the mandible, (2) the premolar and the molar region of the mandible, (3) the frontal region of the maxilla and (4) the posterior region of the maxilla.

Datasets 3 and 4 consist of a 3-D i-CAT CBCT image of the mandible and of the maxilla respectively of two patients who underwent oral implant surgery (dataset 3: 58 year female; dataset 4: 57 year male). These images were provided by the i-CAT manufacturer (Imaging Sciences International, PA, USA), together with corresponding MSCT images of the same patients, acquired with a LightSpeed QX/I (GE Medical Systems, Milwaukee, WI, USA), which were used for pre-operative image-guided oral implant planning.

All CBCT and MSCT images in these datasets were acquired using dental CT imaging protocols suited for image-guided oral surgery planning, as recommended by the manufacturers. The relevant imaging parameters are summarized in Table 3.1. Acquired images were saved as DICOM (Digital Imaging and Communications in Medicine) and transferred to a DELL Precision 530 personal computer (Dell Inc., Round Rock, TX, USA). The two-dimensional (2-D) axial DICOM image series were transformed into a 3-D image matrix using the DCMTK DICOM Toolkit (Offis, Oldenburg, Germany). Example images for each scanner are shown in Figure 3.1.

3.3.2 Bone segmentation

Bone is segmented in both the CBCT and MSCT images using a global threshold approach, i.e. a single threshold is used to segment the whole object everywhere in the image. The threshold value is defined for the CBCT and MSCT images individually by histogram analysis based on the algorithm described in (Baillard and Barillot, 2000), which we implemented in Matlab (The MathWorks, Inc., Natick, MA, USA). For each image, the histogram of image intensities is constructed within a rectangular region of interest containing the bone structure to be segmented, whereby only intensity values

corresponding to bone and soft-tissue are considered by specifying a suitable lower intensity limit to exclude the image background. The histogram is modelled as a mixture of Gaussian distributions, which are fitted to the histogram with the Stochastic Expectation-Maximization (SEM) algorithm (Baillard and Barillot, 2000). The number of Gaussians depends on the form of the intensity histogram. For the MSCT images one Gaussian representing bone and one representing soft-tissue was sufficient, while for the CBCT up to five Gaussians were used. The intensity distributions for bone and soft-tissue are obtained by summing the Gaussians that are (manually) identified as representing bone or soft-tissue respectively. The threshold value for bone is defined as the intersection of both distributions (Figure 3.2). To exclude the stochastic part of the SEM algorithm, the threshold values are calculated five times and the mean value is used as the threshold value.

Table 3.1 Description of the MSCT and CBCT dental protocols of each dataset.

	Image	Tube voltage (kV)	Tube current x time mA(s) ^a	FOV (mm)		Voxelsize (mm)		Number of voxels		Reconstruction filter
				X, Y	Z	X, Y	Z	X, Y	Z	
1	<i>NewTom 9000</i>	110	2.3	128	33	0.25	0.3	512	110	n.a.
	<i>Volume Zoom</i>	120	90	150	90	0.29	0.3	512	301	U70u
2	<i>Accuitomo 3D</i>	80	4	40	30	0.125	0.5	325	61	n.a.
	<i>Volume Zoom</i>	120	90	250	76	0.49	0.4	512	190	H60s
3	<i>i-CAT</i>	120	24	160	110	0.25	0.25	640	440	n.a.
	<i>LightSpeed QX/I</i>	120	90	147	83	0.29	0.5	512	166	Bone
4	<i>i-CAT</i>	120	24	160	110	0.4	0.4	400	274	n.a.
	<i>LightSpeed QX/I</i>	120	90	360	76	0.33	1.25	512	61	Bone

^aas set by the operator; effective mAs for MSCT, mean mA for CBCT. n.a not applicable

For each dataset, a suitable region of interest is defined in the CBCT images and transferred onto the MSCT image based on the registration between both images (see further), such that the threshold is defined in anatomically identical regions in both images.

For the CBCT images, bone threshold values are computed twice for the same region of interest, once based on the original intensities and once after 3-D Gaussian smoothing of the image data using an isotropic 3x3x3 Gaussian kernel with a standard

deviation of one voxel. The effect of noise suppression on bone segmentation accuracy is investigated by performing the bone thickness analysis as described below for both the original and the smoothed CBCT-image.

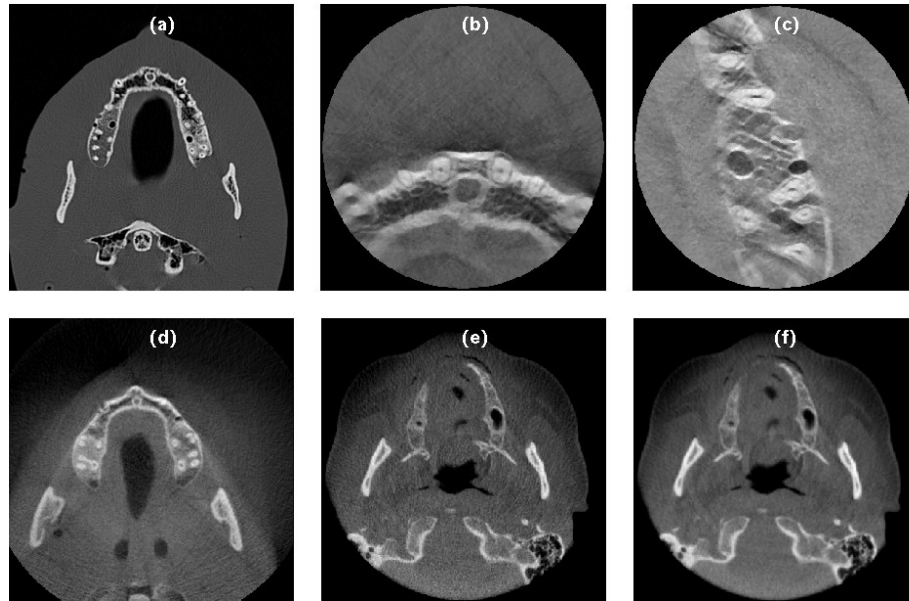


Figure 3.1 Example images of the various datasets used in this study: (a) MSCT image of a Rando anthropomorphic head phantom (dataset 2); (b, c) CBCT images of the same phantom acquired with the 3D Accuitomo scanner: (b) frontal maxilla, (c) posterior maxilla (dataset 2); (d) CBCT image of a different Rando phantom acquired with the NewTom 9000 DVT (dataset 1); (e, f) CBCT patient image acquired with the I-CAT scanner (dataset 3): (e) original image; (f) smoothed image.

3.3.3 Validation

To assess the image quality of the bone models generated from the CBCT images, bone thickness values measured in the CBCT images are compared with thickness values measured at anatomically corresponding points in the MSCT images. This validation is done in the following three steps.

3.3.3.1 Reference model

From the MSCT images, a 3-D surface model of the bone structure of interest is derived (Figure 3.3). This model is used to define a dense collection of measurement sites distributed all over the surface at which bone thickness is measured and compared with the

corresponding CBCT measurements. To construct this model, bone in the MSCT images is segmented by a global threshold as described above, resulting in a binary bone mask. Holes in the bone segmentation, resulting from differences in CT intensity between the more dense cortical bone and the interior trabecular bone, are filled using binary morphological operations implemented with the SCD Morphology Toolbox for Matlab (SCD Information Systems, Naperville, IL, USA). A triangulated model of the outer cortical bone surface is extracted from a smoothed version of the segmented object using the marching cubes algorithm (Lorensen and Cline, 1987). In each point of the surface, a measure line is defined perpendicular to the bone surface at that point. Along this line bone thickness is measured in both the MSCT and CBCT-images, after proper registration of both images.

3.3.3.2 Image registration

The CBCT images are geometrically aligned with the corresponding MSCT images by automated image registration using maximisation of mutual information (Maes *et al* 1997) (MMI). This method computes a 6-parameter rigid transformation T (i.e. a combination of a 3-D translation and a 3-D rotation) that maps every location in the CBCT image volume onto the anatomically corresponding location in the MSCT image volume by maximizing the statistical dependence between intensity values of corresponding voxels in both images. The MMI criterion does not require pre-processing of the images, is not affected by differences in contrast between CBCT and MSCT, is largely insensitive to image artefacts (Maes *et al* 1997) and has been demonstrated to yield subvoxel registration accuracy (West *et al* 1997). The registration is initialised by manually indicating a single landmark in both images, which defines initial values for the translation parameters of the registration transformation. The MMI registration algorithm is then applied as described by Maes *et al* (1997), with the same settings for the parameters of the iterative optimisation procedure, whereby the full extent of the CBCT image volume is considered for computing the similarity measure. After registration, measure lines defined in the MSCT image can be transferred onto the CBCT image through the inverse transformation T^{-1} , such that bone thickness measurements along these lines in each image are at anatomically identical locations and can be directly compared.

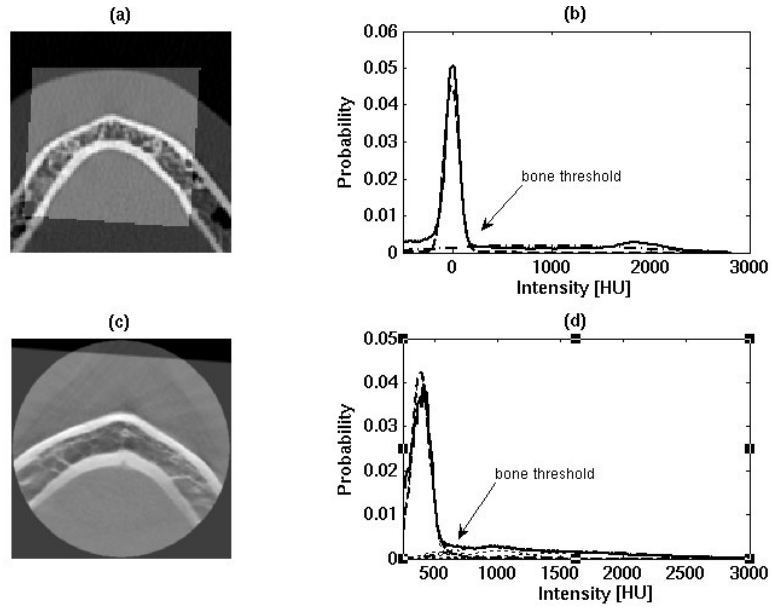


Figure 3.2 Histogram-based calculation of the bone threshold value for the MSCT (a, b) and CBCT (c, d) images of dataset 2 (frontal mandible). A region of interest is defined in the CBCT image (c) and transferred into the MSCT image (a). The intensity histogram within this region (b, d) is represented as a mixture of Gaussians, each corresponding to either bone or soft-tissue. The bone threshold is determined as the intersection of the bone and soft-tissue distributions.

3.3.3.3 Thickness measurement

One-dimensional (1-D) intensity profiles are extracted along corresponding measure lines in the MSCT and CBCT images by 3-D trilinear interpolation of the (original or smoothed) image intensities at equidistant points between the begin and end point of each line (Figure 3.4). The sample distance was identical for both images and determined for each dataset independently as one half times the smallest voxelsize of both images. The intersections of each measure line with the bone surface are extracted by a threshold of its 1-D intensity profile, using the global bone thresholds defined as described above. Linear interpolation of the profile values is used to locate candidate intersection points at sub-voxel precision. If more than 2 candidates are found, which is typically the case when the bone consists of two cortical structures surrounding a spongy part, the 2 locations retained are those closest to the reference bone surface derived from the MSCT images as described above.

Bone thickness along each measure line at corresponding sites in MSCT and CBCT, for which valid boundary points could be extracted, is measured by the distance $|ab|$ or $|a*b*|$ respectively as indicated in Figure 3.4. Geometric accuracy of the bone model derived from CBCT, relative to MSCT is evaluated by the mean and the standard deviation of the difference in bone thickness $|a*b*| - |ab|$ over all measure lines. The statistical significance of geometrical differences between the MSCT and CBCT derived bone models is assessed by a paired t-test on corresponding thickness measurements ($P < 0.05$).

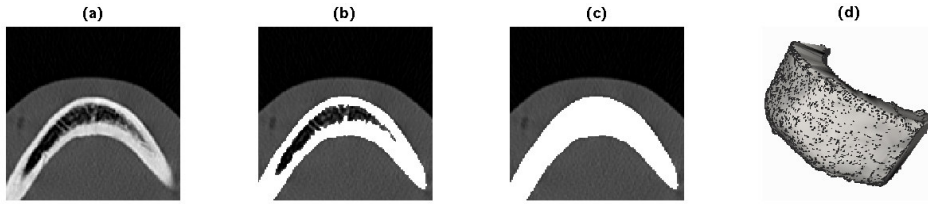


Figure 3.3 Generation of measure lines for bone thickness measurements: (a) MSCT image; (b) Bone segmentation obtained by a global threshold of (a); (c) Filled segmentation obtained by mathematical morphology operations acting on (b); (d) 3-D Bone surface extracted from (c). Measure lines are defined at a large number of surface points (indicated by black dots in (d)) along the normal to the surface.

3.4 Results

The bone threshold values determined for each dataset are tabulated in Table 4.2. The threshold values for CBCT for dataset 2 vary widely for different structures, which were all imaged using separate acquisitions due to the limited field of view of the Accuitomo 3D scanner. The threshold values for the smoothed CBCT images are for each case lower than the values determined for the original images. The final models are shown in Figure 3.5. The measurements of bone thickness differences between CBCT and MSCT are summarized in Table 3.3. The results show a statistically significant difference between the MSCT and CBCT thickness measurements for all experiments varying between 0.05 ± 0.47 mm (dataset 3, I-CAT) up to about 1.2 ± 1.0 mm (dataset 2, Accuitomo 3D, posterior maxilla). This corresponds to a difference up to about 1 to 1.5 MSCT voxels. For the Accuitomo 3D (dataset 2) and the i-CAT (dataset 3,4) smaller bone thickness values were obtained with CBCT than with MSCT, whereas for the NewTom 9000 DVT (dataset 1) larger bone thickness was measured with CBCT than with MSCT. Smoothing

of the CBCT image using a small $3 \times 3 \times 3$ Gaussian kernel reduces the mean difference between CBCT and MSCT thickness measurements by about 30% in almost all cases, except for the NewTom 9000 DVT where an increase of the mean difference of about 40% (from 0.53 to 0.73 mm) is observed. In those cases for which thickness values are available for the maxilla and the mandible acquired with the same CBCT scanner (dataset 2: Accuitomo 3D, and dataset 3 and 4: i-CAT), the differences found for the mandible are smaller than for the maxilla. For the Accuitomo 3D (dataset 2) the frontal parts of mandible and maxilla yield smaller thickness differences compared to MSCT than the posterior parts (-0.69 and -0.74 mm versus -0.96 and -1.19 mm respectively).

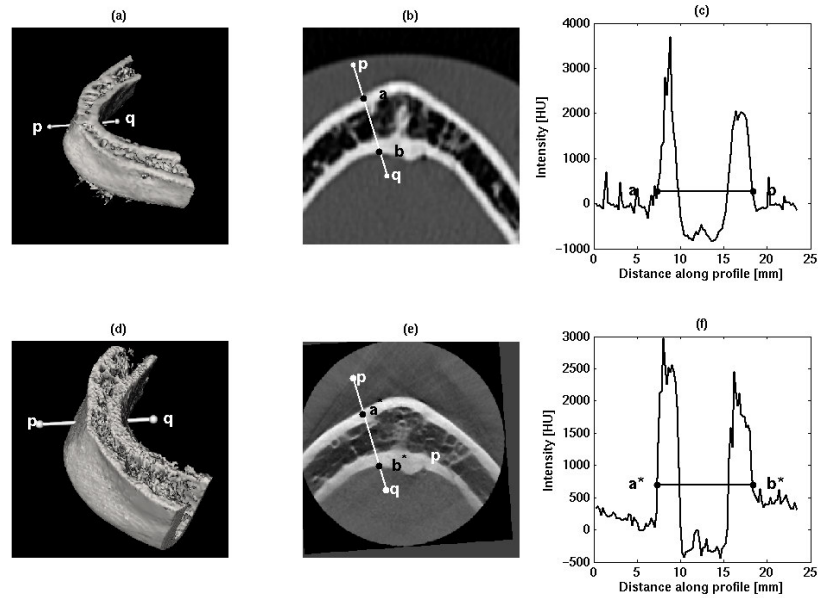


Figure 3.4 Illustration of the validation method for the frontal part of the mandible, imaged with the Accuitomo 3D (dataset 2). A measure line pq is defined orthogonal to the bone segmentation (a) obtained from the MSCT image (b) as illustrated in figure 3.3. This measure line is transferred to the anatomically corresponding location in the bone segmentation (d) derived from the CBCT image (e) after registration of both images. The intensity profiles (c, f) across the measure lines are calculated from the MSCT (b) and CBCT (e) images respectively.

Table 3.2 Difference in bone thickness as measured at anatomically corresponding sites in CBCT (original and smoothed data) relative to MSCT for each dataset: number of measure lines (N), number of valid CBCT and MSCT measurements (N_v), CBCT thickness difference versus MSCT (mean, standard deviation and 95% confidence interval).

	Object	N	Thickness (mm)	CBCT	N_v	Difference (mm)	
1	Maxilla	4637	9.42 ± 3.78	Original	4473	$+0.53 \pm 0.59$	[+0.51,0.54]
				Smoothed	4473	$+0.73 \pm 0.62$	[+0.71,0.75]
2	Frontal mandible	3006	12.93 ± 3.33	Original	2791	-0.69 ± 0.60	[-0.71, -0.66]
				Smoothed	2799	-0.48 ± 0.66	[-0.51, -0.46]
	Posterior mandible	569	10.80 ± 1.84	Original	462	-0.96 ± 0.65	[-1.02, -0.90]
				Smoothed	494	-0.61 ± 0.69	[-0.67, -0.54]
	Frontal Maxilla	1556	9.00 ± 2.45	Original	1274	-0.74 ± 0.78	[-0.79, -0.70]
				Smoothed	1289	-0.52 ± 0.80	[-0.60, -0.52]
	Posterior maxilla	1829	12.08 ± 4.18	Original	753	-1.19 ± 1.00	[-1.26, -1.12]
				Smoothed	1293	-0.71 ± 1.00	[-0.76, -0.65]
3	Mandible	5713	10.51 ± 2.93	Original	5581	-0.05 ± 0.47	[-0.06, -0.04]
				Smoothed	5571	$+0.03 \pm 0.47$	[+0.02,0.04]
4	Maxilla	4245	8.20 ± 4.44	Original	3789	-0.67 ± 0.59	[-0.69,-0.65]
				Smoothed	3836	-0.41 ± 0.61	[-0.43, -0.39]

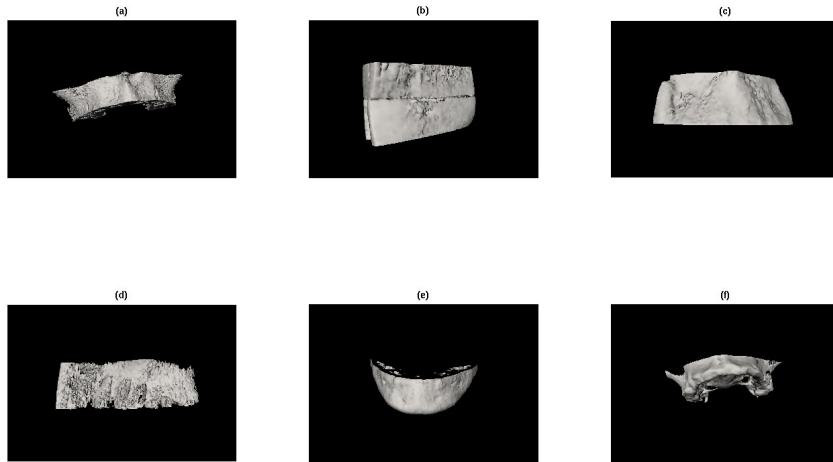


Figure 3.5 3-D renderings of the bone models obtained by segmentation of the various CBCT datasets used in this study: (a) maxilla (dataset 1, NewTom 9000 DVT); (b, c, d) frontal mandible, frontal maxilla and posterior maxilla (dataset 2, Accuitomo 3D); (e) mandible (dataset 3, i-CAT); (f) maxilla (dataset 4, i-CAT). Smoothing of the CBCT data was applied prior to segmentation for all images shown, except for (a).

3.5 Discussion

We assess the geometric accuracy of bone models segmented from CBCT by comparing bone thickness measurements at anatomically corresponding sites in similar models extracted from MSCT data. Our method relies on a correct geometric alignment or registration of the CBCT and MSCT images. The rigid-body MMI registration approach has been proven to be subvoxel accurate compared to external marker-based segmentation (West *et al* 1997). Hence, for this study, we can assume that the anatomical correspondence established between the MSCT and CBCT image volumes has an accuracy better than 0.5 mm everywhere in the image, provided that the impact of possible temporal changes between the CBCT and MSCT acquisitions on the rigid-body registration accuracy of the bone objects can be neglected when patient images are considered (datasets 3 and 4). The impact of registration errors on the CBCT thickness measurement is much smaller, considering that offsets due to an error in the registration in the location of the first bone surface point in CBCT relative to MSCT along each measure line (i.e., the location of point a^* in Figure 3.4 relative to point a) will be largely compensated for by similar offsets for the second point (points b and b^* in Figure 3.4). This was evaluated for dataset 1 (NewTom 9000 DVT) by computing the offsets along each measure line between the ideal bone surface locations (points a and b) and the corresponding CBCT-derived locations (points a^* and b^* , respectively). The average offsets were -0.33 ± 0.44 mm for $|aa^*|$ and $+0.20 \pm 0.37$ mm for $|bb^*|$, which is consisted with an average thickness increase of 0.53 mm. The absolute point location differences were 0.42 ± 0.35 mm and 0.31 ± 0.28 mm for $|aa^*|$ and $|bb^*|$, respectively. Because the difference in thickness is on average quite symmetrically distributed over both bone surface locations (0.33 and 0.20 mm, respectively), it can be concluded that the registration error is small and that the measured thickness difference is primarily a result of segmentation differences between both scans. The registration error component of the bone surface location error at the individual points a or b for dataset 1 can be estimated as $(-0.33 + 0.20)/2 = -0.07$ mm, while the segmentation error component is $\pm(0.33 + 0.20)/2 = \pm 0.26$ mm (-0.26 mm at point a , $+0.26$ mm at point b).

While datasets 1 and 2 in this study involve images of phantom objects, datasets 3 and 4 contain images of live patients. Patient scans may suffer from motion-related artefacts that may affect segmentation accuracy. The presence of such artefacts in the

CBCT image would likely be reflected in an increased bone thickness difference with respect to MSCT. However, similar artefacts in the MSCT image could possibly spoil the absolute accuracy of the MSCT-derived bone model and could induce (local) differences between the MSCT and CBCT bone models, which our approach would incorrectly attribute to errors in the CBCT segmentation, while it is in fact the MSCT reference itself that is (locally) not reliable. Hence, the fact that we use MSCT as a method of reference for evaluating the relative geometric accuracy of CBCT assumes that a sufficiently accurate segmentation can be obtained from the MSCT image, i.e., in agreement with clinical requirements almost everywhere along the bone surface.

A particular advantage of our registration-based validation approach is that measurements can be automatically performed in a reproducible way at a very large number of sites distributed all over the surface of the object of interest. This is not feasible with, for instance, manual measurements by a human observer, which are time-consuming and subject to intra- and inter-observer variability. Our registration-based validation approach, on the contrary, is observer independent, such that our results are not confounded by observer subjectivity. Averaging over a large number of measurements increases the statistical significance of the results and takes the whole object into account, although a more local analysis of regional accuracy would also be feasible with our approach, but was not pursued here.

In the current study, bone segmentation was performed by a global threshold using object-specific bone threshold values derived by a robust procedure involving regional intensity histogram analysis. This approach avoids the need for observer-specified threshold values. The use of a single threshold value for the entire object has the additional advantage that only a single segmentation parameter has to be estimated. The pitfall of using a more complex segmentation protocol would be that the validation results would become more sensitive to an optimal choice of the segmentation parameters and that the study would have to focus more on the segmentation performance of various protocols rather than on differences in image quality of the different modalities under study. Egger *et al* (2005) and Aamodt *et al* (1999) evaluated the use of 1 single global threshold value for bone segmentation in CT. This approach is not feasible for segmentation of the mandible and the maxilla in CBCT because of the large intensity differences that occur between distinct bone structures in the same image, between various patients,

and between different scanners, as can be seen in Table 4.2. Instead, threshold values were determined for each dataset and each object of interest separately. Prevrhal *et al* (1999) investigated the accuracy of bone segmentation using a local threshold based on the 50% rule and the maximum gradient criterion and concluded that the 50% threshold value gave better results than the maximum gradient approach. This method was not preferred in the present study because this local threshold value can only be calculated after performing initial bone segmentation (which further increases the number of segmentation parameters that need to be tuned).

The impact of the choice of the threshold value on geometric accuracy was investigated for dataset 1. The CBCT threshold value was varied in the range 0-500 and for each value the number of valid CBCT measurements and the mean difference in bone thickness relative to MSCT was computed (Figure 3.6). The threshold value as determined by histogram analysis (276.8) is found to maximize the number of valid CBCT measurements at near 98% of all measurements, with an average thickness difference over all valid measurements of 0.53 mm. The average thickness difference can be reduced to almost zero by selecting a higher CBCT threshold of about 400, but this reduces the number of valid measurements by about 10%, meaning that this threshold yields an unreliable segmentation for about 10% of the bone surface. For all datasets, the mean difference in bone thickness between CBCT and MSCT was found to be smaller than 1 mm, except for the posterior part of the maxilla in dataset 2 acquired with 3D Accuitomo (1.2 mm). Hence, notwithstanding the statistically significant difference between the CBCT and MSCT measurements, the discrepancy between both systems is generally at a submillimetre level and likely to be clinically acceptable, although further study would be required to confirm this. The standard deviation of the thickness difference between CBCT and MSCT was smaller than 0.7 mm for most datasets. A low standard deviation implies that a nice-looking, smooth bone surface was obtained from the CBCT data, which mimics the reference MSCT bone model well. Higher standard deviations (up to 1 mm) were found for both the frontal and posterior parts of the maxilla imaged with the Accuitomo 3D (dataset 2), indicating a less smooth 3-D segmentation. Moreover, the percentage of measure lines along which a valid measurement could be performed by the global threshold operation is generally much lower for the Accuitomo 3D than for the other scanners. Especially for the posterior part of the maxilla in dataset 2, local disconti-

nities were observed in the CBCT-derived bone surface, which makes this segmentation not clinically usable. The reason for the inferior quality of these models is that significant intensity inhomogeneity can be observed within the bone; the cortical bone on one side of the object having higher intensities than on the other side, as illustrated in Figure 3.7. This artefact should be corrected to improve the quality of the bone segmentation (Hsieh *et al* 2000). The use of a more sophisticated segmentation algorithm that takes such intensity inhomogeneity into account is an interesting avenue for further research.

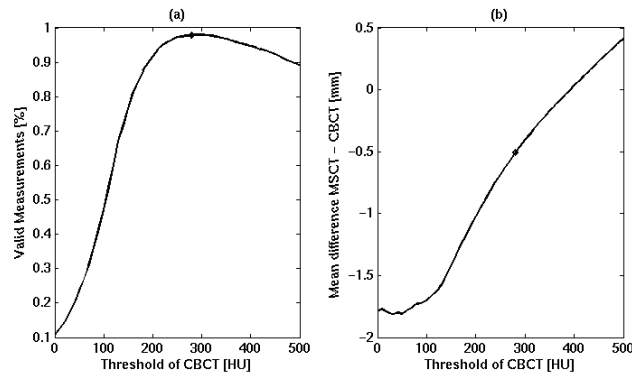


Figure 3.6 Impact of the bone threshold selection on geometric accuracy for dataset 1 (a): number of valid CBCT measurements in function of the threshold; (b) mean bone thickness difference over all valid measurements in function of the threshold. The threshold value as determined by histogram analysis (276.8) is indicated by the black dot.

The current study includes only a limited number of datasets, supplied by different institutes and acquired using different CBCT and MSCT imaging devices and different imaging parameters, involving both anthropomorphic phantom data and patient images. This study therefore does not aim at a comparative evaluation of the geometric accuracy of different CBCT scanners, but instead serves to demonstrate the general applicability of our registration-based validation approach in cases where no geometric ground-truth can be established. In the future, we plan to apply the method in a more extensive study of the geometric accuracy of bone models segmented from CBCT, comparing the image quality of different scanners in a more systematic and standardized manner based on images acquired from the same objects. Of particular interest is investi-

gating the impact on image quality of differences in radiation dose between different CBCT systems.

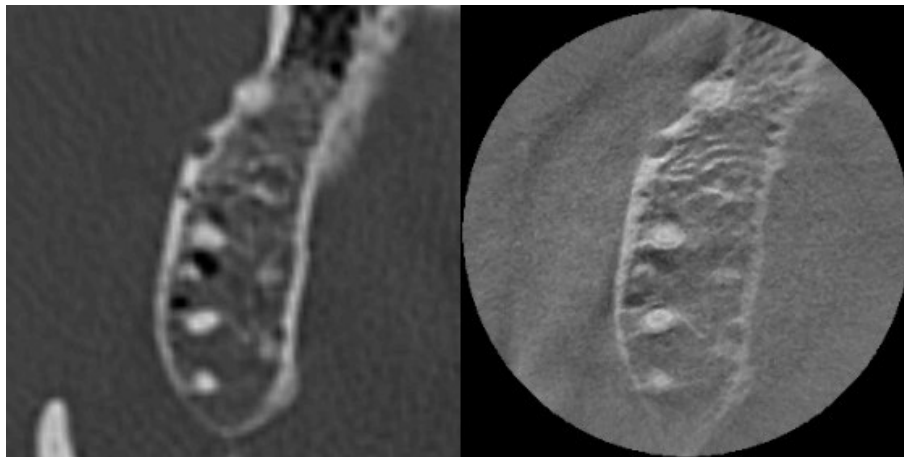


Figure 3.7 Co-registered MSCT (left) and CBCT (right) images of dataset 2 (Accuitomo 3D, posterior maxilla). The CBCT image is an original axial slice as acquired by the scanner, whereas the MSCT image was created by reslicing the 3-D image data volume according to the registration transformation between both images. While the cortical bone is clearly outlined in the MSCT image, local differences in contrast can be perceived in the Accuitomo 3D CBCT image, which complicates its segmentation by a global threshold.

3.6 Conclusion

In this article, a method is presented for evaluating the quality of bone models generated from CBCT in the context of oral surgery planning by comparison with conventional MSCT imaging of the same objects, which is considered as the clinical gold standard. Anatomical correspondences between both images are automatically established by image registration, such that corresponding bone thickness measurements can be extracted from both images and compared at a large number of sites distributed all over the bone surface. A pilot study involving both phantom and patient data acquired with 3 different CBCT scanners (NewTom DVT 9000, i-CAT, Accuitomo 3D) demonstrates the general applicability of our validation approach.

Chapter 4

Assessment of bone segmentation quality of CT scanners using laser scanning

4.1 Abstract

We present a protocol for the evaluation of the geometric accuracy of bone segmentation algorithms in multi-slice and cone-beam computed tomography (CT). Three important issues are resolved in this protocol: construction of a skull phantom with an accurate geometrical description serving as gold standard; registration between this geometric model and the 3-D CT images; and a quality measure to evaluate the segmentation accuracy. A 3-D model of a dry skull phantom is obtained using a high-resolution laser scanner. CT images are acquired of the phantom immersed in a water-containing head mould to mimic the presence of soft tissues. The geometric accuracy of bone objects derived by segmentation of the CT images using an optimal threshold is evaluated by comparison with the ground-truth provided by the laser-scanned model. Anatomical correspondences between the laser model and the CT images are automatically established by image registration, such that bone thickness measurements in both modalities can be compared at a large number of anatomically corresponding sites distributed along the bone surface. The protocol provides a standardized methodology to evaluate the image quality of bone models for various CT scanners.

4.2 Introduction

In surgical simulations, bone models are used for planning of oral implant placement or maxillofacial surgery. Such bone models are typically obtained from image data acquired with multi-slice spiral computed tomography (MSCT), using a segmentation algorithm for extracting bony tissues and applying the marching cubes algorithm (Lorensen and Cline, 1987) for generating a triangulated model of the bone surface. For successful bone surgery planning and simulation it is important that the geometric accuracy of the bone model is known.

This paper presents a protocol for the evaluation of the accuracy of bone segmentation algorithms in computed tomography (CT) scanners and is the extension of a method that

was previously developed in our research group (Chapter 3, Chapter 4). To develop this protocol three important issues need to be resolved: construction of a phantom object with an accurately known geometrical description which serves as the gold standard, a registration method between this geometric description and the 3-D CT data acquired of the phantom and a quality measure to evaluate segmentation accuracy. The proposed method was used to evaluate the image quality of the I-CAT (Imaging Sciences International, Hatfield, Pennsylvania, USA) cone beam CT (CBCT) scanner and of the Somatom Sensation 16 (Siemens, Erlangen, Germany) multi-slice spiral CT scanner (MSCT) scanner.

4.3 Material and Methods

4.3.1 Constructing a semi-anthropomorphic skull-phantom

The traditional skull phantoms that are used to assess the image quality of CT scanners consist of a dry human skull embedded in a solid soft-tissue simulating material (e.g. 3M, Minnesota, USA). Due to the construction of these phantoms it is not possible to acquire a geometrical description of the dry skull in a non-destructive way, which makes these phantoms not suitable to use as a gold standard for the validation of segmentation accuracy. A dry skull of a person who donated his body for research and which was kindly provided by the Department of Morphology, University of Hasselt (Belgium) was used for the construction of this phantom. This skull was cut into four parts: the mandible, the calvarium, the left zygoma and left part of the maxilla, and the right zygoma and part of the maxilla. The four different parts were scanned with an XC50 Cross Scanner (Metris, Leuven, Belgium) with three laser planes, mounted on a Wenzel LH57 3-D coordinate measurement machine. With this laser scanner it is possible to obtain surfaces in the form of a point cloud with an accuracy of 15 μm . Having the skull cut into four pieces, it was possible to acquire the outer and inner bone surface in one acquisition, allowing to measure bone thickness along the point cloud. After acquiring the laser scan, the skull was placed in a head mould enclosure filled with water for soft-tissue simulation.

4.3.2 Registration between volumetric CT data and the point cloud of the laser scanner

Before registering the CT data and the point cloud (Figure 4.1 (a)) derived from the laser data, the point cloud is transformed into a volumetric dataset. Using the FastRBF Interpolation Toolbox (FarField Technology Limited, Christchurch, New Zealand), an implicit function was derived through the point cloud, which has a value of zero on the surface, negative values within the scanned object, and positive values outside the object. This function is evaluated on a 3-D grid to generate a volumetric representation of the laser-scanned surface (Figure 4.1 (d)). The CT images (Figure 4.1 (c)) are geometrically aligned with the volumetric image (Figure 4.1 (d)) derived from the laser scanner by automated image registration using maximization of mutual information (Maes *et al* 1997). This method computes a 6-parameter rigid transformation T (i.e. a combination of a 3-D translation and a 3-D rotation) that maps every location in the CT image volume into the anatomically corresponding location in the volumetric image of the laser image by maximizing the statistical dependence between intensity values of corresponding voxels in both images.

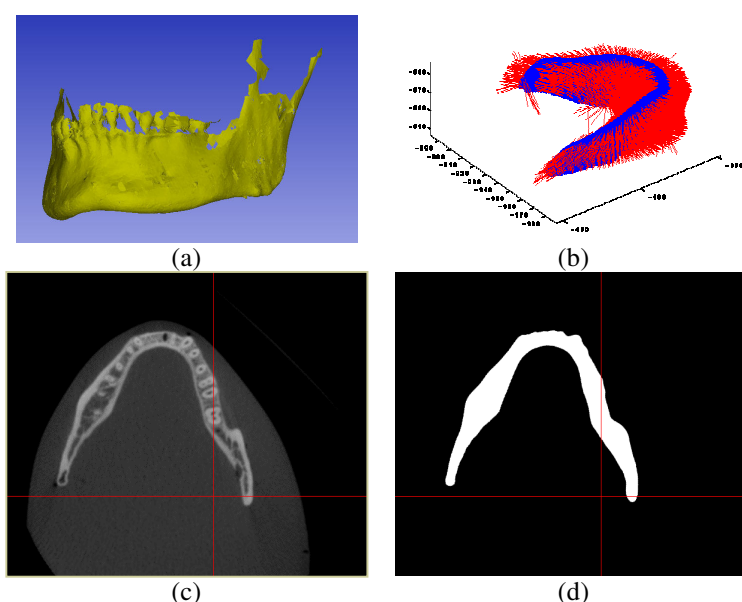


Figure 4.1 This figure gives an overview of the method for the validation of the image quality by comparing a 3-D laser scan (a) with a CT image (c). Using implicit functions, the point cloud is converted to a label image (d), which is registered to the CT image (c). The validation is performed along boundary points on the point cloud (b).

4.3.3 Definition of the quality measure

For the evaluation of the CT image quality, a measure needs to be defined. In this paper the error on the bone thickness measured on the bone model will be used as the quality measure. To evaluate this error, measure lines are defined along the bone surface in the laser model, which are transferred to the CT image based on the transformation calculated in the previous section.

For the definition of the measure lines, a cylindrical grid with the vertical axis through the centre of mass of the object as z-axis was calculated. This is the central axis of a cylindrical grid defined by a vertical increment Δz and an angular increment $\Delta \theta$. In all the elements $(i\Delta z, j\Delta \theta)$ of the cylindrical grid where bone exists, a measure line is defined by two points on the bone surface along a radial line through this element one point nearest the z-axis and one point farthest the z-axis. The result of the calculation of these measure lines is shown in Figure 4.1 (b).

Across these measure lines 1-D intensity profiles are calculated by 3-D trilinear interpolation of the image intensity at equidistant points between the beginning and the end point of each line. Sample distance was 0.1 mm. The intersections of each measure line with the bone surface are extracted by a threshold of its 1-D intensity profile using a global bone threshold. Linear interpolation of the profile values is used to locate candidate intersection points at sub-voxel precision. If more than 2 candidates are found, which is typically the case when the bone consists of two cortical plates surrounding spongy middle, the locations that are retained are those closest to the reference bone surface derived from the laser data.

4.3.4 Determination of the threshold value

Bone segmentation based on a global threshold can be defined as finding the intensity which defines the transition between bony tissue and soft-tissue. Wiemker and Zwartkruis (2001) showed that this transition corresponds to a local optimum in the cumulative Laplace-weighted histograms. In some cases an optimum of the surface histogram, the mean gradient histogram, the volume histogram or the sphericity histogram can give more information to find the ideal threshold value. The quality of the different threshold values can be evaluated by calculating the mean difference of the thickness

measured on the laser data and the CT data and finding the threshold value that yields the smallest absolute mean error.

4.3.5 Evaluation of the quality measure

To evaluate image quality, the mean and standard deviation of the difference between thicknesses measured on the laser data and the CT data are calculated. As a third quality measure, the number of valid measurements is assessed. The latter corresponds to the number of measures lines, from which it is possible to calculate the bone thickness with the given threshold value.

4.3.6 Evaluated scanners

One CBCT scanner, I-CAT (Imaging Sciences International, Hatfield, Pennsylvania, USA) and one MSCT scanner Sensation 16 (Siemens, Erlangen, Germany) were evaluated in this study. For the I-CAT all the different protocols provided by the manufacturer were evaluated (Table 4.1). For the MSCT scanner, a protocol used for orthodontic indications was selected. The MSCT images were reconstructed with bone and soft tissue reconstruction filters.

Table 4.1 Characteristics of the evaluated protocols on the i-CAT and Sensation 16.

		Protocol	Tube voltage (kV)	Tube current x time (mAs)	Voxelsize (mm)	Filter	Nb
<i>i</i> <i>-</i> <i>C</i> <i>A</i> <i>T</i>	<i>Im-plants</i>	Mandible	120	23.87	[0.4 0.4 0.4]	n.a.	1
		Mandible high		46.72	[0.2 0.2 0.2]		2
		Medium		12.48	[0.3 0.3 0.3]		3
		Medium		12.48	[0.4 0.4 0.4]		4
		2 arches		23.87	[0.4 0.4 0.4]		5
	<i>Ortho-dontic</i>	13 cm, 10 sec	120	12.48	[0.4 0.4 0.4]	n.a.	1
		13 cm, 20 sec		23.87	[0.3 0.3 0.3]		2
		13 cm, 20 sec		23.87	[0.4 0.4 0.4]		3
		13 cm, 40 sec		46.72	[0.25 0.25 0.25]		4
		13 cm, 40 sec		46.72	[0.4 0.4 0.4]		5
<i>Sensa-tion</i> <i>16</i>	<i>Ortho-dontic</i>	Head	120	90	[0.25 0.25 0.4]	H30s	1
						H60s	2

4.4 Results

In Figure 4.2 the histograms of the features considered for threshold selection are shown for orthodontic protocol 3 on the I-CAT with 120 kV and 23.87 mAs. The different histograms were calculated for a region of interest on the image that included the mandible (Figure 4.2 (a-f)). The mean difference between the thickness measured on the laser and the CT data was calculated for threshold values ranging from 200 HU till 1000 HU (figure 4.2 (g)). Figure 4.2 (g) shows that the optimum threshold value was 776 HU. This value was the best approximated by the first local optimum of the histogram of the mean gradient (Figure. 4.2 (c)).

Table 4.2 Results of the evaluation of the segmentation quality.

		<i>Nb</i>	Threshold (HU)	Mean \pm std (mm)	Valid profiles (%)
<i>i</i> - <i>C</i> <i>A</i> <i>T</i>	<i>Im-</i> <i>plants</i>	1	731	-0.08 \pm 0.54	96.43
		2	830	-0.01 \pm 0.59	95.07
		3	819	0.02 \pm 0.70	94.62
		4	829	-0.03 \pm 0.62	95.85
		5	858	-0.10 \pm 0.50	97.41
	<i>Ortho-</i> <i>dontic</i>	1	775	0.00 \pm 0.66	96.35
		2	775	-0.02 \pm 0.57	96.57
		3	761	-0.02 \pm 0.62	96.24
		4	742	-0.01 \pm 0.56	97.05
		5	731	-0.13 \pm 0.53	96.54
<i>Sensa</i> <i>tion 16</i>	<i>Ortho-</i> <i>dontic</i>	1	1047	0.20 \pm 0.56	97.27
		2	1000	0.14 \pm 0.60	95.18

4.5 Conclusion

A novel method is presented for evaluating the quality of bone models generated from CT scanners in the context of oral surgery planning by comparison with point clouds generated with a laser scanner acting as the gold standard. Anatomical correspondences between both images are automatically established by image registration as such that matching bone thickness measurements can be extracted for both images and compared at a large number of sites distributed all over the bone surface.

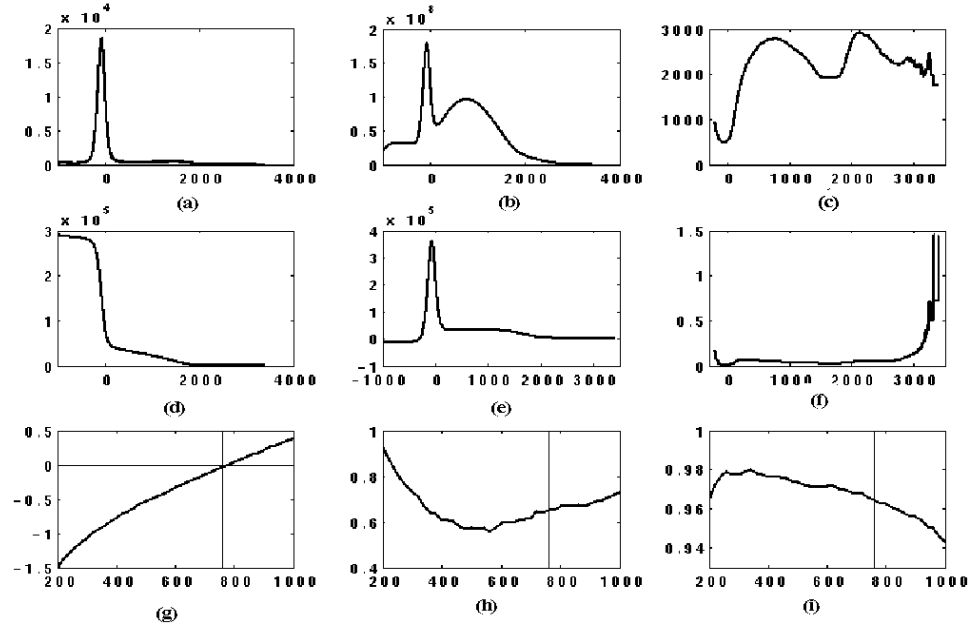


Figure 4.2. This figure gives the overview of the different optimisation methods which were used for searching the optimum threshold value for the bone segmentation for orthodontic 4 (120 kV, 23.87 mAs and [0.4 0.4 0.4] voxelsize): intensity histogram (a), total gradient (b), mean gradient (c), volume histogram (d), surface histogram (e), sphericity (f). The quality of a threshold value is evaluated by calculating the mean error (g) and the standard deviation (h) of the difference between the thickness calculated on the point cloud of the laser scanner and the thickness calculated on the scanner under consideration. As a last quality measure the percentage of valid measurements is calculated. These quality measures were evaluated for threshold values from 200 HU till 1000 HU (g, i).

Chapter 5

Geometric accuracy and radiation dose in 3-D scanners in dentomaxillofacial radiology

5.1 Abstract

The aim of this study was to investigate the relation between radiation exposure and image quality in the context of oral imaging applications for cone beam computed tomography (CBCT) compared to multi-slice computed tomography (MSCT). Four different CBCT scanners were evaluated: i-CAT, NewTom 3G, MercuRay, and Accuitomo 3D. The MSCT scanner that served as reference in our study was the Somatom Sensation 16. Different protocols were evaluated for each scanner. The radiation dose of each protocol was evaluated based on effective dose measurements with the anthropomorphic Rando Alderson phantom. The image quality was quantified by the contrast-to-noise ratio (CNR) and by the segmentation accuracy of objects with known dimensions consisting of different materials. The radiation dose of the Accuitomo 3D was found to be the lowest of all scanners investigated, but this scanner also has the smallest field of view. The NewTom 3G and the i-CAT had a lower radiation exposure than the MercuRay and the Somatom Sensation 16. The CNR was generally higher for the MSCT than for the CBCT scanners. While bone was segmented with sub-millimeter accuracy in all scanners, thin high-density aluminum structures could be quantified more accurately with the CBCT scanners than with MSCT. Based on these findings, it can be concluded that the CBCT scanners in dentomaxillofacial radiology provide more suitable images for this application.

5.2 Introduction

During the last decade there has been a trend to use 3-D scans in the dentomaxillofacial field. Besides the diagnosis of different pathologies, 3-D scans can be used for the generation of tangible solid models of human organs. Among these modelling techniques, stereolithography is well known for the high-quality models it can generate. If the fabrication of these models is submillimeter accurate, they can be used for the planning of oral or maxillofacial surgeries with Computer Aided Design (CAD) software and they can

eventually be used as a master or negative for prosthesis or implant production and also for intra-operative guidance (Suetens 2002). The segmentation of the anatomical structures out of 3-D scans is of primordial importance for the generation of accurate models. Traditionally dental scan protocols on computed tomography scanners were used for the generation of such models (Suetens 2002). The last years however, a lot of manufacturers have introduced cone-beam CT (CBCT) scanners dedicated for dentomaxillofacial radiology (Scarfe *et al* 2006, Guerrero *et al* 2006). The success of these CBCT scanners is mainly due to the decreased radiation dose compared to the traditional CT scanners (Schulze *et al* 2004, Ludlow *et al* 2006). Because of the widespread use of these scanners, it is obvious that these scanners will be used for the generation of 3-D models. However, because of difference in image quality between different CBCT scanners, the accuracy of such image generated models will also vary between scanners (Loubele *et al* 2006).

To compare the image quality of scanners in dentomaxillofacial radiology, mostly the accuracy of thickness measurements by observers is assessed (Marmulla *et al* 2005, Kobayashi *et al* 2004). Such studies are time consuming, not standardized and suffer from inter-and intra observer variability (Loubele *et al* 2006). There exist however not much correspondence between diagnostic performance and physical parameters of scanners. So the calculation of only physical parameters, does not give enough information to a dentist when he needs to decide about the choice of scanner that is appropriate for him. Therefore there is certainly a need for inclusion of segmentation quality in a protocol for performance of image quality, because the segmentation process mimics the delineation of a human observer. Due to the limited FOV of some of the scanners for dentomaxillofacial radiology (Guerrero *et al* 2006), it is not possible any more to use established phantoms for quality control like the Catphan Phantoms (The Phantom Laboratory, Salem, NY) for evaluation of image quality, because these phantoms cannot be imaged by some of the scanners.

It is obvious that the segmentation quality needs to be balanced with the radiation dose of the scanner. For the evaluation of the radiation dose with X-ray beams with a height of more than 10 cm, a case which can occur for almost all CBCT scanners, the CTDI is not a good dose measurement any more (Boone *et al* 2007). There does not exist yet an adequate solution for a technical dose measurement for which also a relation exists

with the effective radiation dose, it is still the best to evaluate the radiation dose of the different scanners with effective dose measurements in a Rando Alderson Phantom.

The main goal of this study was to evaluate and compare the radiation dose and image quality of one MSCT and four CBCT scanners used in dentomaxillofacial imaging. The radiation dose was measured both with anthropomorphic Rando Alderson phantoms. Image quality was evaluated by measuring the contrast-to-noise ratio (CNR) of each scanner, using two phantoms of the image quality kit provided with the scanner with the smallest FOV for compatibility reasons as mentioned above, and by assessing the accuracy of linear measurements. By relating image quality and radiation dose, a comparison of the performance of the different scanners could be made taking both aspects into account.

5.3 Material and Methods

5.3.1 Evaluated scanners

Image quality assessment was performed on one MSCT and 4 different CBCT scanners and dose measurements were performed on 3 CBCT scanners and 1 MSCT scanner. The MSCT scanner was the Somatom Sensation 16 (Siemens, Erlangen, Germany). The CBCT scanners were the i-CAT (Imaging Sciences International, Hatfield, PA, USA), the NewTom 3G (Quantitative Radiology, Verona, Italy), the MercuRay (Medico Technology Corporation, Kashiwa, Japan) and the Accuitomo 3D (Morita, Kyoto, Japan). On the MercuRay, no radiation dose was assessed. When we initiated this study, the different CBCT scanners were not available at many sites and hence measurements needed to be performed at different institutions. The measurements with the Somatom Sensation 16 and the Accuitomo 3D were performed at the University Hospital Leuven (Leuven, Belgium), with the NewTom 3G at the UCLA School of Dentistry (Los Angeles, CA, USA), with the MercuRay CB at SmartScan Imaging (Orange, CA, USA) and with the i-CAT at the Golden State X-ray Lab (North Hollywood, CA, USA) and at Imaging Sciences International (Hatfield, PA, USA).

Because the results of the evaluation of the image quality and the radiation dose of the different CBCT scanners are related to the design of each scanner, a comparison of the most relevant design parameters of these scanners is included in Table 5.1. For the CBCT devices there is less freedom as for the MSCT scanner in the selection of the ex-

posure parameters. This is especially the case for the selection of the FOV, the X-ray tube settings and the reconstruction parameters.

For all CBCT scanners the size of the FOV can be selected only from a fixed number of settings, while for MSCT almost all different FOV heights and diameters can be selected. For the CBCT devices either a spherical FOV (NewTom 3G, MercuRay) or a cylindrical FOV (i-CAT, Accuitomo 3D) is used.

For the NewTom 3G the parameters, which control the X-ray tube, cannot be freely selected by the operator because of the Automatic Exposure Control (AEC) of the scanner. The AEC calculates the optimal value of the tube current after an axial and a coronal scout view of the imaged scene. This feature of the scanner makes that the tube current may be different when image quality and radiation dose are evaluated with different phantoms, even when the same protocol was specified, which has to be taken into account when relating both. The i-CAT scanner allows selecting 3 different values of the scanning time, which result in a different number of basis images and another mAs setting. For the Accuitomo 3D and the MercuRay there is even more freedom to vary the tube voltage and tube current settings. It is also important to point out that the Accuitomo 3D and the MercuRay operate with a continuous exposure of the X-ray tube, while the i-CAT and the NewTom 3G work with a pulsed X-ray exposure.

In the reconstruction phase, only the NewTom 3G allows reconstructing the images with different reconstruction kernels ranging from a smooth reconstruction to a very sharp reconstruction.

Table 5.1 Properties of the evaluated CBCT scanners

	i-CAT	NewTom 3G	MercuRay	Accuitomo 3D
<i>Current (mA)</i>	5.5	15 ³	10 or 15	1-10
<i>Potential (kVp)</i>	120	110	60-120 (step 20 kV)	60-80 kV (step 1 kV)
<i>Scanning time (s)</i>	10, 20, 40	36	10	9, 18
<i>Exposure time (s)</i>	1.92, 3.67, 7.188	5.4	10	8.31, 16.02
<i>Exposure time of one frame (ms)</i>	12	15	33	30
<i>Current x exposure time for one frame (mAs)</i>	0.066	0.208 ³	0.347-0.521	0.030-0.300
<i>Basis images</i>	160, 306, 599	360	288	512
<i>Current x exposure time (mAs)</i>	10.56, 20.2, 39.53	75 mAs ³	100 or 150	8.31-83.1 or 16.02-160.2
<i>Focal spot (mm)</i>	0.5	0.5, 1.5	0.6	0.5
<i>Type of exposure</i>	Pulsed	pulsed	continuous	continuous
<i>Parameters selected by the operator</i>	Scanning time and scan height	size of the FOV	kV, mA for 1 frame, size of the FOV	Scanning time, kV, mA for 1 frame
<i>Patient positioning</i>	Sitting	supine	sitting	sitting
<i>Source to rotational Centre distance (cm)</i>	48.069	66.3	82.0	33.5
<i>Rotational center to detector distance (cm)</i>	20.51	28.5	29	34.9
<i>Source to sensor distance (cm)</i>	68.58	94.8	111.00	68.4
<i>Detector type</i>	Flat panel	CCD 12-bit	CCD 12-bit	CCD 8-bit
<i>Detector size (cm)</i>	20 x 25	Ø 15.24, 22.86 or 30.4	Ø 12 to 29	Ø 10.16
<i>Detector size (pixel)</i>	960 x 768	1000 x 1000	1024 x 1024	240 x 320
<i>Scan dimensions (cm)</i>	16 x 21, 16 x 13, 16 x 8, 16 x 6	10 x 10, 13 x 13, 18 x 18	51.2 x 51.2, 102.4 x 102.4, 150 x 150, 193.5 x 193.5	4 x 3
<i>Voxelsize in plane (mm)</i>	0.2-0.4	0.16-0.42	0.1-0.4	0.125
<i>Min reconstruction increment (mm)</i>	0.2 ²	0.16 ¹	0.1 ²	0.125 ¹

¹This is the minimal slice increment that can be selected.

²For these scanners, only cubical voxels are possible and the smallest dimension of cubical voxel is given.

³The NewTom 3G works with automatic exposure control, therefore in this table the value with maximum exposure is given.

5.3.2 Radiation dose assessment

The effective radiation dose of the MSCT and CBCT scanners was assessed using two Rando Alderson phantoms. The first phantom had slices with a uniform thickness of 2.5 cm, while the second phantom had slices of 2.5 cm for the body and 1 cm for the head. The experiments on the Somatom Sensation 16 were performed using the first phantom, while the experiments on the CBCT scanners were performed using the second phantom. For the dose measurements, thermoluminescent dosimeters (TLD) type TLD100 (Li:Mg,Ti) and TL100H (Li:Mg,Cu,P) (Bicron, Solon, OH) were used. The TLDs (55 in total for the first phantom, 75 for the second phantom) were inserted in the radiation sensitive organs and tissues of the phantom, namely in the red bone marrow and bone surface, the thyroid, the brain, the salivary glands and the skin. The location of these organs and tissues in the phantom was determined by visually comparing the slices of the phantom with an atlas of cross-sectional anatomy (Cahill and Orland, 1984). For the bone marrow and the bone surface the TLDs were distributed over the calvarium, the maxilla, the mandible, the ramus and the upper spine. For the salivary glands the TLDs were distributed over the submandibular gland, the sublingual gland and the parotid. The TLDs for measuring the skin dose were placed on the mouth and on the eyes. These TLDs are used for measuring the deterministic effect of the radiation dose, because due to the small surface of the skin, which is irradiated with these protocols, the skin dose does not contribute much to the effective radiation dose (Ludlow *et al* 2006).

For the dose measurements, first one or two scout views (depending on the scanner) were made to allow positioning of the phantom according to the protocol under investigation. In order to reach sufficiently high radiation dose levels for the TLDs and to lower the influence of the acquisition of the scout views on the dose values, each scan protocol was repeated 10 times without changing the position of the phantom in the scanner.

After radiographic exposure, the TLDs were analysed either by the Unit of Personal Dosimetry at the University Hospital Leuven (Leuven, Belgium) with a fully automated Harshaw 6600 reader (Bicron, Solon, OH) or by Global Dosimetry Solutions (Irvine, CA, USA) with a Harshaw 8800 Automated TLD Card Reader Workstation (Bicron, Solon, OH). The calibration of the TLDs was performed by measuring the dose

profile over a length of 10 cm both with an ion chamber and with strips of TLDs of 10 cm.

The mean radiation dose D_j of an organ j was calculated as (Golikov and Nikitin 1989):

$$D_j = \sum_{i=1}^n f_{i,j} D_{i,j} \quad (5.1)$$

with $f_{i,j}$ the fraction of the total organ mass of organ j in slice i of the Rando Alderson phantom, $D_{i,j}$ the average radiation dose of the TLDs situated in the organ j in slice i and n the total number of slices of the phantom. For the fractions $f_{i,j}$ the values defined by Golikov *et al* (1989) and Huda and Sandison (1990) were used.

The effective radiation dose E was calculated as:

$$E = \sum_{j=1}^m w_j D_j \quad (5.2)$$

with D_j the mean organ dose for each organ j as defined above and w_j the tissue weighting factors as defined in the latest recommendations (ICRP 2007).

5.3.3 Image quality assessment

5.3.3.1 Phantoms

We used two phantoms provided with the scanner with the smallest FOV, the Accuitomo 3D, for evaluating image quality of all scanners in this study. This ensures that the phantom fits in all the scanners. The first phantom, a contrast phantom, is made of polymethylmethacrylate (PMMA) with an insert of four smaller cylinders with a diameter of 10 mm consisting of aluminium, PMMA, air and bone equivalent plastic (Figures 5.1 (a, b)). Based on the image intensities of each cylindrical structure, the CNR was calculated and an optimal threshold value for segmentation of each structure was obtained. This segmentation allows for image-based measurement of the diameter of the cylinders at various positions, which was used as a measure of image quality as described below.

The second phantom consists of a PMMA cylinder with an insert of folded, 1 mm thick aluminium plates in the form of a mushroom (Figures 5.1 (c-d)). This phantom allows investigation of the sensitivity of a scanner to metal artefacts by image-based measurement of the thickness of the aluminium plates. The different structures in this

phantom are subdivided in three substructures: the straight part of the stem, the round part of the stem and the cap of the mushroom (Figure 5.2). The usefulness of this subdivision is illustrated in Figure 5.3. Figure 5.3 (a) and 5.3 (c) are a computer model of the mushroom phantom and Figure 5.3 (b) and Figure 5.3 (d) are the corresponding images which are acquired from the Accuitomo 3D (Figure 5.3 (b)) and the Sensation 16 (Figure 5.3 (d)). An artefact that occurs is beam hardening (Figure 5.3 (b)). Due to this artefact the intensity of a structure is calculated higher by the reconstruction algorithm. Also streak artefacts can occur (Figure 5.3(d)). Because the structures of a tooth have similar attenuation properties as aluminium, aluminium is used in phantoms for evaluation of image quality of teeth (Herkströter *et al* 1990).

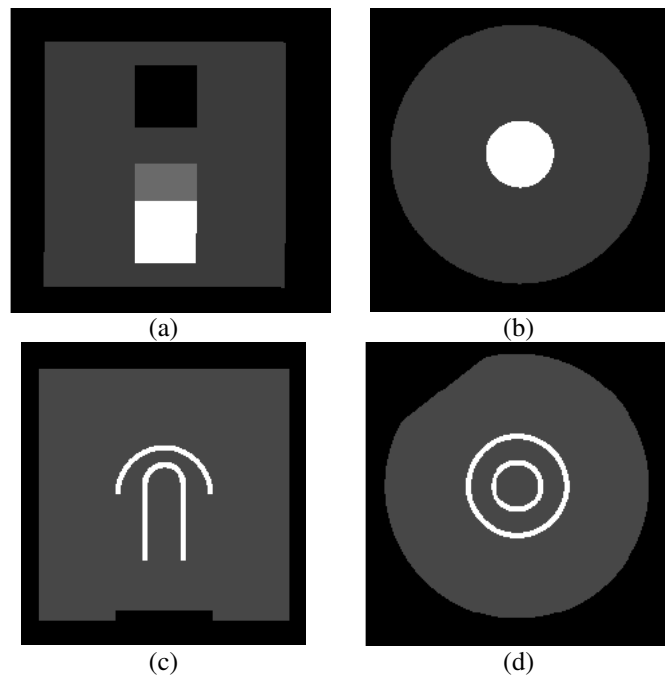


Figure 5.1 Computer-generated 3-D model images of the two phantoms used for evaluating image quality: sagittal slices (a, c) and axial slices (b, d) of the contrast phantom (a, b) and of the mushroom phantom (c, d). The contrast phantom contains cylindrical objects in different materials (air, bone, aluminium).

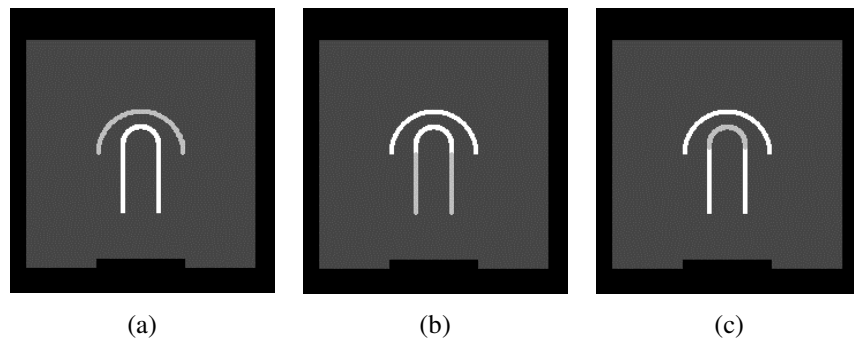


Figure 5.2. The mushroom phantom consists of thin aluminium plates and is divided into separate geometrical parts: the cap (a), the straight part of the stem (b) and the round part of the stem (c).

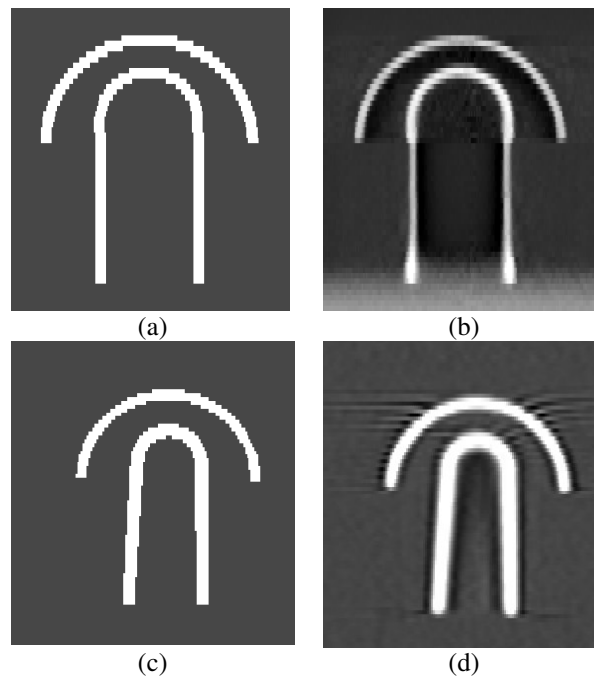


Figure 5.3 Two couples of corresponding coronal slices of the mushroom phantom. Figure (a) and (c) represent a computer model of the phantom and Figure (b) and (d) represent the corresponding axial slice which is acquired with the Accutomo 3D (b) and the Sensation 16 (d).

5.3.3.2 Image quality measurements

a Generation of a 3-D model of the phantoms

Based on technical drawings of the phantom as provided by the manufacturer, a 3-D computer model of each phantom was constructed. This model was described by a set of analytical equations representing the different parts of the phantom, such that no truncation artefacts occur when calculations are performed on the model. For visualization purposes, a high resolution 3-D image of the model was generated by sampling the model on a 3-D image grid, assigning a different grey value or label to each substructure (Figure 5.1).

b Registration

The 3-D image generated from the computer model of the phantom was registered to each of the CBCT and MSCT images using an automated procedure based on maximization of mutual information (MMI) (Maes *et al* 1997). The registration computes a 6-parameter rigid transformation T (i.e. a combination of a 3-D translation and a 3-D rotation) that maps every location in the CT image onto the corresponding location in the model image. The registration was initialised by manually indicating a single landmark in both the model and the CT image, which defines initial values for the translation parameters.

c Feature definition and extraction

Cylindrical regions of interest, each corresponding to a different material in the phantom, were defined on the computer model of the phantom (Figures 5.4 (a, b)), as well as one-dimensional (1-D) measure lines at the boundary of each structure and orthogonal to the surface (Figures 5.4 (c, d)). These regions and measure lines were projected into the CT image using the registration transformation T , such that image measurements can be performed at these geometrically predefined sites in the CT image to assess image quality of the various evaluated scanners and scan protocols, as explained in the next sections d and e.

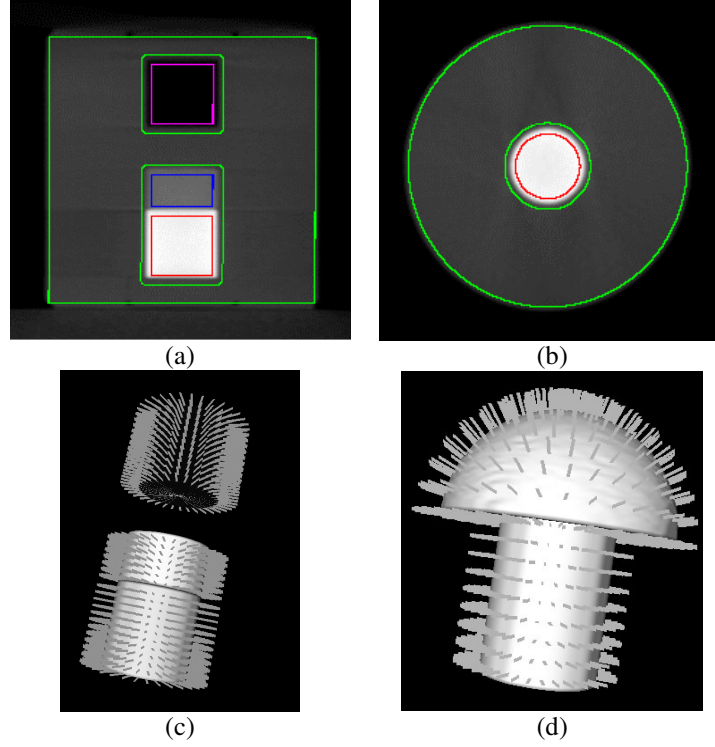


Figure 5.4 Computer-generated 3-D model images of the phantoms used for evaluating image quality, with cylindrical regions of interest (a) and measure lines (b-d) overlaid: (a-c) contrast phantom, (d) mushroom phantom.

d CNR measurements

The cylindrical regions of interest defined in the contrast phantom, corresponding to the various materials, are mapped to the CT image and subsequently slightly eroded to eliminate possible registration errors and to exclude transition artefacts between different materials. The CNR of each object Obj is calculated from the mean and the standard deviation (STD) of the CT intensities within the various regions:

$$CNR_{Obj} = \frac{|mean(I_{PMMA}) - mean(I_{Obj})|}{std(I_{Obj})} \quad (5.3)$$

where I_{PMMA} refers to the CT intensities of the PMMA substrate of the phantom and I_{Obj} to the intensities of the object under investigation, i.e. air, bone or aluminium. The

threshold value T_{Obj} that discriminates between PMMA and the different other materials is calculated as:

$$T_{Obj} = \frac{mean(I_{PMMA}) + mean(I_{Obj})}{2} \quad (5.4)$$

e Thickness measurements

The CT intensities along each 1-D measure line were extracted from the CT image using trilinear interpolation. These 1-D profiles were segmented by using the threshold value T_{Obj} calculated with (5.4). From these segmented profiles the diameter of the cylindrical inserts in the contrast phantom and the thickness of the aluminium plates in the mushroom phantom were measured (Figures 5.5 and 5.6). The differences between the ground truth values as defined in the computer model of the phantom and those measured at the corresponding sites in the CT image were collected for all measure lines, positive values indicating an underestimation of the true thickness, negative values indicating an overestimation. Overall, for the contrast phantom 234, 252 and 432 measurements were collected for the air, bone and aluminium cylinders respectively, and for the mushroom phantom 323, 595 and 595 measurements for the straight part of the stem, the round part of the stem and the cap of the mushroom respectively. The 95-percentile of the absolute value of these thickness errors was used as a quantitative measure of image quality for each object separately.

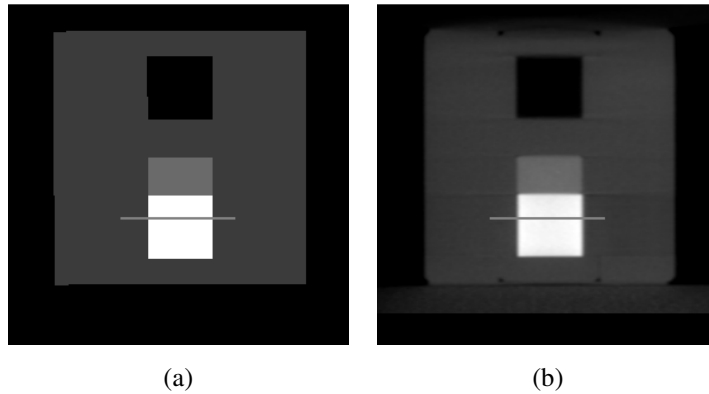


Figure 5.5 Linear measurements used for image quality assessment. Measure lines are defined on the computer model of the phantom (a) and transferred to the CT image (b), after proper registration between them.

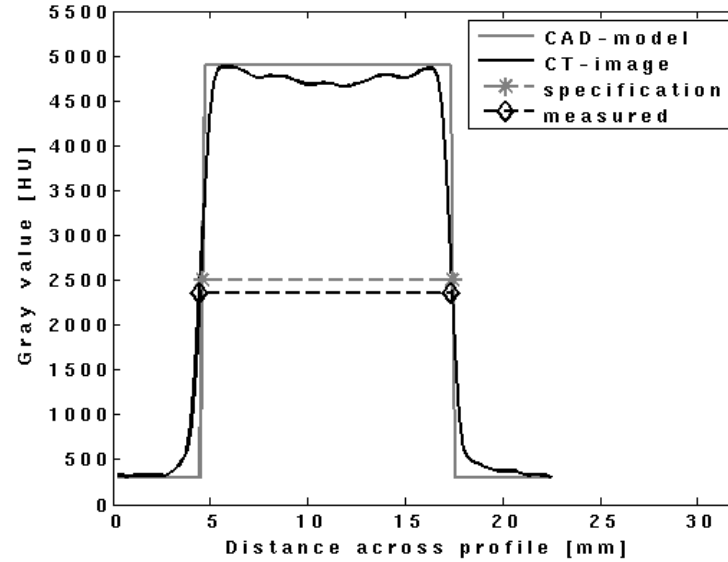


Figure 5.6 The 1-D CT intensity profile along each line is extracted by interpolation and segmented by a threshold in order to measure the thickness of the structure of interest. This image-based thickness measurement is compared to the ground truth of the computer model in order to assess CT image quality.

5.3.4 Experiments

5.3.4.1 Evaluated MSCT and CBCT imaging protocols

The aim of this study was to compare different scanning protocols on CBCT and MSCT with respect to radiation dose and image quality. We indicate the different protocols evaluated in this study by S_{ij} , I_{ij} , N_{ij} , M_{ij} and A_{ij} for the Somatom Sensation 16, i-CAT, NewTom, MercuRay and Accuitomo 3D respectively, where i denotes the set of acquisition parameters and j the reconstruction parameters. The acquisition parameters relevant for MSCT (S_{ij}) are listed in Table 5.2 and those for CBCT (I_{ij} , N_{ij} , M_{ij} and A_{ij}) in Table 5.3. The reconstruction parameters for CBCT and MSCT are listed in Table 5.4. Because of practical reasons, such as the fact that the scanners were located at different institutes and that the available scanning time was limited, it was not possible to perform all effective radiation dose measurements, technical measurements of radiation dose and image quality measurements for all imaging protocols on all scanners.

Table 5.2. Summary of the acquisition parameters of the Somatom Sensation 16 MSCT scanner.

	Tube voltage (kVp)	Tube current x Time (mAs)	Height (mm)	Table feed (mm/rot)	Pitch	Collimation (mm)	Rotation Time (s)
<i>S1j</i>	120	90	225	6	0.5	0.75	0.75
<i>S2j</i>	120	90	63	6	0.5	0.75	0.75
<i>S3j</i>	80	28	225	12	1	0.75	0.75
¹ <i>S4j</i>	80	28	63	12	1	0.75	0.75

¹Only used for the technical evaluation of the radiation dose based on CTDI, not for evaluation of the effective dose.

For the MSCT scanner, protocol *S2j* is typically used for oral implant planning, *S1j* for maxillofacial surgery and *S3j* is the low dose protocol as derived in Loubele *et al* (2006). The FOV of *S2j* was the mandible, while for *S1j* and *S3j* the entire head was scanned in order to obtain an estimate of the upper limit of the patient dose when a complete head scan is performed. Image quality was evaluated for the clinical and low dose protocols, with the images reconstructed with either a smooth reconstruction kernel (H30s, for protocol *Si1*) or a sharp reconstruction kernel (H60s, for protocols *Si2*, *Si3*, and *Si4*). To investigate the influence of the voxel size on the image quality, images reconstructed with different voxel sizes were considered (*Si2*, *Si3*, *Si4*).

Table 5.3 Summary of the acquisition parameters of the CBCT scanners.

	Tube voltage (kVp)	Tube current x time (mAs)	Diameter (mm)	Height (mm)	Shape FOV	Rotation Time (s)	Exposure Time (s)
<i>I1j</i>	120	10.56	160	60	Cylinder	10	1.92
<i>I2j</i>	120	20.2	160	60	Cylinder	20	3.67
<i>I3j</i>	120	39.53	160	60	Cylinder	40	7.19
<i>I4j</i>	120	20.2	160	80	Cylinder	20	3.67
<i>I5j</i>	120	10.56	160	130	Cylinder	10	1.92
<i>I6j</i>	120	20.2	160	130	Cylinder	20	3.67
<i>I7j</i>	120	39.53	160	130	Cylinder	40	7.19
<i>N1j</i>	110	9.1	15.24	100	Sphere	36	5.4
<i>N2j</i>	110	39.6	22.86	150	Sphere	36	5.4
<i>N3j</i>	110	9	30.48	200	Sphere	36	5.4
<i>M1j</i>	120	150	193	193	Sphere	10	10
<i>A1j</i>	60	72	40	30	Cylinder	18.5	18.5
<i>A2j</i>	70	72	40	30	Cylinder	18.5	18.5
<i>A3j</i>	80	72	30	30	Cylinder	18.5	18.5

For the effective dose measurements with the i-CAT scanner, the FOV was positioned according to the recommendations of the manufacturer, i.e. the horizontal laser alignment light placed in the occlusal plane between the lips of the Rando Alderson phantom and the vertical laser alignment light placed 4 cm before the condyle when the chin of the phantom is in the chin support of the scanner. Correct positioning was verified with a single scout view. Based on this positioning the largest scan height was selected (13 cm) to include as much as possible of the entire head. The effective dose was then measured for two different scan times, namely 10 seconds (*I5j*) and 40 seconds (*I7j*). Also the mandible was scanned with the protocol suited for imaging the jaws (*I2j*, *I3j* and *I4j*). For the NewTom 3G, protocol *NIj* is recommended by the manufacturer for oral implant placement imaging, *N2j* for tempomandibular joint indications, and *N3j* for orthodontic indications. These have a spherical FOV with a diameter of respectively 10 cm, 15 cm and 20 cm. For the effective dose measurements, the axial mid plane of the spherical FOV was aligned with the occlusal plane of the Rando Alderson phantom. Positioning along the other directions was performed such as to include as much as possible of the skull and the facial soft tissues in the FOV, including the nose. For evaluation of image quality, protocol *NIj* with a FOV with a diameter of 10 cm was used and the image was reconstructed with the three different reconstruction filters available on this scanner. Some special attention is needed when relating the dose and image quality measurements on the NewTom 3G because of the AEC feature of this scanner. The settings for the mAs are not specified by the user, but automatically determined by the scanner based on the selected FOV and two scout views of the object being imaged. Hence, it is not possible to achieve the same mAs setting for all different experiments. The actual mAs values for our various experiments with the NewTom 3G are listed in Table 5.5. Because the radiation dose is proportional to the mAs, all dose values are recalculated to match the mAs settings used for image quality assessment (i.e. 15 mAs) in order to obtain comparable results. When evaluating effective radiation dose, each exposure also includes the two scout views, as the acquisition of the scout view could not be turned off in this scanner. For the Accuitomo 3D, three different regions of the mandible were evaluated for the assessment of the radiation dose. These regions were: the region with the incisor, the region with the premolar and the region with the molar teeth. The same protocols used for dose measurements were also used for image quality assessment. Only a single reconstruction kernel is

possible with this scanner. Finally, for the MercuRay, the protocol with the largest FOV was selected, both for technical dose evaluation as for image quality measurements. No effective dose measurements were performed for this scanner, as no Rando Alderson phantom was available on site. Some example images acquired of the Rando Alderson phantom with the different scanners evaluated in this study are shown in Figure 5.7.

Table 5.4. Summary of the reconstruction parameters on the different scanners.

Scanner	Code	Voxelsize (mm)	reconstruction filter
Somatom Sensation 16	<i>Si1</i>	[0.141 0.141 0.4]	H30s
	<i>Si2</i>	[0.141 0.141 0.4]	H60s
	<i>Si3</i>	[0.199 0.199 0.4]	H60s
	<i>Si4</i>	[0.398 0.398 0.4]	H60s
i-CAT	<i>Ii1</i>	[0.2 0.2 0.2]	Not applicable
	<i>Ii2</i>	[0.25 0.25 0.25]	Not applicable
	<i>Ii3</i>	[0.3 0.3 0.3]	Not applicable
	<i>Ii4</i>	[0.4 0.4 0.4]	Not applicable
NewTom 3G	<i>Ni1</i>	[0.36 0.36 0.4]	very high resolution
	<i>Ni2</i>	[0.36 0.36 0.4]	high resolution
	<i>Ni3</i>	[0.36 0.36 0.5]	standard resolution
MercuRay	<i>Mi1</i>	[0.377 0.377 0.377]	Not applicable
Accuitomo 3D	<i>Ai1</i>	[0.125 0.125 0.5]	Not applicable

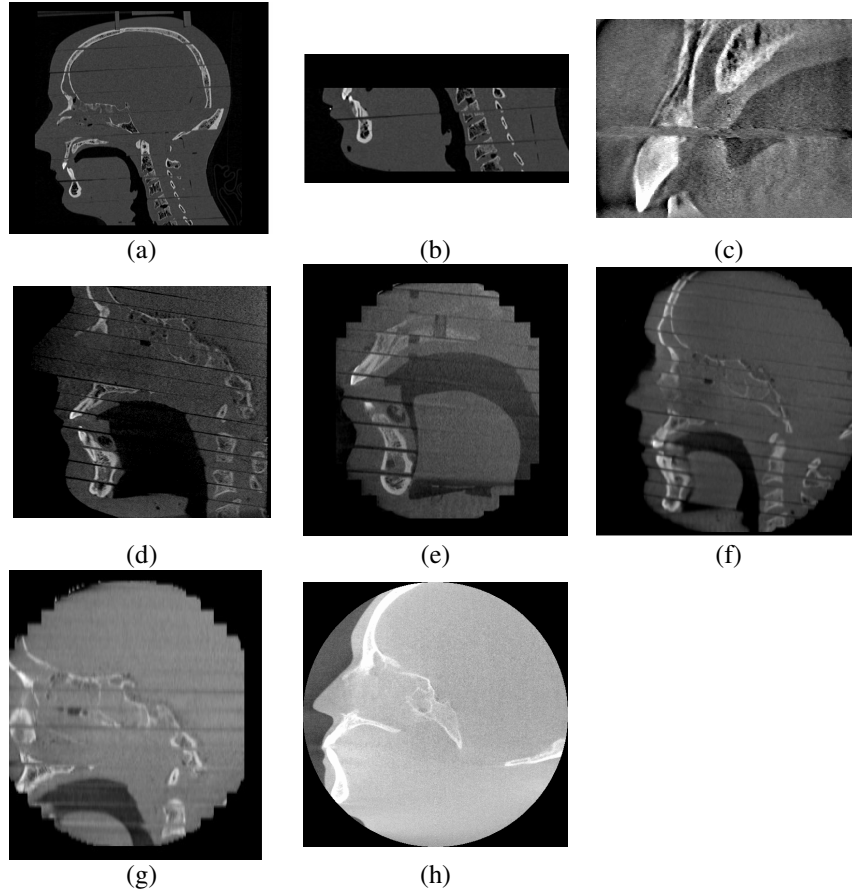


Figure 5.7 Sagittal slices of the CT datasets acquired with some of the protocols evaluated in this study using the Rando Alderson phantom 1 (a-c), the Rando Alderson phantom 2 (d-g) and a skull phantom (h). Protocols shown are: (a) *S14* and (b) *S24* (Somatom Sensation 16); (c) *A31* (Accuitomo 3D); (d) *I34* (i-CAT); (e) *N12*, (f) *N22* and (g) *N32* (NewTom 3G); (h) *M11* (MercuryRay CB).

5.3.5 Relating image quality and radiation dose

To relate image quality and radiation dose, the effective radiation dose was used as a measure for the radiation dose. As explained before, this measure was not available for all the protocols. As explained above, image quality is characterized by the 95-percentile of the absolute value of the difference in thickness of the structures of interest as measured in the CT image compared to the ground truth derived from the computer model of the phantom. This image quality measure is evaluated separately for the cylindrical air,

bone and aluminium inserts in the contrast phantom and for the cap of the mushroom, the straight part of the stem and the round part of the stem in the mushroom phantom. Hence, 6 scatter plots are obtained that relate radiation dose to image quality for these 6 different structures for all evaluated imaging protocols.

Table 5.5 Overview of the mAs parameters resulting from the AEC on the NewTom 3G.

Experiment	Protocol Name	Height [mm]	mAs
Effective radiation dose	N1j	100	9.1
Effective radiation dose	N2j	150	39.6
Effective radiation dose	N3j	200	9
Image quality	N1j	100	15

5.4 Results

5.4.1 Radiation dose assessment

The results of the dose measurements are summarized in Table 5.6. The highest radiation dose was measured for the two head protocols *S1j* and *S2j* on the MSCT scanner. The low-dose MSCT protocol *S3j* achieves similar or even lower dose than some of the CBCT protocols. The Accuitomo 3D has the lowest radiation dose of all evaluated CBCT scanners, but also the smallest FOV.

5.4.2 Image quality assessment

Figure 5.8 summarizes the results of the image quality measurements in the contrast phantom. The mean intensity of air, PMMA, bone and aluminium expressed in Hounsfield units (HU) (Figure 5.8) differs significantly between the MSCT scanner and the various CBCT scanners. This may be due to differences in the spectrum of the X-ray tubes in the various scanners tested and also due to the scattered radiation. The results of the CNR measurements are presented in Figure 5.9. Because the clinical protocol *A3I* did not give an image of the contrast phantom which was suitable for image analysis, this protocol is left out in the analysis of the contrast phantom.

Table 5.6 Results of the effective dose measurements for the various protocols evaluated in this study. Absorbed dose (in mGy) as measured in the Rando-Alderson phantom in various organs and effective dose (in mSv).

	Absorbed dose (mGy)							Effective Dose (mSv)
	Rbm	Thyroid	Bone surface	Brain	Salivary glands	Eye	Mouth	
W_T	0,12	0,04	0,01	0,01	0,01	-	-	
S1j	2.96	6.74	2.83	13.11	14.31	18.98	18.18	0.93
S2j	0.84	5.32	0.74	0.84	9.37	0.65	16.55	0.42
S3j	0.30	1.23	0.29	1.39	1.69	2.45	2.16	0.12
I2j	0.14	0.16	0.14	0.02	0.98	0.54	2.01	0,03
I3j	0.27	0.29	0.27	0.26	1.54	1.99	3.2	0,06
I4j	0.09	0.24	0.09	0.76	0.87	1.11	1.35	0,04
I5j	0.10	0.25	0.10	0.48	1.13	1.16	1.21	0.04
I7j	0.34	0.50	0.34	1.66	4.16	3.85	4.28	0.12
N1j	0.71	0.19	0.71	0.23	2.23	0.35	2.24	0.12
N2j	0.52	0.25	3.10	4.43	3.07	4.43	4.02	0.18
N3j	0.16	0.23	0.16	0.84	1.31	1.54	1.54	0.05
A3j ¹	0.06	0.05	0.06	0.02	0.27	0.51	8.88	0,01
A3j ²	0.10	0.17	0.04	0.30	0.28	0.51	6.04	0,03
A3j ³	0.16	0.07	0.16	0.03	0.59	0.02	2.52	0,03
A3j ⁴	0,58	0,53	0,46	0,68	2,01	1,57	26	0,12

Results of dose measurements for the incisors' region¹, the premolar region², the molar region³ and the complete mandible⁴.

The CNR was the highest with the NewTom 3G in air and the protocols *I2-6-4,4* and *I3-7,4* of the i-CAT (see Table 5.3 and 5.4 for the explanation of these abbreviations). The high CNR for air in the NewTom 3G is an artefact caused by the fact that air falls outside the detectable range of the NewTom 3G, such that all image values for air are returned as -1000 HU with a STD of 0. Hence, for the calculation of the CNR, STD for air was arbitrarily set to 1 for these protocols. The high CNR of the i-CAT for protocols *Ii4* for air can be explained by the fact that these protocols have a high level of built in smoothing because of the large voxel sizes used for reconstruction. The low levels of the CNR of the Accuitomo 3D can be explained by saturation of the 8-bit detector and by beam hardening and cupping artefacts that have a negative influence on the contrast (Mozzo *et al* 1998).

With the threshold values calculated with formula (5.4), the diameter of the cylindrical inserts in the contrast phantom was measured and the error with respect to the known ground truth was computed. The results of these measurements are shown in Figures 5.10 till 5.12 for the three materials. For protocol *A3I*, the image quality of the Ac-

cuitemo 3D was not sufficiently satisfying to obtain a proper segmentation, hence these measurements are left out of the analysis. All evaluated scanners allow quantification of bone with sub-millimetre accuracy (Figure 5.11). Finally, the segmentation of the aluminium cylinder is problematic for the Accuitomo 3D and the *S11* and *S12* protocols of the Somatom Sensation 16 (Figure 5.12). The poor segmentation in the Accuitomo 3D can be explained by beam hardening. The problems with protocols *S11* and *S21* are due to a combination of metal artefacts and the image smoothing induced by the use of the smooth reconstruction kernel H30s, which makes these protocols not appropriate for aluminium segmentation.

The same threshold value as applied for the segmentation of the aluminium cylinder in the contrast phantom was used for the segmentation of the aluminium plates in the mushroom phantom. The results of these accuracy measurements are shown in Figures 5.13 till 5.15. Based on these results, one can conclude that all the CBCT scanners in this study allow quantifying the thickness of the aluminium plates with sub-millimetre accuracy. Most MSCT protocols perform poorly because their image quality suffers from streak artefacts.

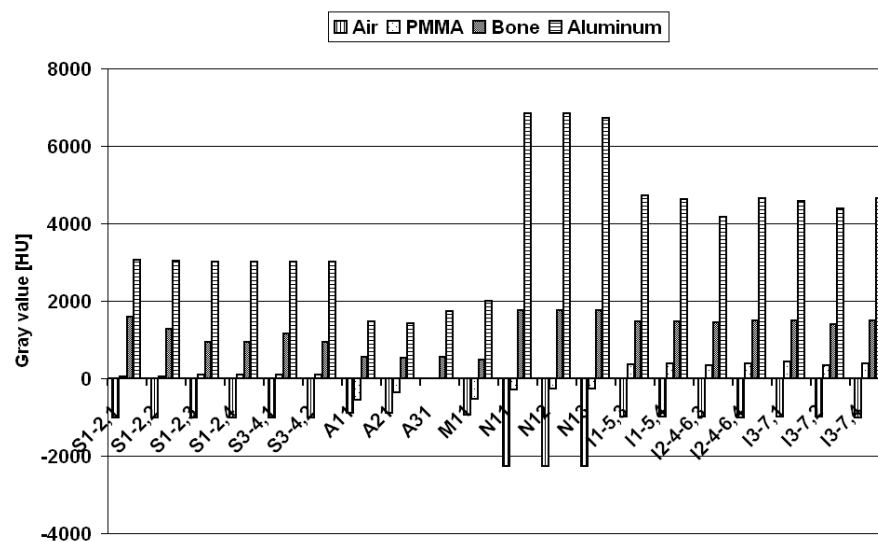


Figure 5.8 Results of the mean intensity of the different materials in the contrast phantom for the protocols as given in Table 5.2 to Table 5.4.

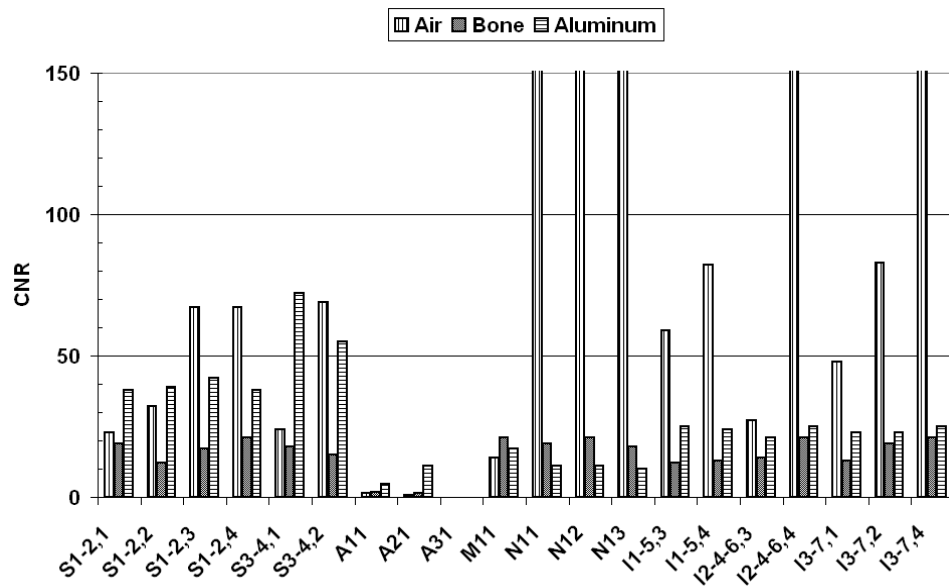


Figure 5.9 Results of evaluation of CNR towards PMMA for the materials in the contrast phantom for the protocols as given in Tables 5.2 to 5.4.

5.4.3 Relating image quality and radiation dose

Figures 5.16 till 5.21 relate image quality to radiation dose for each of the evaluated protocols by plotting the segmentation error against the effective radiation dose for each material of the contrast phantom (Figures 5.16 till 5.18) and each subpart of the mushroom phantom (Figures 5.18 till 5.21) separately. The low-dose MSCT protocols *S3-4,1-2* combine low radiation dose with accurate segmentation of air, bone and aluminium. A similar performance is obtained with i-CAT (all protocols, except for the reconstructions *Si4* at lowest resolution) and NewTom 3G (*N1j*). Figures 5.19 to 5.21 indicate that both CBCT scanners, as well as the Accuitomo 3D, allow for a more accurate quantification of high contrast structures, which is important in dentomaxillofacial imaging for diagnosing dense objects such as the teeth, dentine and enamel.

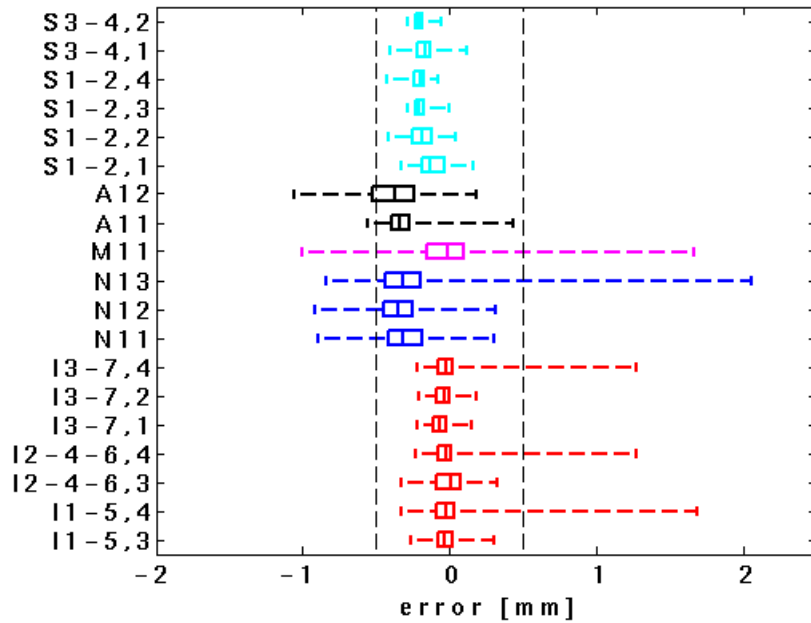


Figure 5.10 Results of the accuracy analysis on the air cylinder of the contrast phantom. The boxplot of the difference between the real thickness and the measured thickness is shown. (Explanation of the protocols Tables 5.2 to 5.4)

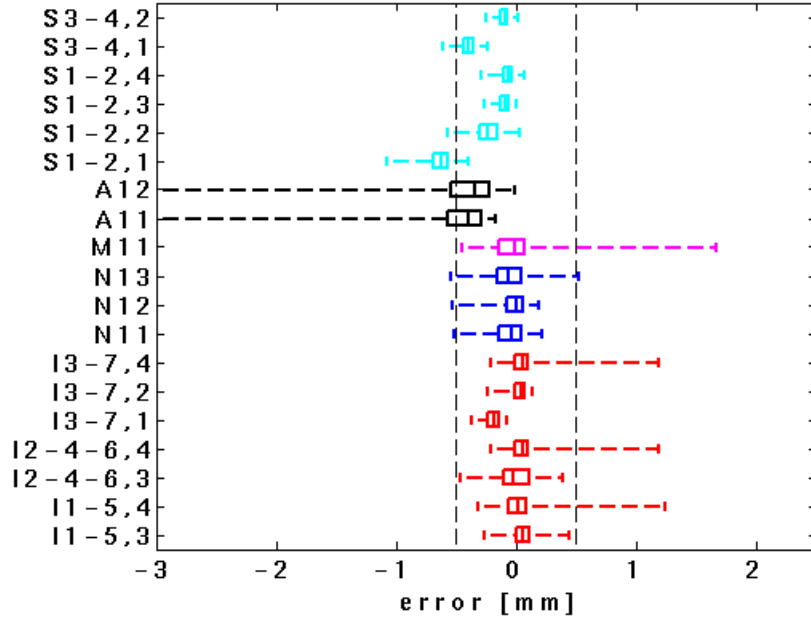


Figure 5.11 Results of the accuracy analysis on the bone cylinder of the contrast phantom. The boxplot of the difference between the real thickness and the measured thickness is shown. (Explanation of the protocols Tables 5.2 to 5.4)

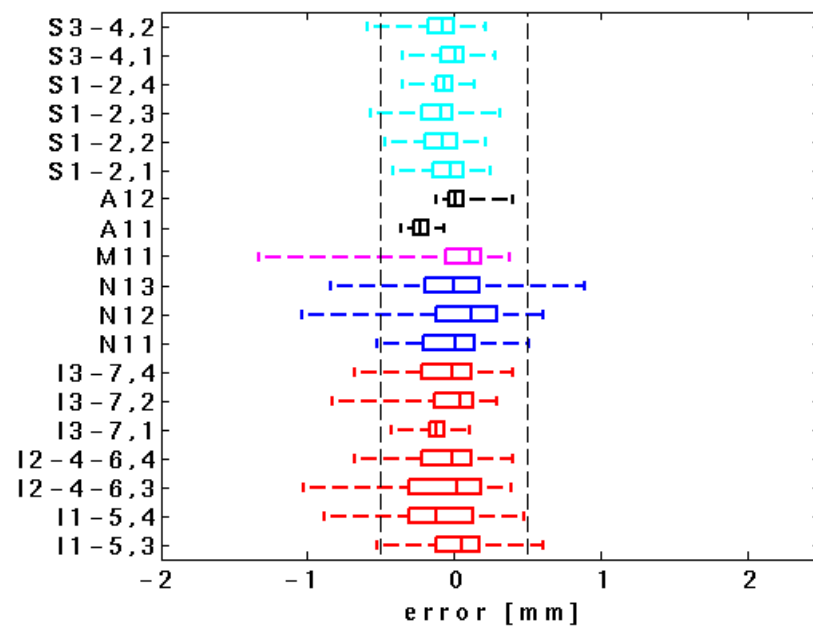


Figure 5.12 Results of the accuracy analysis of the aluminium cylinder in the contrast phantom. The boxplot of the difference between the real thickness and the measured thickness is shown. (Explanation of the protocols Tables 5.2 to 5.4)

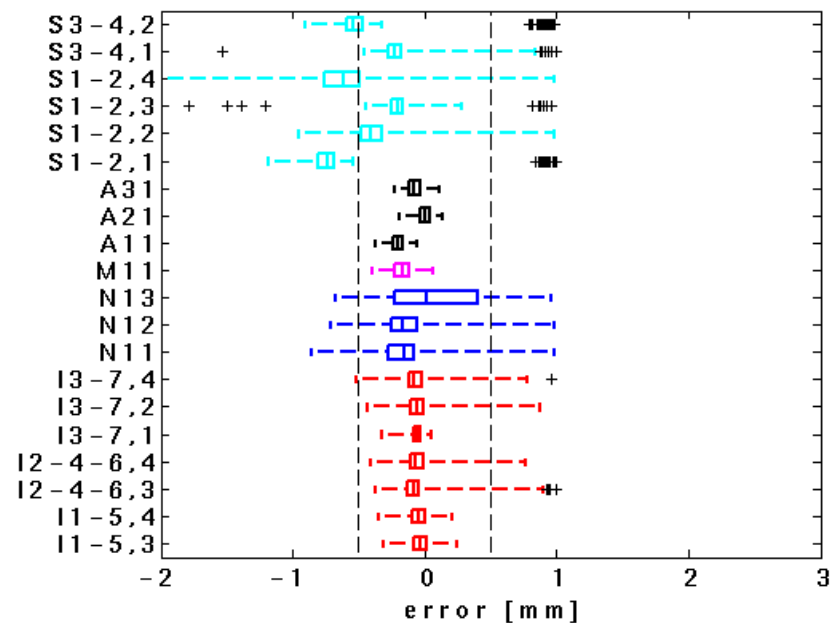


Figure 5.13 Results of the accuracy analysis of the cap of the mushroom. The boxplot of the difference between the measured thickness and the real thickness is shown. (Explanation of the protocols Tables 5.2 to 5.4)

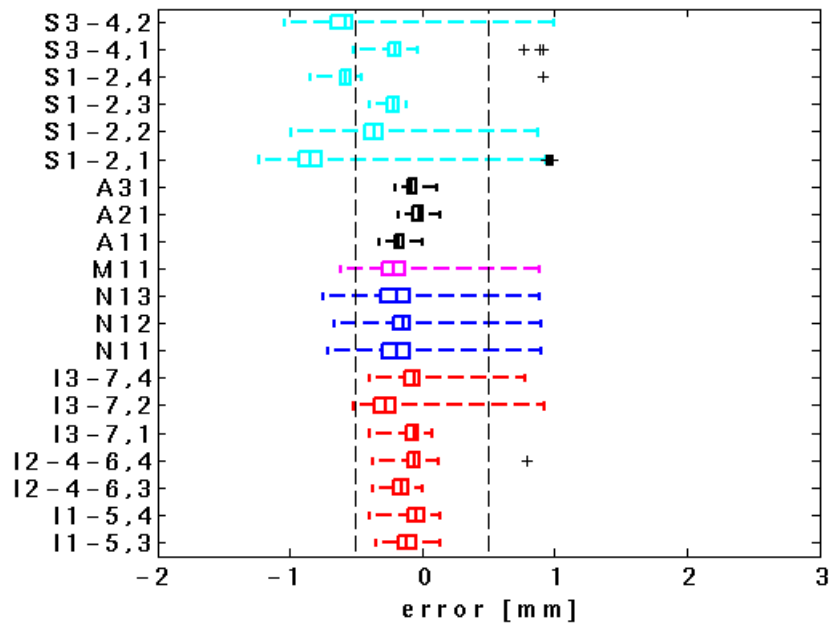


Figure 5.14 Results of the accuracy analysis of the straight part of the stem of the mushroom. The boxplot of the difference between the measured thickness and the real thickness is shown. (Explanation of the protocols Tables 5.2 to 5.4)

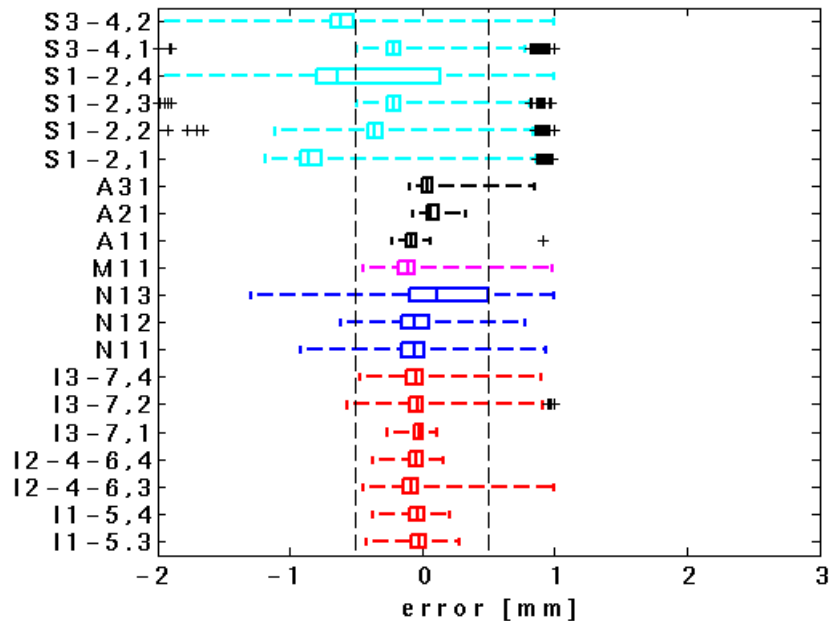


Figure 5.15 Results of the accuracy analysis of the round part of the stem of the mushroom. The boxplot of the difference between the measured thickness and the real thickness is shown. (Explanation of the protocols Tables 5.2 to 5.4)

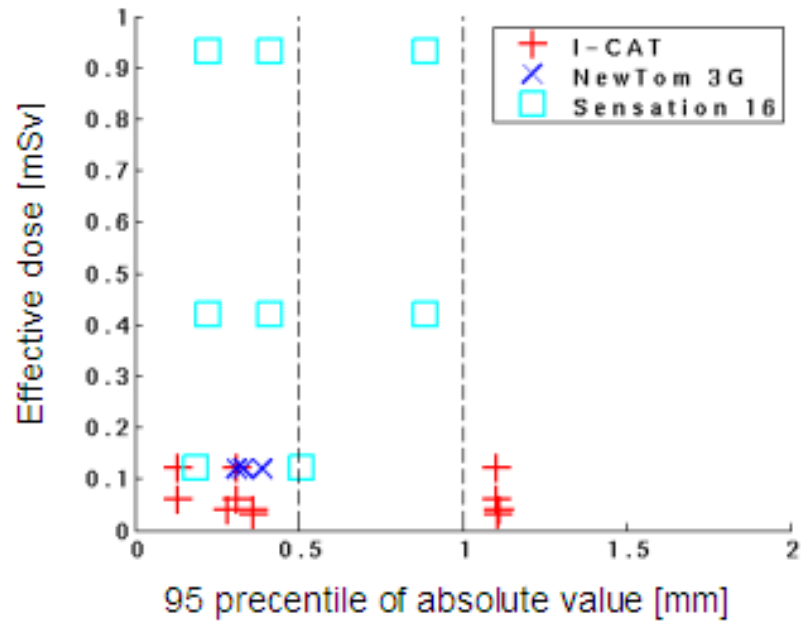


Figure 5.16 Image quality versus radiation dose for the cylinder in air of the contrast phantom. (Explanation of the protocols Tables 5.2 to 5.4)

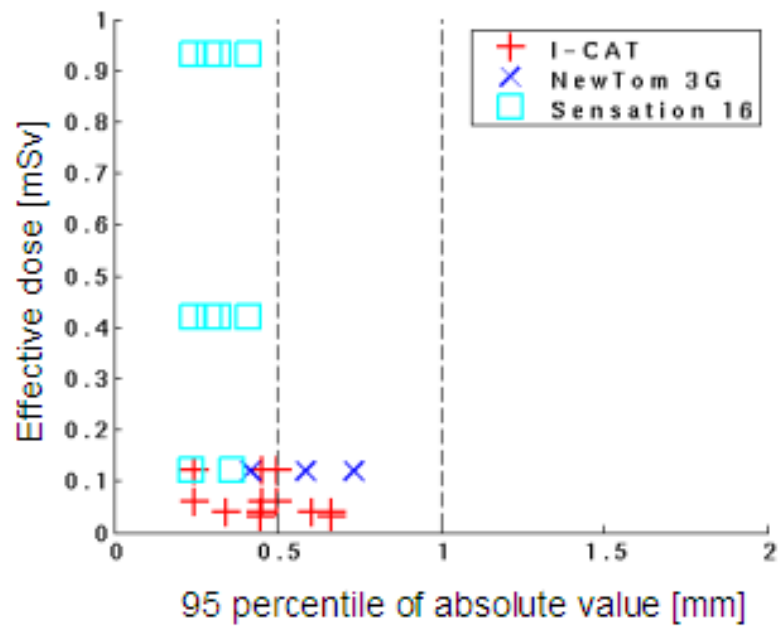


Figure 5.17 Image quality versus radiation dose for the cylinder in bone of the contrast phantom. (Explanation of the protocols Tables 5.2 to 5.4)

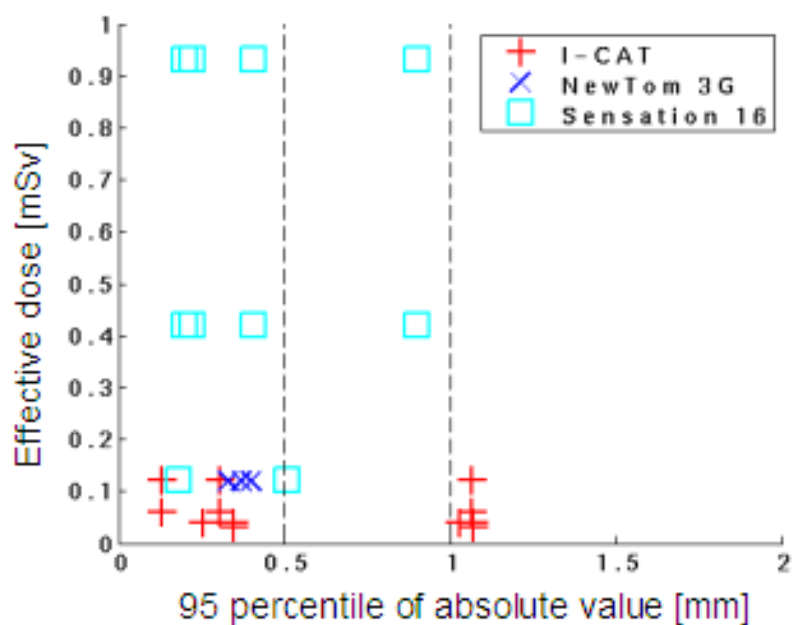


Figure 5.18 Image quality versus radiation dose for the cylinder in aluminium of the contrast phantom. (Explanation of the protocols Tables 5.2 to 5.4)

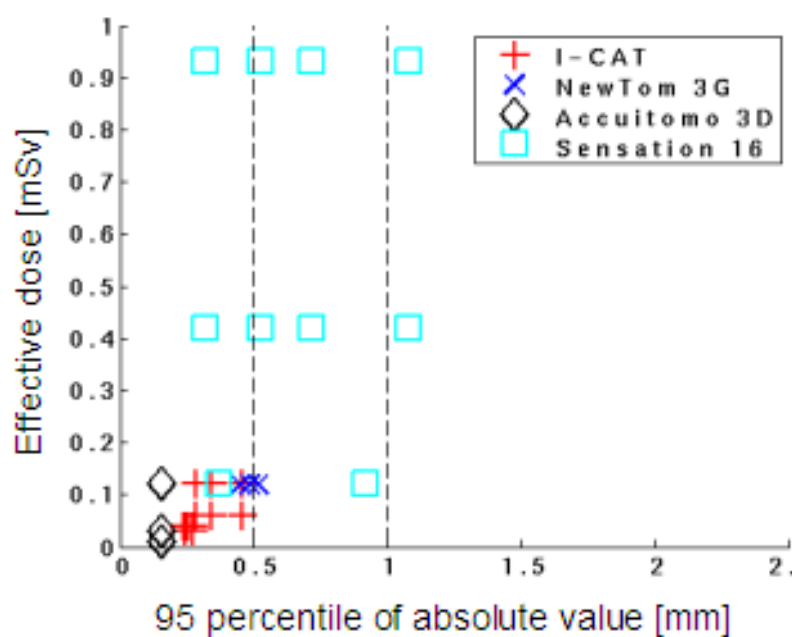


Figure 5.19 Image quality versus radiation dose for the straight part of the stem of the mushroom phantom (Explanation of the protocols Tables 5.2 to 5.4)

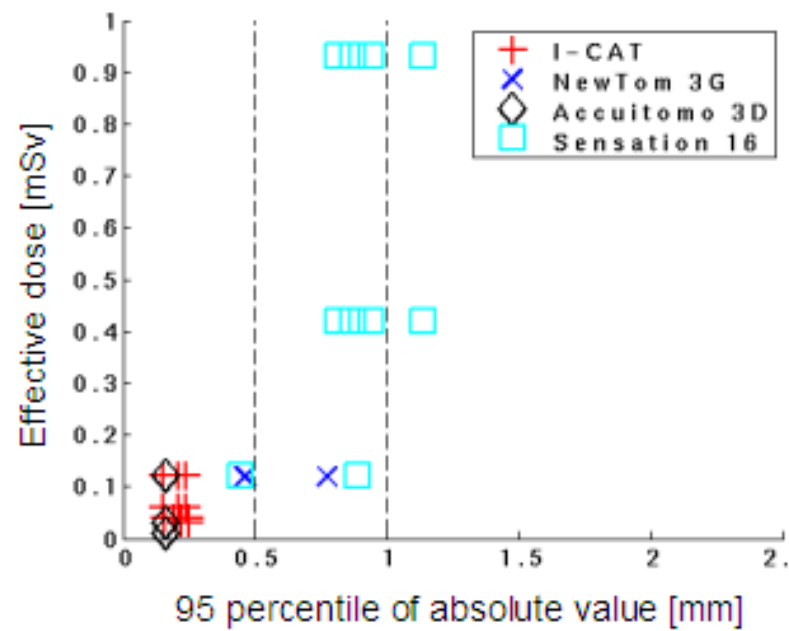


Figure 5.20 Image quality versus radiation dose for the round part of the stem of the mushroom phantom. (Explanation of the protocols Tables 5.2 to 5.4)

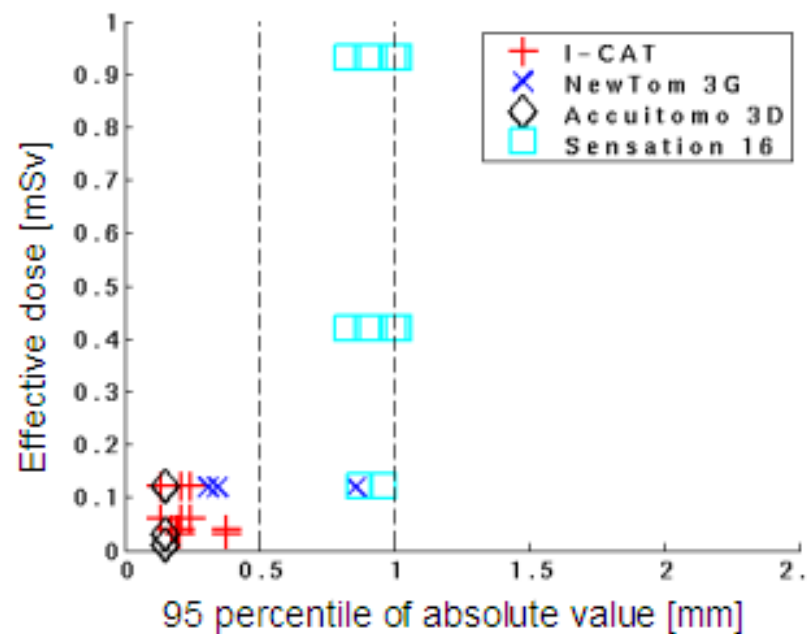


Figure 5.21 Image quality versus radiation dose for the cap of the mushroom phantom. (Explanation of the protocols Tables 5.2 to 5.4)

5.5 Discussion and conclusion

5.5.1 Radiation dose assessment

In this paper, the radiation dose and image quality of different CBCT scanners was compared with the radiation dose and image quality of an MSCT scanner in the context of dentomaxillofacial imaging applications. The radiation dose was evaluated by effective dose measurements in Rando-Alderson phantoms. Measurements of radiation dose in the Rando-Alderson phantom have been performed previously by Ludlow *et al* 2007. They obtained an effective radiation dose according to the ICRP 2007 draft recommendations of 0.059 mSv for protocol *N3j* on NewTom 3G and of 0.193 mSv for protocol *I7j* on i-CAT (Ludlow *et al* 2006). This agrees well with our measurements (0.05 mSv and 0.12 mSv respectively, Table 5.6), with differences likely due to another positioning of the Rando-Alderson phantom, the use of another phantom, other positioning of the TLDs in the phantom, other method of calculation, etc. Although such Rando-Alderson measurements are very time consuming and not practical to achieve when the scanners to be evaluated are positioned at different sites, they facilitate a more fair comparison of the measured radiation dose against published values of other imaging devices.

Based on the results of (Gijbels *et al* 2002, Gijbels *et al* 2004 and Gijbels *et al* 2005) an effective radiation dose of 0.01 mSv appears to be an upper limit for the traditional dental radiography devices, namely the panoramic and the intra-oral devices. Our measurements show that the radiation dose of CBCT scanners is from 2 times (for the Accuitomo 3D) till about 30 times (for the NewTom 3G) higher as that of a traditional dental radiography unit. This, however, is still considerably less than with conventional MSCT imaging.

5.5.2 Image quality assessment

For the assessment of the image quality of the various scanners we used the image quality kit of the Accuitomo 3D, as this phantom could be scanned with all scanners evaluated in this study because of its small size. A disadvantage of this approach would be however that the truncated view artefact could not be visualized, but this was not an issue in this paper. The mean CBCT intensity, expressed in HU, of various materials shows little correspondence to that of the traditional MSCT protocols. This may be due to a combination of lower mean energy of the X-ray beam of the CBCT scanners compared to the

MSCT scanner and the increased level of scattered radiation in CBCT scanners (Carlsson *et al* 1999). This results in a lower contrast for materials like PMMA and a higher contrast for structures with a high density like bone and aluminium (Figure 5.9). This is advantageous for dentomaxillofacial imaging applications where the structures of interest that need to be visualized are also rather dense, such as the dentin and the enamel. For these structures a high resolution is needed in order to facilitate linear measurements with high accuracy as required for diagnosis and treatment planning. The resolution of the various imaging protocols was not measured directly in this study, but can be deduced from the linear measurements. We did not perform comparative resolution measurements using a wire phantom as suggested by one of the developers of the Accuitomo 3D, because from initial pilot studies we concluded that it was very difficult to perform a reproducible measurement using such a phantom.

The accuracy of image-based linear measurements was assessed for quantification of the diameter of the cylindrical inserts in different materials in the contrast phantom and of the thickness of the aluminium plates in the mushroom phantom. For the Accuitomo 3D, it was not possible to properly segment any of the objects in the contrast phantom with protocol A3j (80 kV, 4 mA), which, however, is recommended for patient imaging. This suggests that there is no good correspondence between phantom and in-vivo imaging for this scanner. All protocols on NewTom 3G and Accuitomo 3D had difficulties for segmenting the air cylinder. This is consistent with the fact that in diagnostic imaging there are also difficulties of finding the transition between soft tissue and air with these scanners. This is illustrated in Figure 5.22 for an ex-vivo specimen imaged with the Siemens Sensation 16 (Figure 5.22 (a)) and the Accuitomo 3D (Figure 5.22 (b)). For all the scanners evaluated in this study, there exist imaging protocols that yield segmentation accuracy for the bone simulating material with accuracy better than 0.5 mm. For segmentation of the aluminium cylinder, there are again accuracy concerns for the Accuitomo 3D. However, with the same scanner, a high accuracy is achieved for the segmentation of the thin aluminium plates in the mushroom phantom. Due to the smaller energy of the X-ray beam, the Accuitomo 3D suffers more from beam hardening than the other scanners, which makes it not possible to accurately segment the aluminum cylinder with one global threshold value. Due to this lower energy however, there is a better contrast for the high-density structures like the trabecular bone (Figure 5.22 (b)). This is also

one of the applications for which the Accuitomo 3D is used in the University of Leuven. The other three CBCT scanners achieve accuracy better than 0.5 mm for the segmentation of the small thin aluminum plates in the mushroom phantom. The MSCT scanner, however, suffers from severe metal artifacts (Figure 5.3 (d)), which makes it hardly impossible to segment the aluminum plates accurately.

Based on all these findings, we can conclude that CBCT scanners for dentomaxillofacial radiology applications are indeed designed to accurately image the anatomical structures of interest, especially high-density structures.

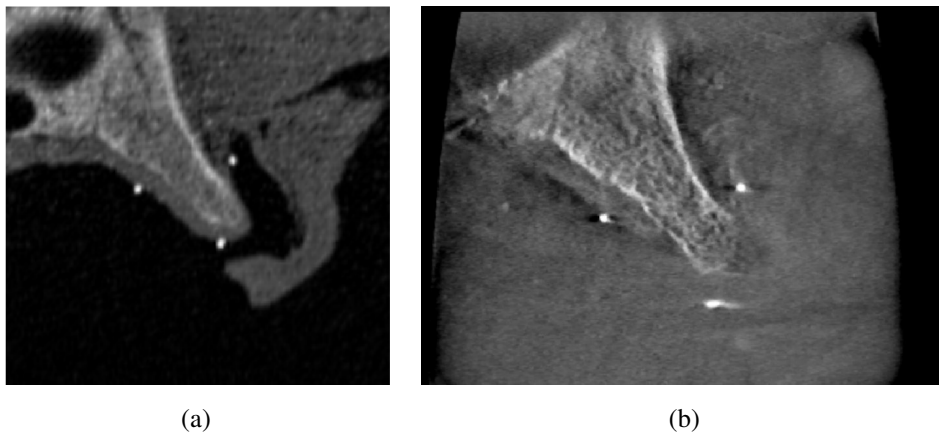


Figure 5.22 The transition of soft-tissue to air can be perceived in the Somatom Sensation 16 MSCT scanner (a), but cannot be discriminated in the Accuitomo 3D (b).

Chapter 6

Discussion

6.1 Technology of CBCT scanners

In this dissertation, a comparison was performed of the available models of CBCT scanners for dentomaxillofacial radiology in the period from autumn 2005 until winter 2006. The aim of this work was to provide a global comparison of the image quality and the radiation dose of different scanners. Difficulties in this comparative study were the lack of standardized protocols for image acquisition on different scanners, which makes it hard to make a complete comparison based on some standardized phantoms. We asked ourselves the question whether this situation would improve in the near future. Therefore we performed a search of the different scanners which are available and looked which information about radiation dose and image quality is present in the literature.

Table 6.1 gives an overview of this search for the current available CBCT scanners for dentomaxillofacial imaging. This overview was made based on the currently available scanners which were presented at the International Dental Show (IDS) at Cologne in April 2007, the 10th European Congress of Dentomaxillofacial Radiology (10th ECDMFR) in Leuven in June 2006 and the 16th International Congress of Dentomaxillofacial Radiology in Beijing (16th ICDMFR) in June 2007.

A comparison of the different design parameters of the scanners taught us that there is still a lack of uniformity in the design of these scanners. We also don't expect this situation to improve with the new generations of scanners. The new models also contain both types of scanners which work at a low kV (for example 40 kV for the Picasso) and scanners which work at a high kV (120 kV for the i-CAT and CB-Throne). For the detection of the X-rays, both the CCD (Galileos) and FPD (i-CAT) are used. All manufacturers also provide at least one scanner which scans the patient in an up-right position. But it is important to note that the characteristics of the different scanners are so distinct that the results of one scanner cannot be extrapolated to another scanner and can certainly not be generalized for the whole family of CBCT scanners dedicated to dentomaxillofacial imaging. This makes it impossible to get an impression of image quality and radiation dose based on the given parameters.

Table 6.1 Overview of international peer reviewed literature available of past and current CBCT models

Company	Model	Radiation dose	Accuracy
Morita	Accuitomo 3D (1)	no	Yes
	Accuitomo 3D (2)	no	No
	Veraviewepocs	no	No
Imaging Sciences International	i-CAT	yes	Yes
Quantitative Radiology	NewTom 9000	yes	Yes
	NewTom 3G	yes	Yes
	NewTom VG	no	No
Asahi Roentgen	3-D Panoramic	no	Yes
	Alphard Vega	no	No
E Woo Technology	1	no	No
	2	no	No
	3	no	No
Vatech	Implagraphy	yes	No
	VCT	yes	No
Planmeca	Promax 3-D	no	No
Kodak's Dental Systems	Iluma	no	No
TeraRecon	Prexion	no	No
Soredex	Scanora 3-D	no	No
Hitachi Medical	3-D MercuRay	yes	No
	CB throne	no	No
Sirona	Galileos	yes	Yes

Therefore, for comparison of radiation dose and image quality one is dependent on the information provided by the manufacturers and published in the peer-reviewed journals. As briefly mentioned in chapter 1 and as will be further discussed in section 6.2 it is not possible to use the CTDI as a technical measure for the comparison of the radiation dose of different scanners any more (Dixon *et al* 2005). Therefore, the fastest way to acquire results of the effective radiation dose of scanners is through experimentation using Rando Alderson Phantoms. However, the measure which is provided in the manuals of the manufacturers is for a modified version of the CTDI and in most cases is only an estimation of the radiation dose based on Rando-Alderson phantoms together with a reference to the study performed.

Next, the manufacturers provide information about the quality control procedures. This is information such as the MTF, the expected HU of some materials and the CNR. Besides these measurements, some patient cases are also presented. But a look at

Table 6.1 shows that there is very little information available about the accuracy of the different scanners in peer reviewed journals. There is definitively a need for a protocol that can objectively evaluate accuracy and radiation dose of the scanners. This should be included in the manual of the different scanners. This is especially true because of the enormous growth of the market of CBCT scanners for dentomaxillofacial applications, which will make it hard to perform similar studies in the future.

6.2 Evaluation of methods for dose measurements

As mentioned before, the effective radiation dose has to be calculated from absorbed dose values, which can be determined either by measurements using a Rando-Alderson phantom or by Monte Carlo simulations. Measurements using Rando-Alderson phantoms are very sensitive to the positioning of the primary beam, the positioning of the TLDs, the phantom that is used and the calculation of the fractions being irradiated. For positioning of the patient in CBCT scanners, care must be given to the positioning in the axial plane (Struelens *et al* 2005). In view of the experimental uncertainties, the use of Monte-Carlo simulations seems to be a good alternative or complementary method, because this will assess dose distributions in the whole scan plane. Nevertheless there is a lot of research still going on to evaluate these methods. As such, these simulations cannot guarantee immediate and correct information about the effective radiation dose when new radiological devices are presented (Struelens *et al* 2005).

Because calculations of the effective radiation dose cannot be applied to every single patient, it is the general practice in radiology to define a dose-related parameter that can easily be measured or calculated from the exposure settings and which can be converted to the effective radiation dose through the use of tabulated conversion factors (Leitz *et al* 1995). Examples of such dose-related parameters are the CTDI, the Dose Length Product for CT scanners and the Dose Area Product for X-rays. A similar parameter for CBCT does not yet exist and the methods available from CT are not immediately applicable to CBCT for various reasons. For the CBCT scanners, in most cases only one rotation around the patient is performed. Some dose quantities defined for CT (e.g. the Dose Length Product, Dixon 2006) are therefore not relevant to CBCT. This is however not the only problem: for CBCT scanners the height of the FOV is at least 3 cm and therefore not all the scattered radiation dose can be covered with an ion chamber of 10 cm, which is the standard equipment for the measurement of the CTDI. Much longer

CTDI phantoms (with a length up to 90 cm) are needed (Mori *et al* 2005). This approach is however not feasible for the CBCT scanners in dentomaxillofacial radiology because it is technically not feasible to put a phantom with such a large length in a CBCT scanner.

Because of the large learning curve for the use of Monte Carlo simulations and the problems with the technical dose measures for CBCT, we decided to use effective dose measurements for the evaluation of the radiation dose of the different CBCT scanners.

6.3 Choice for an optimal threshold value

6.3.1 Introduction

A key part of the analysis of the accuracy of linear measurements was the choice of the threshold value for the segmentation of the bony tissues. Several methods were used in this dissertation. We will briefly describe the methods used and will discuss which of the methods should be preferred in which cases.

6.3.2 Calculation of 50% threshold

In chapter 2, a number of measure lines were defined perpendicular to the boundary of the structure to be segmented. Across these measure lines, the 1-D intensity profiles of the CT-image was calculated. Based on these profiles the average profile was calculated and the mean value of the maximum and the minimum of this average profile was used as the threshold value.

In chapter 5, a variant of this method was used. A mask was defined which lies completely in the structure-to-segment and another mask was defined in the material which surrounds the structure-to-segment. The mean intensities of the voxels corresponding to the two masks were calculated. The threshold value was then set as the mean of the two latter means.

This is a very accurate way of calculating a threshold value. But the disadvantage is that it only can be used when a description of the object that is to be segmented is available. This is not the case in the normal clinical situation. However for the evaluation of the upper limit of the accuracy of a scanner or for purpose of quality control, this can be a very useful method.

6.3.3 Analyses of the histogram of intensities

Because the former methods could not be applied in the normal clinical situation, we searched for other heuristics which could be applied. A binary mask was defined by indicating the structure which needs to be segmented in chapter 3. The histogram of the intensities of the voxels in this mask was calculated. This histogram can be approximated by a mixture of two or more Gaussians. The parameters which gave the best approximation of this histogram were calculated based on SEM. Next the Gaussian corresponding with soft tissue and bone are selected manually. From these two Gaussians one can calculate the probability distribution for bone and soft tissue. The threshold value was then calculated as the intensity which had the same probability for being soft-tissue as for being bone.

This method was used in chapter 2 because at that moment there was no ground-truth available for the verification of the segmentation accuracy, but when a better ground-truth was available, this method didn't seem to give satisfactory results.

6.3.4 Analysis of the weighted histogram of the laplacian

A better technique for determining an optimal threshold value was developed by Wiemker and Zwartkruis (2001). At the edges of a structure the gradient of the intensities reaches a maximum value. This means that if we would select a number of threshold values and for each of the threshold values calculate the sum of the gradient of the voxels which correspond to this threshold values, the maximum is reached at the optimal threshold value. These heuristics can be optimally calculated by the histogram of the weighted laplacian of the image intensities. An optimum in this histogram will correspond to an optimal threshold value.

In chapter 5 this method gave very accurate results for the bone segmentation in the i-CAT and the Sensaiton 16. For the other scanners this method performed worse because of the intensity inhomogeneity of those CBCT-images.

6.3.5 Conclusion

Based on our results we come to the following rules for finding an appropriate threshold value:

- If a ground truth exist of the structure to segment, than one of the two 50 % threshold rules can be used.

- In the common clinical situation, the ground truth is not known, in that case one can use the histogram of the weighted laplacian histogram.
- If there are a lot of intensity inhomogeneities in the CBCT image, the rules based on the analysis of the histogram don't perform well and an improvement of the image quality is needed to improve the segmentation accuracy or a more sophisticated segmentation algorithm is needed.

6.4 Evaluation of the different phantoms

6.4.1 Introduction

Although the accuracy of these scanners is very important even though many CBCT scanners are available in the dentomaxillofacial field, few publications are available regarding accuracy assessment of linear measurements about bone structures in CBCT scanners in the dentomaxillofacial field. In this section we focus on the phantoms which were used in the available studies.

Accuracy of linear measurements on dry skulls was performed by Lascala *et al* (2004), Kobayashi *et al* (2004), Pinsky *et al* (2006), Ludlow *et al* (2007) and Mischkowski *et al* (2007). The results of Chapters 4 of this dissertation can be related to these studies. Accuracy analysis based on geometrical phantoms were performed by Marmulla *et al* (2005), Pinsky *et al* (2006) and Mischokowski *et al* (2007). The results of chapter 5 can be related to these studies.

6.4.2 Accuracy on dry skulls

For all the studies in which accuracy measurements on dry skulls were assessed, reference points were indicated on the dry skull through the use of radiopaque markers (Lascala *et al* 2004, Ludlow *et al* 2006) or by drilling holes in the dry skull (Kobayashi *et al* 2004, Pinsky *et al* 2006) or by a combination of both (Mishokowski *et al* 2007). The gold standard was acquired next by measuring distances between the different reference points on the skull using a caliper. After insertion of the skull in a plastic box filled with water to simulate soft-tissue, the skulls were scanned. Next, similar measurements were performed in the CBCT images by a group of observers based on dedicated software provided by the scanner or by third party software. Statistical analysis was then performed based on the differences between the gold standard measurements and the meas-

measurements on the CBCT images. Such observer studies are very time-consuming and dependent on inter and intra-observer variability. Because these measurements are performed on human skulls, which are different from one another and because they were only performed on a limited number of points, it is not possible to talk about a standardized phantom. The studies were only performed to assess the accuracy of one CBCT scanner: Lascala *et al* (2004), NewTom 9000; Kobabyashi *et al* (2004), 3-D Multi Image Micro CT; Pinsky *et al* 2006, i-CAT; Ludlow *et al* 2007, NewTom 9000 and Mishkowsky *et al* 2007 (Galileos). The conclusions of these studies were that the CBCT under investigation allowed for accurate measurements. Unfortunately, because there is no standardized skull phantom available, the results acquired in one study cannot be compared with the results in another study.

If we relate the methodology of chapters 3 and 4 to these studies, one can first see that much more measurements are performed in these chapters than in the above mentioned studies. In these studies no markers were needed because a registration was performed between the data used as a gold standard and CBCT data. The disadvantage of the study in Chapter 3, was that the gold standard here was acquired from MSCT images. In Chapter 4, this problem was solved by using a laser scanner for acquiring the ground truth. A comparison between the accuracy results in these literature studies and these chapters teaches us that with human observer measurements usually higher accuracy can be achieved than with an automated skull segmentation. This can be explained because of the segmentation algorithm which is used. As mentioned in Chapter 3, the segmentation is performed based on one threshold value. Therefore, if there are intensity inhomogeneities in the CBCT image, these might not be noticed by the threshold value and this might give a less accurate segmentation result.

6.4.3 Geometrical phantoms

Through the use of fabricated geometrical phantoms like Marmulla *et al* (2004), Pinsky *et al* (2006), Mishkowsky *et al* (2007), it was possible to acquire reproducible results for all scanners. The phantoms which were fabricated for these studies consisted of a background material which was used to simulate soft-tissues: polymethylmethacrylate (Marmulla *et al* 2004), acryl (Pinsky *et al* 2006) and silicon gel matrix (Mishkowsky *et al* 2007). For the study of Marmulla *et al* (2004) and Pinsky *et al* (2006),

respectively, small cylinders or holes were drilled into the phantom. Because air has a lower density than the background material, in these two cases, segmentation of regions of black intensity needed to be segmented out of a gray background. For the study of Mishowkosky *et al* (2007), polytetrafluorethylene was used for the fabrication of a cube, a pyramid, a cuboid, a hexagon and a cylinder. These structures were inserted in the silicon gel matrix. The polytetrafluorethylene has a higher intensity than the silicon matrix. So in this case, high intensity structures needed to be segmented. If we compare the approach of chapter 5 with these studies, we can see that in our study different materials are segmented out of the polymethylmethacrylate phantom. We provide also more information about the segmentation algorithm that we applied. The results which are acquired in the three studies mentioned above: a mean accuracy of 0.13 mm in (Marmulla *et al* 2005) and a mean accuracy of 0.1 mm in (Pinsky *et al* 2006) are in the same range as the results which are acquired in chapter 5. However, it is important to search in future studies for the correlation between such geometrical phantoms and the clinical situation.

6.4.4 Conclusion

Based on the quest for phantoms in this dissertation, we may conclude that there is need for a standardized phantom for evaluating the image quality of CBCT scanners for the head. Accurate descriptions of these phantoms must be available; these descriptions can be technical drawings or surfaces acquired through laser scanning. Such a phantom can be based on the paper of Chiarot *et al* 2005: their phantom is a Rando phantom with inserts which simulate different lesions and inserts for the evaluation of physical imaging performance. For the evaluation of CBCT scanners different sizes of inserts need to be made because of the different sizes of FOVs that are possible for the distinct scanners. It is also important that these phantoms can be used lying down or standing up in a scanner.

6.4.5 Correlation between different phantoms

In a final study the segmentation accuracy of the bony and aluminium structures in the phantom was compared to the segmentation accuracy of the mandible of the phantom that was designed in chapter 4. For the determination of the threshold values of the bone, the same rule as described in chapter 4 was used. The results of the evaluation of the segmentation result can be found in Table 6.7. The correlation between the accuracy results ac-

quired on the segmentation of the bony cylinder and the aluminium cylinder can be found in Table 6.8. The highest correlation is found between the 95th percentile of the segmentation of the bony cylinder and the 95th percentile of the mandible in the skull phantom. This means that the segmentation of the bony cylinder already gives an indication for the maximum error, but improvements are still needed for a better accuracy estimation based on the segmentation results achieved in the cylinder.

Table 6.7 Results of assessment of segmentation accuracy on different CBCT scanners

Protocol	Threshold	Mean	SD	Prct 95
<i>N11</i>	960	-0,68	1,5	3,44
<i>N21</i>	960	-0,69	1,5	3,51
<i>N31</i>	980	-0,74	1,49	3,49
<i>I13</i>	819	0,03	0,68	1,38
<i>I14</i>	829	-0,03	0,62	0,96
<i>I24</i>	731	-0,08	0,54	0,95
<i>I31</i>	830	-0,01	0,59	1,1
<i>M11</i>	-110	-0,14	1,97	4,24
<i>S25</i>	1000	0,14	0,6	1,23
<i>S26</i>	1000	0,19	0,56	1,22
<i>A31</i>	800	0,46	1,08	2,92
<i>A31</i>	1000	0,46	1,08	2,92

Table 6.8 Results of the calculation of the correlation coefficient between the results of segmentation accuracy in the mandible in the skull phantom on the one hand and the cylinder in bone and aluminium in the contrast phantom on the other hand

Material	Quality measure	Correlation
Bone	Mean	-0,06
	SD	0,36
	Prct 95	0,46
Aluminium	Mean	-0,29
	SD	0,36
	Prct 95	-0,14

6.5 Clinical implications

6.5.1 Radiation dose

6.5.1.1 Introduction

In chapter 5, the radiation dose of different CBCT scans was assessed. It is however not that important to know the influence of one scan to one patient, but it is essential to know the epidemiological effect of the large use of CBCT scanners in dentomaxillofacial applications. The Rando-Alderson phantom typically represents a male or a female person. Unfortunately these phantoms only represent the average male or female which obviously does not exist. Therefore, there is also a need for more personalized dosimetry especially when CBCT scanners are used for scanning of children. The estimation of the global effect is a weighted average of different age groups. The influence of CBCT to the global dose will be dealt with in the following section.

6.5.1.2 Influence of the use of CBCT to global dose

In Chapter 1, we mentioned a study in Switzerland (Aroua *et al* 2004) which showed that 43% of the radiographs which were acquired in Switzerland were derived from dentistry. However, dental radiographs only account for one percent of the effective dose which patients receive yearly from medical exposures (Aroua *et al* 2004). Similar results were found in a study performed in Luxemburg (Shannoun *et al* 2006) and by UNSCEAR 2000 for the period of 1991-1996.

Based on Aroua *et al* 2004, one can conclude that the major contribution from radiation dose in dentistry comes from intra-oral and panoramic radiography. The influence of the radiation dose of dental CT to the dose of dentistry is negligible because of the small number of acquired dental CTs. The use of CBCT in dentistry will lead to an increase in the dose coming from dentistry. To calculate this increase, dose estimates from a CBCT examination, intra-oral radiographs and panoramic radiographs are needed. Also the percentage of intra-oral radiographs and panoramic radiographs is needed. The distribution of intra-oral and panoramic radiographies were derived from UNSCEAR 2000 and are given in Table 6.2.

Due to the introduction of the new weighting factors of ICRP 2007, the dose estimates of intra-oral radiographs and panoramic radiographs need to be recalculated. The

recalculation of the effective radiation dose was performed based on Gijbels *et al* (2002) and Gijbels *et al* (2005). This calculation can be found in Table 6.3. This table also gives a global overview of radiation studies which were performed on CBCT scanners. If intra-oral radiographs are to be replaced by CBCT scanners, preferably a CBCT scanner with a small FOV like the Accuitomo 3D (CBCT1) will be used. If panoramic radiographs will be replaced by CBCT scanners, more likely a protocol on a CBCT scanner which images the mandible, the maxilla or both will be used (CBCT2). Therefore to calculate the radiation dose of CBCT1, the mean value of effective dose of Accuitomo 3D will be used. This value is 23 μSv . To calculate the radiation dose of CBCT2, the mean value of examinations of jaws on the NewTom 9000, NewTom 3G, the Implagraphy and the i-CAT will be used. This value is 78 μSv . If the assumption is made that the same percentage of intra-orals and panoramic radiographs will be replaced by the appropriate CBCT scans, the influence of the use of CBCT scans on the global dose can be estimated. This calculation is performed for the different countries given in Table 6.1 and is presented in Figure 6.1. Because the contribution of the radiation doses in dentistry is 1% of the global dose received from medical radiation, a second interpretation of this graph can be made. This is that the y axis also gives the percentage of radiation dose in dentistry to the global radiation dose if the percentage of CBCT scanners given on the X-axis would be used. Based on Figure 6.1 one can conclude that special care must be taken when using CBCT in dentistry, because its frequent use might give an increased collective dose.

However, for the use of image guided planning of implants, 3-D scans are needed. Because the CBCT scanners provide 3-D scans with a smaller dose than MSCT scanners, the use of CBCT scans make sure that the radiation dose which is due to image guided implant treatment is lowered. To illustrate this, a similar experiment is performed as before. But now the influence of using a percentage of CBCT scans instead of MSCT scans for the acquisition of the jaws is analysed (Figure 6.2). Here the use of CBCT instead of MSCT might result in a decreased collective dose.

Table 6.2 Summary of the number intra-oral and panoramic radiographs per 1000 inhabitants for different countries. (UNSCEAR)

	Number Intra-oral radiographs	Number Panoramic radiographss	Number Total	Distribution Intra-oral radiographs[%]	Distribution Panoramic radiographs[%]
Finland	254	36	290	88	12
Switzerland	524	34	571	92	6
Japan	743	88	839	89	10
Luxembourg	438	31	469	93	7
Netherlands	170	8	182	93	4
Sweden	682	57	739	92	8
UK	161	49	212	76	23

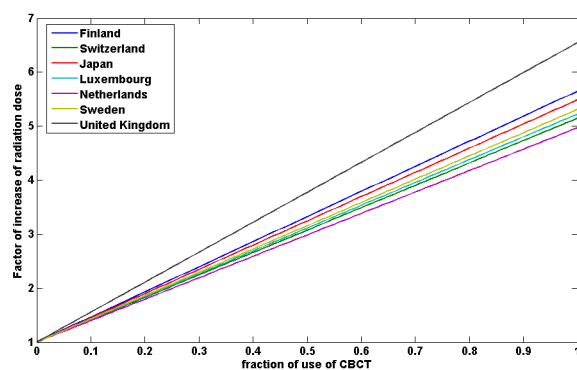


Figure 6.1 Influence of the use of CBCT to the global dose of dentistry

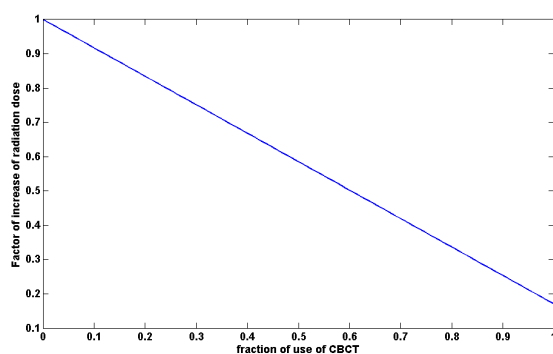


Figure 6.2 Influence of the use of CBCT instead of MSCT in image guided implant treatment.

Table 6.3 Overview of effective radiation dose of dose studies adapted to ICRP 2007.

Scanner	Study	Region	Thyroid	Bone marrow	Oesophagus	Bone Surface	Brain	Salivary Glands	Effective dose [mSv]
NewTom 9000	Tsiklakis <i>et al</i> 2005	No shielding	0.32	0.058	0.16	0.20	0.32	1.20	0.045
	Tsiklakis <i>et al</i> 2005	Shielding	0.18	0.05	0.2	0.20	0.30	1.16	0.04
	Ludlow <i>et al</i> 2003	Max/man	0.370	0.093	-	0.432	0.400	1.682	0.051
	Ludlow <i>et al</i> 2003	Mandible	0.430	0.071	-	0.327	0.195	0.162	0.033
	Ludlow <i>et al</i> 2003	Maxilla	0.200	0.052	-	0.240	0.200	0.887	0.028
NewTom 3G	Ludlow <i>et al</i> 2006	Large FOV	0.333	0.125	0.057	0.581	0.700	0.956	0.054
	Chapter 6	Small FOV	0.19	0.71	-	0.71	0.23	2.23	0.125
	Chapter 6	Medium FOV	0.25	0.52	-	3.10	4.43	3.07	0.178
	Chapter 6	Large FOV	0.23	0.16	-	0.16	0.84	1.31	0.052
i-CAT	Ludlow <i>et al</i> 2006	Large FOV	0.767	0.418	0.123	1.941	3.583	3.522	0.177
	Chapter 6	Mandible	0.16	0.14	-	0.14	0.02	0.98	0.035
	Chapter 6	mandible	0.29	0.27	-	0.27	0.26	1.54	0.065
	Chapter 6	Max/man	0.24	0.09	-	0.09	0.76	0.87	0.038
	Chapter 6	13 height	0.25	0.10	-	0.10	0.48	1.13	0.039
	Chapter 6	13 height	0.50	0.34	-	0.34	1.66	4.16	0.122

Scanner	Study	Region	Thyroid	Bone marrow	Oeso-Phagus	Bone Surface	Brain	Salivary Glands	Effective Dose [mSv]
Accui-tomo 3-D	Chapter 6	Front mandible	0.05	0.06	-	0.06	0.02	0.27	0.013
	Chapter 6	Can. Mandible	0.17	0.04	-	0.04	0.30	0.28	0.026
	Chapter 6	Post. mandible	0.07	0.16	-	0.16	0.03	0.59	0.030
	Chapter 6	Full mandible	0.53	0.46	-	0.46	0.68	2.01	0.108
Mercu Ray	Ludlow <i>et al</i> 2006	Full	6.33	0.692	0.393	3.211	3.967	5.467	0.482
Impla-Graphy	Lee <i>et al</i> 2007	Maxilla	0.826	0.078	0.098	0.361	0.604	2.125	0.078
	Lee <i>et al</i> 2007	mandible	1.290	0.108	0.099	0.500	0.339	2.744	0.105
VCT	Lee <i>et al</i> 2007	Full	1.242	0.335	0.179	1.555	2.121	2.930	0.165
Sensation 16	Chapter 3	Large FOV	6.74	2.96	-	2.83	13.11	14.31	0.927
	Chapter 3	Mandible	5.32	0.84	-	0.74	0.84	9.37	0.423
	Chapter 3	Low dose	1.23	0.30	-	0.29	1.39	1.69	0.119
pano-ramic	Gijbels <i>et al</i> 2005	Panoramic	0.052	0.008	0.001	0.008	0.023	0.328	0.007
Intra-oral	Gijbels <i>et al</i> 2003	Cephalometry	0.08	0	0	0	0.024	0.15	0.005

Table 6.3 continued

6.5.2 Impact on diagnosis and treatment

To conclude our discussion, we describe how and why CBCT for dentomaxillofacial applications can change the treatment for the patients, for example in the area of oral implant placement. Due to the ageing of the population, full or partially edentulism becomes a major problem which can lead to aesthetical, chewing, occlusal and pronunciation problems. Traditionally, dentures were used to overcome these problems. However during the last decades the use of oral implants have proven to be one of the major improvements in the long history of oral rehabilitation (Feine *et al* 2006). These implants are placed during a surgical procedure. As discussed in the introduction, a good preparation of this procedure is necessary to achieve an optimal osseointegration of the implants. For the preparation of such a surgery, preference has gone to the use of 3-D imaging. Before the introduction of the CBCT scanner, the patient needed to get an appointment in a clinic or a radiological practice to acquire a CT of the mouth. Due to the long waiting list, getting such an appoint could take several weeks. With the introduction of CBCT however, it is possible to image the patient during his visit. After the images has been processed, the implantologist can make a first diagnosis and discuss the different treatment options with the patient, which improves communication with the patient. Thanks to this quicker diagnosis, the patient care can be improved considerably.

Because CT scanners exist longer than CBCT one could wonder why dentists did not just install CT scanners in their offices? There are different reasons for this. A first reason is the difference in price between a CBCT and a CT scanner. For example the first version of the i-CAT was available at a price of 155 000 \$ where the cost of a full-service CT scanner was around 1,5 million dollar or more (Kaplowitz 2005). CBCT scanners are becoming cheaper due to increased competition because several companies have launched their CBCT scanner. A second reason is the size of CBCT scanners. A CBCT scanner: a CBCT scanner is more compact than a full-service CT scanner which makes it more easy to install it in a dental office. A third reason is the ease of use and the specialisation of installed software towards dental applications. Finally there is also more comfort to the patient because sitting in a scanner is more comfortable rather than laying down.

Although there are many advantages when using a CBCT scanners in dentomaxillofacial applications one must keep in mind that there are still some disadvantages.

There is no good contrast between soft-tissues and therefore it is not appropriate for the diagnosis of tumours. Although the radiation dose of CBCT is lower than the radiation dose of a standard CT, it is still considerably higher than that of an intra-oral radiograph and because of the high number of radiographs which are acquired in dental applications, one must ensure that there is no overconsumption of CBCT scanners.

Chapter 7

Summary

Recently, an impressive number of cone-beam computed tomography (CBCT) scanners have been introduced that are dedicated to dentomaxillofacial imaging. With a traditional multi-slice computed tomography (MSCT) scanner, several rotations of a gantry on which an X-ray source and an X-ray receptor are mounted, are performed around the patient while the patient moves through the gantry. With a CBCT scanner, an X-ray source and a two-dimensional (2-D) image receptor are mounted on the gantry. In this case, only one rotation of the gantry around the patient is performed. A reconstruction algorithm is performed to calculate a three-dimensional (3-D) volume, based on the acquired image data. Besides being solely used for diagnostic purposes, CBCT and MSCT scanners are gaining increasing importance for presurgical planning and image-guided surgical procedures in the maxillofacial area. 3-D images acquired by these machines can be successfully used for intra-operative navigation and image-guided endosseous dental implant placement. Such applications require a sufficient geometric accuracy of the scans to achieve satisfactory surgical results.

The manufacturers of CBCT scanners promise that these scanners provide 3-D information to the dentomaxillofacial radiologist with a lower radiation dose than conventional MSCT scanners, but with sufficient image quality to be used in image guided endosseous implant placement. To test this hypothesis, both the image quality and the radiation dose were evaluated on one MSCT scanner and four different CBCT scanners: Accuitomo 3D, NewTom 3G, MercuRay CB and i-CAT. These were the four pioneering CBCT scanners for the field of dentomaxillofacial radiology.

(1) The image quality was evaluated based on bone segmentation accuracy, because accurate bone segmentation is a requirement for the use of CBCT scanner in image guided endosseous implant placement.

(2) The radiation dose was evaluated by measuring the effective radiation dose through experiments with a Rando-Alderson phantom and Thermoluminescent Dosimeters. This method was preferred because no standardized technical dose estimate was available and simulations were too time-consuming.

The question about image quality assessment was studied in different steps. In the first step, software was developed which can be used to establish segmentation accuracy of CT scanners automatically. Therefore, the European Spine Phantom (ESP), a semi-anthropomorphic phantom that consists out of a spine with three inserts, was used. This phantom is built with an accuracy of 0.1 mm. A computer model of this phantom was built and aligned with the CT images of the phantom. Thanks to this alignment, measure lines defined on the computer model could be transferred to the CT image and bone thickness at corresponding places could be measured and compared. This software was further developed and optimised for use with more realistic phantoms for dentomaxillofacial imaging.

In the next step the measured bone thickness from mandibles and maxillas derived from bone segmentations in both MSCT and CBCT scanners were compared. The conclusion of this study was that the bone thickness was significantly different. The smallest difference was found for the i-CAT (0.05 ± 0.47 mm) and the largest difference was found for the Accuitomo 3D (1.2 ± 1.0 mm).

To express the absolute accuracy of bone segmentation, a better gold standard needed to be developed. This gold standard was found by scanning a dry skull with a laser scanner. Based on a point cloud derived of the laser scanner, a 3-D volume was calculated. This 3-D volume was matched with the 3-D scans of the dry skull. For the segmentation of the skull, the highest accuracy was achieved for the i-CAT. This accuracy was expressed as the 90th percentile of the absolute difference between the thickness measured on the laser model and the corresponding thickness measured on the CT scan. For the MSCT scanner, this value was 1.22 mm. For the other evaluated CBCT scanners, the accuracy was larger than 3 mm.

In a last test, the accuracy was assessed based on physical phantoms provided with the Accuitomo 3D. The first phantom was a cylinder in PMMA with cylindrical inserts of air, bone and aluminium. The second phantom was a cylinder in PMMA with thin aluminium plates inserts folded in the form of a mushroom. The tests on the first cylindrical phantom taught us that except for the clinical protocol of the Accuitomo 3D, the cylinders could be segmented with an accuracy which is better than 1 mm. The study of the second phantom taught us that the MSCT scanner suffered more from metal artefacts and thus the segmentation accuracy was worse for the MSCT scanner than for the

CBCT scanner. In general, the results on the physical phantoms, showed a better accuracy for the scanners, than the results on the skull phantom.

Based on the study of the radiation dose, one could conclude that the lowest radiation dose was acquired for the Accuitomo 3D with 13 μSv and the highest radiation dose for the Sensation 16 with 927 μSv . But for the Accuitomo 3D, only a small part of the mandible was scanned and for the Sensation 16 the complete head was scanned. For the NewTom 3G the values were between 52 μSv and 178 μSv . For the i-CAT the values ranged between 40 μSv and 180 μSv .

If the combination of radiation dose and image quality is addressed however, one can see that of the evaluated scanners, only the i-CAT holds it promise of providing images with a lower dose but with the possibility to acquire accurate bone segmentations comparable to traditional MSCT scanners. For the assessment of this accuracy, a skull phantom with an accurate geometrical description derived from a laser scanner should preferably be used. While geometric objects seem to allow a good evaluation of segmentation accuracy, more anthropomorphic structures, although essential, cannot be measured nor compared using such geometric objects.

Chapter 8

Samenvatting

Onlangs zijn een indrukwekkend aantal cone-beam computed tomography (CBCT) scanners geïntroduceerd die gespecialiseerd zijn in dentomaxillofaciale beeldvorming. Met een traditionele multi-slice computed tomography (MSCT) scanner, worden enkele rotaties van een portaal waarop een X-stralenbron en een x-stralenontvanger zijn gemonteerd, uitgevoerd rond de patiënt terwijl de patiënt door het portaal beweegt. Met een CBCT scanner, zijn een x-stralenbron en een twee-dimensionale (2-D) beeldontvanger gemonteerd op het portaal. In dit geval wordt slechts één rotatie van het portaal rond de patiënt uitgevoerd. Een reconstructiealgoritme wordt uitgevoerd voor de berekening van een drie-dimensionaal (3-D) beeldvolume op basis van de verkregen beeldgegevens. CBCT en MSCT scanners worden niet alleen meer gebruikt voor diagnostische taken, maar ze worden ook steeds belangrijker voor prechirurgische planning en beeldgeleide chirurgische procedures in het dentomaxillofaciale gebied. 3-D beelden verkregen door deze machines kunnen gebruikt worden voor intra-operatieve navigatie en beeldgeleide operaties waarin orale implantaten geplaatst worden. Dergelijke toepassingen vereisen een voldoende geometrische nauwkeurigheid van de scans om op deze manier een geslaagde operatie te bereiken.

De fabrikanten van CBCT scanners beloven dat deze scanners 3-D informatie genereren voor de dentomaxillofaciale radioloog met een lagere stralingsdosis dan de conventionele MSCT scanners, maar met voldoende kwaliteit zodat ze gebruikt kunnen worden in beeldgebaseerde operaties voor het plaatsen van orale implantaten.

Om deze hypothese te testen, werden zowel de beeldkwaliteit en de stralingsdosis geëvalueerd op een MSCT scanner en vier verschillende CBCT scanners: de Accuimo 3-D, de NewTom 3G, de MercuRay CB en de i-CAT. Dit waren de vier pioniers van CBCT scanners voor de dentomaxillofaciale radiologie.

(1) De beeldkwaliteit werd geëvalueerd op basis van de nauwkeurigheid van de botsegmentatie in deze beelden. Een nauwkeurige botsegmentatie is een vereiste voor het gebruik van de CBCT scanner in beeldgeleide operaties voor het plaatsen van orale implan-

taten.

(2) De stralingsdosis werd geëvalueerd door het meten van de effectieve stralingsdosis door middel van experimenten met het Rando-Alderson fantoom en thermoluminescente dosimeters. Deze methode genoot de voorkeur omdat er geen gestandaardiseerde technische dosis schatting beschikbaar was en simulaties te veel tijd in beslag nemen.

De vraag over de beoordeling van de nauwkeurigheid werd onderzocht in verschillende stappen. In de eerste stap, werd de software ontwikkeld die gebruikt wordt voor het automatisch evalueren van de segmentatienauwkeurigheid van CT scanners. Daarvoor werd het European Spine Phantom (ESP), een semi-anthropomorfisch fantoom dat bestaat uit een simulatie van een menselijke ruggengraat, gebruikt. Dit fantoom is gebouwd met een nauwkeurigheid van 0,1 mm. Een computermodel van dit fantoom werd gebouwd en geregistreerd met de CT-beelden van het fantoom. Dankzij deze registratie kunnen meetlijnen die gedefinieerd zijn in het computermodel overgedragen worden naar het CT-beeld en kunnen botdiktes op overeenkomstige plaatsen worden gemeten en vergeleken. Deze software werd verder ontwikkeld en geoptimaliseerd voor gebruik met meer realistische fantomen voor de dentomaxillofaciale beeldvorming.

In de volgende stap werden botdiktes gemeten op kaken gescand met CBCT scanners en MSCT scanners met elkaar vergeleken. De conclusie van deze studie was dat de dikte van het bot significant verschillend was als overeenkomstige diktes werden gemeten op de twee verschillende soorten beelden. Het kleinste verschil werd gevonden voor de i-CAT ($0,05 \pm 0,47$ mm) en het grootste verschil werd gevonden voor de Accuitomo 3D ($1,2 \pm 1,00$ mm).

Om de absolute nauwkeurigheid van botsegmentatie weer te geven, moest een betere gouden standaard ontwikkeld worden. Deze gouden standaard werd vastgesteld door het scannen van een droge schedel met een laser scanner. Gebaseerd op een puntenwolk afkomstig van de laser scanner, werd een 3-D volume berekend. Dit 3-D volume werd geregistreerd aan de 3-D scans van de schedel. De hoogste segmentatienauwkeurigheid werd bereikt met de i-CAT scanner. Deze nauwkeurigheid is uitgedrukt in de 90e percentiel van de absolute verschil tussen de dikte gemeten op de laser model en de overeenkomstige dikte gemeten op de CT-scan. Voor de MSCT scanner was deze waarde 1,22 mm. Voor de andere geëvalueerde CBCT scanners, werden nauwkeurigheden tot 3 mm gevonden.

In een laatste test werd de nauwkeurigheid beoordeeld op basis van fysische fantomen die geleverd werden bij de Accuitomo 3D. Het eerste fantoom was een cilinder in PMMA met cilindrische structuren van lucht-, bot-en aluminium in verwerkt. Het tweede fantoom was een cilinder in PMMA met dunne aluminium gevouwen platen in de vorm van een paddestoel in verwerkt. De proeven op het cilindrisch fantoom leerden ons dat met uitzondering van het klinische protocol van de Accuitomo 3D, de cilinders kunnen worden gesegmenteerd met een nauwkeurigheid die beter is dan 1 mm. De studie van het tweede fantoom leerde ons dat de MSCT scanner meer last heeft van metaalartefacten en bijgevolg is de segmentatienauwkeurigheid slechter voor de MSCT scanner dan voor de CBCT scanner voor structuren met een hoge densiteit. In het algemeen werden er op de fysische fantomen, bleek een betere segmentatienauwkeurigheid bekomen dan met het schedelfantoom.

Gebaseerd op de studie van de stralingsdosis, kan men concluderen dat de laagste stralingsdosis werd bekomen door de Accuitomo 3D met 13 μSv en de hoogste dosis straling voor de Sensation 16 met 927 μSv . Maar voor de Accuitomo 3D, wordt slechts een klein deel van de onderkaak gescand en voor de Sensation 16 werd het volledige hoofd gescand. Voor de NewTom 3G lagen de waarden tussen 52 en 178 μSv . Voor de i-CAT lagen de waarden tussen 40 μSv en 180 μSv .

Als men de stralingsdosis en de beeldkwaliteit combineert is echter te zien dat van de geëvalueerde scanners, alleen de i-CAT de belofte waarmaakt van het leveren van beelden met een lagere dosis maar met de mogelijkheid tot het verwerven van accurate botsegmentatie vergelijkbaar met de traditionele MSCT scanners. Voor de beoordeling van de juistheid van de segmentatie van het schedelbot, wordt bij voorkeur een fantoom met een nauwkeurige geometrische beschrijving, afkomstig van een laserscanner gebruikt. Hoewel geometrische objecten zeer goed dienen voor het bepalen van de segmentatienauwkeurigheid, missen zij de evaluatiemogelijkheden voor vergelijkende antropomorfe studies.

References

- Aamodt A, Kvistad KA, Andersen E, Lundlarsen J, Eine J, Benum P, Husby OS 1999 Determination of the Hounsfield value for CT-based design of custom femoral stems. *J Bone Joint Surg Br* **81** 143-144
- Alaei P, Gerbi B, Geise R 2000 Evaluation of model-based treatment planning system for dose computations in the kilovoltage energy range. *Med Phys* **12** 2821-2282
- Alspaugh JD, Answer to Question # 6578 Submitted to "Ask the Experts" Category Medical and Dental Equipment/Shielding equipment
<http://www.hps.org/publicinformation/ate/q6578.html>
- Arai Y, Honda K, Iwai K, Shinoda K 2001 Practical model « 3DX » of limited cone-beam X-ray CT for dental use. *Int Congr Ser* **1230** 713-718
- Araki K, Maki K, Seki K, Sakamaki K, Harata Y, Sakaino R, Ikano T, Seo K 2004 Characteristics of a newly developed dentomaxillofacial X-ray cone beam CT scanner (CB MercuRay): system configuration and physical properties. *Dentomaxillofac Radiol* **33** 51-59
- Aroua A, Buchillier-Decka I, Dula K, Nedjadi Y, Perrier M, Vader J-P, Valley J-F 2004 Radiation exposure in dental radiology: a 1998 nationwide survey in Switzerland. *Dentomaxillofac Radiol* **33** 211-219
- Baillard C, Barillot C 2000 Robust 3D segmentation of anatomical structures with level sets. *LNCS* **1935** 236-244
- Beutel J, Kundel H L, Van Metter R L, Handbook of medical imaging. Volume physics and psychophysics. SPIE PRESS Bellingham, Washington US ISBN 0-8194-3621-6
- Brenner DJ, Doll R, Goodhead DT, Hall EJ, Land CE, Little JB, Lubin JH, Preston DL, Preston RJ, Puskin JS, Ron E, Sachs RK, Samet M, Setlow RB and Zaider MZ 2003 Cancer risks assessment to low doses of ionizing radiation: Assessing what we really know. *PNAS* **100** 13761-13766
- Cahill DR, Orland MJ 1984 Atlas of human cross-sectional anatomy Lea and Febiger Philadelphia ISBN/ISSN 0-8121-0890-6
- Carlsson CA 1999 Imaging modalities in x-ray computerized tomography and in selected volume tomography. *Phys Med Biol* **24** 430-439
- Cavalcanti M P G, Yang J, Ruprecht A, Vannier M W 1999 Accurate Linear Measurements in the anterior maxilla using orthoradially reformatted spiral computed tomography. *Dentomaxillofac Radiol* **28** 137-140
- Cavalcanti MPG, Rocha SS, Vannier MW 2004 Craniofacial measurements based on 3D-CT volume rendering: implications for clinical applications. *Dentomaxillofac Radiol* **33** 170-176
- Chiarot CB, Siewerdsen JH, Haycocks T, Moseley DJ, Jaffray DA 2005 An innovative phantom for quantitative and qualitative investigation of advanced x-ray imaging technologies. *Phys Med Biol* **50** N287-298
- Cohnen M, Kemper J, Möbes, Pawelzik J, Möbes, Pawelzik J, Mödder U 2002 Radiation dose in dental radiology. *Eur Radiol* **12** 634-637
- De Groeve P, Schutyser F, Van Cleynenbreugel J, Suetens P 2001 Registration of 3D photographs with spiral CT images for soft tissue simulation in maxillofacial surgery. In: Proceedings of the Fourth International Conference on Medical Image Computing and

Computer-assisted Intervention (MICCAI 2001), 14–17 October, Utrecht, The Netherlands **2208** 991–996

- De Man B, Nuyts J, Dupont P, Marchal G, Suetens P 1999 Reduction of metal streak artefacts in X-ray computed tomography: a simulation study. *IEEE Trans Nucl Sci* **46** 691–696
- Dempster AP, Laird NM, Rubin DB 1976 Maximum likelihood from incomplete data via the EM algorithm. *J R Stat Soc* **3** 1–38
- Dixon RL 2003 A new look of CT dose measurement: beyond CTDI. *Med Phys* **30** 1272–1280
- Dixon RL, Munley MT, Bayram E 2005 An improved analytical model for CT dose simulation with a new look at the theory of CT dose. *Med Phys* **32** 3712–3719
- Dixon RL 2006 Restructuring CT dosimetry- A realistic strategy for the future Requiem for the pencil chamber. *Med Phys* **33** 3973–3976
- Egger G, Korb W, Welzel T, Daüber S, Marmulla R, Hassfeld S 2005 The accuracy of CT based craniofacial models for robotic surgery. *Proceedings Surgetica*. 2005 399–404
- Endo M, Tsunoo T, Nakamori N, Yoshida K 2001 Effect of scattered radiation on image noise in cone beam CT. *Med Phys* **28** 469–474
- Feine J, Jacobs R, Lobbezoo F, Sessle BJ, van Steenberghe D, Trulsson M, Fejerskov O, Svensson P 2006 A functional perspective on oral implants – state-of-the-science and future recommendations *J Oral Rehabil* **33** 309–312
- Gahleitner A, Watzek G, Imhof H. 2003 Dental CT imaging technique, anatomy, and pathologic conditions of the jaws. *Eur Radiol* **13** 366–376
- Gijbels F, Sanderink G, Wyatt J, Van Dam J, Nowak B, Jacobs R 2003 Radiation doses of collimated vs non-collimated cephalometric exposures. *Dentomaxillofac Radiol* **32** 128–133
- Gijbels F, Jacobs R, Sanderink G, De Smet E, Nowak B, Van Dam J, van Steenberghe D 2002 A comparison of the effective dose from scanography with periapical radiography *Dentomaxillofac Radiol* **31** 159–163.
- Gijbels F, Jacobs R, Bogaerts R, Debaveye D, Verlinden S, Sanderink G 2005 Dosimetry of digital panoramic imaging. Part I: patient exposure. *Dentomaxillofac Radiol* **34** 145–149
- Golikov VY, Nikitin VV 1989 Estimation of the mean organ doses and the effective dose equivalent from Rando phantom measurements. *Health Phys* **56** 111–115
- Guerrero ME, Jacobs R, Loubele M, Schutyser F, Suetens P, van Steenberghe D 2006 State-of-the-art on Cone beam CT imaging for preoperative planning for implant placement. *Clin Oral Investig* **10** 1–7
- Hagtvedt T, Aaløkken T, Nøttgheden J, Kolbenstvedt A 2003 A new low-dose CT examination compared with standard-dose CT in the diagnosis of acute sinusitis. *Eur Radiol* **12** 976–980
- Hein E, Rogalla P, Randolph K, Hamm B 2002 Low-dose CT of the paranasal sinuses with eye lens protection: effect on image quality and radiation. *Eur Radiol* **12** 1693–1696
- Herkströter FM, Ten Bosch JJ 1990 Wavelength-independent microradiography: A method for non-destructive Quantification of Enamel and Dentin Mineral Concentrations using Polychromatic X-rays. *J Dent Res* **69** 1522–1526
- Hsieh J, Molthen RC, Dawson CA, Johnson RH 2000 An iterative approach to the beam hardening correction in cone beam CT. *Med Phys* **27** 23–26

- Hubbel JH, Seltzer SM 1996 Table of X-Ray Mass Attenuation Coefficients and Mass Energy-Absorption Coefficients Physics Laboratory Reference Data National Institute of Standards and Technology <http://physics.nist.gov/PhysRefData/XrayMassCoef/>
- Huda W, Sandison GA 1984 Estimation of mean organ doses in diagnostic radiology from Rando phantom measurements *Health Phys* **47** 463-467
- ICRP Publication 60 Radiation Protection. 1990 recommendations of the International Commission on Radiological Protection. Ann ICRP 1991; 21
- ICRP 2007 Recommendations of the International Commission on Radiological Protection ICRP
- Ibánñez L, Schroeder W and the Insight Consortium 2003 NLM Insight segmentation and registration toolkit Kitware Inc ISBN 1-930934-10-6
- Imhof H, Czerny C, Dirisamer A 2003a Head and neck imaging with MDCT. *Eur J Radiol* **45** S23-S31
- Imhof H, Schibany N, Ba-Salamah A, Czerny C, Hojreh A, Kainberger F, Krestan C, Kudler H, Nöbauer I, Nowotny R 2003b Spiral CT and radiation dose. *Eur J Radiol* **47** 29-37
- Kalender WA, Felsenberg D, Genant HK, Fischer M, Dequeker J, Reeve J 1995 The European Spine Phantom—a tool for standardization and quality control in spiral bone mineral measurements by DX and QCT. *Eur J Radiol* **20** 83-92
- Kang Y, Engelke K, Kalender WA 2003 A new accurate and precise 3-D segmentation method for skeletal structures in volumetric CT Data. *IEEE TMI* **22** 586-598
- Kaplowitz G, Cone Beam CT: an interview with the president of i-CAT Osseonews Saturday, June 18th 2005
- Kau CH, Richmond S, Palomo JM and Hans MG 2005 Current Products and Practice Three-dimensional cone beam computerized tomography in orthodontics *J Orthod* **32** 282-293
- Kobayashi K, Shimoda S, Nakagawa Y, Yamamoto A. 2004 Accuracy in Measurements of Distance Using Limited Cone-Beam Computerized Tomography. *Int J Oral Maxillofac Implants* **19** 228-231
- Lascala CA, Pamella JH, Marques MM 2004 Analysis of the accuracy of linear measurements obtained by cone beam computed tomography (CBCT-NewTom). *Dentomaxillofac Radiol* **33** 291-293
- Lee J-N, Han W-J, Kim E-U 2007 Absorbed and effective dose from newly developed cone beam computed tomography in Korea *Korean J Oral Maxillofac Radiol* **37** 93-102
- Lehr JL 1983 Truncated view artefacts: clinical importance on CT *Am J Roentgenol* **141** 183-191
- Leitz W, Axelsson B, Szendrő G 1995 Computed tomography dose assessment – a practical approach. *Radiat Prot Dosimetry* **57** 377-380
- Lorensen W, Cline H. 1987 Marching cubes: a high resolution 3d surface construction algorithm. *Proceedings SIGGRAPH* 163-169
- Loubele M, Jacobs R, Maes F, Schutyser F, Debaveye D, Bogaerts R, Coudyzer W, Vandermeulen D, Van Cleynenbreugel K, Marchal G and Suetens P 2005 Radiation dose versus image quality for low-dose CT protocols of the head for maxillofacial surgery and oral implant planning *Radiat Prot Dosimetry* **117** 211-216
- Loubele M, Maes F, Schutyser F, Marchal G, Jacobs R, Suetens P 2006 Assessment of bone segmentation quality of cone-beam CT versus multi-slice spiral CT: a pilot study *Oral Surg Oral Med Oral Pathol Oral Radiol Endod* **102** 225-234

- Loubele M, Maes F, Vandermeulen D, Denis K, Jacobs R, White SC, van Steenberghe D, Van Bael A, Loeckx D, Lambrichts I, Suetens P 2006 Assessment of bone segmentation quality of CT scanners using laser scanning, *Int J Comput Assist Radiol Surg* **1** supplement 400-402
- Ludlow JB, Davies-Ludlow, LE, Brooks SL 2003 Dosimetry of two extraoral direct digital imaging devices: NewTom cone beam CT and Orthophos Plus DS panoramic unit. *Dentomaxillofac Radiol* **32** 229-243
- Ludlow JB, Davies-Ludlow L, Brooks S, Howerton W 2006 Dosimetry of 3 CBCT devices for oral and maxillofacial radiology: CB Mercuray, NewTom 3G and i-CAT *Dentomaxillofac Radiol* **35** 219-226
- Ludlow JB, Laster WS, See M, Baily LJ, Hershey HG 2007 Accuracy of measurements of mandibular anatomy in cone beam computed tomography images *Oral Surg Oral Med Oral Pathol Oral Radiol Endod* **103** 534-542
- Maes F, Collignon A, Vandermeulen D, Marchal G and Suetens P 1997 Multi-modality image registration by maximization of mutual information *IEEE TMI* **16** 187-198
- Marmulla R, Wörtche R, Mühling J, Hasffeld S 2005 Geometric Accuracy of the NewTom 9000 Cone Beam CT. *Dentomaxillofac Radiology* **34** 28-31
- McNitt-Gray M F 2002 AAPM/RSNA Tutorial for residents: Topics in CT. Radiation dose in CT. *Radiographics* **22** 1541-1553
- Mischkowski RA, Pulsfort R; Ritter L, Neugebauer J, Brochhagen HG, Keeve E, Zöller JE 2007 Geometric accuracy of a newly developed cone-beam device for dentomaxillofacial imaging *Oral Surg Oral Med Oral Pathol Oral Radiol Endod* **104** 551-559
- Mori S, Endo M, Nishizawa K, Tsunoo T, Aoyama T, Fujiwara H, Murase K 2005 Enlarged longitudinal dose profiles in cone-beam CT and the need for modified dosimetry *Med Phys* **32** 1061-9
- Mori S, Nishizawa K, Ohno M, Endo M 2006 Conversion factor for CT dosimetry to assess patient dose using a 256-slice CT scanner *Br J Radiol* **79** 888-892
- Mozzo P, Procacci C, Tacconi A, Tinazzi Martini P, Bergamo and Andreis I A 1998 A new volumetric CT machine for dental imaging based on the cone-beam technique preliminary results. *Eur Radiol* **8** 1558-1564
- NHS Purchasing and Supply Agency November 2005 Siemens Somatom Sensation Open CT scanner technical evaluation Report 05071
- Pinsky HM, Dyda S, Pinsky W, Misch KA, Sarment DP 2006 Accuracy of three-dimensional measurements using cone-beam CT. *Dentomaxillofac Radiol* **35** 410-416.
- Prevrhal S, Engelke K, Kalender WA 1999 Accuracy Limits for the determination of cortical width and density: the influence of object size and CT imaging parameters. *Phys Med Biol* **44** 751-764
- Scarfe WC, Farman AG, Sukovic P 2006 Clinical applications of cone-beam computed tomography in dental practice *J Can Dent Assoc* **72** 75-80
- Schulze D, Heiland M, Thurmann H, Rother UJ (2004) Radiation exposure during midfacial imaging using 4- and 16-slice computed tomography, cone beam computed tomography systems and conventional radiography. *Dentomaxillofac. Radiol.* **33** 83-86
- Schutyser F, Van Cleynenbreugel J, Ferrant M, Schoenaers J and Suetens P 2000 Image-based 3D planning of maxillofacial distraction procedures including soft tissue implication. Proceedings of 3rd Computing and Computer-Assisted Intervention (MICCAI 2000), Pittsburgh, PA 11-14 October. *LNCS* **1935** 999-1007

- Sebastian TB, Tek H, Crisco JJ, Kimia BB 2003 Segmentation of carpal bones from CT images using skeletally coupled deformable models. *Medical Image Analysis* **7** 21-24.
- Seppi E J, Munro P, Johnsen S W, Shapiro E G, Tognina C, Dan Jones M, Pavkovich J M, Webb C, Mollov I, Partain L D, Colbeth R E 2003 Megavoltage cone-beam computed tomography using a high-efficiency image receptor *Int J Radiation Oncology Biol Phys* **55** 793-803
- Shannoun F, Zeeb H, Back C, Blettner M 2006 Medical exposure of the population from diagnostic use of ionising radiation in Luxembourg between 1994 and 2002. *Health Phys* **91** 154-162
- Struelens L 2005 Optimization of patient doses, linked to image quality in vascular radiology Doctoraatsproefschrift, VUB
- Suetens P 2002 Fundamentals of Medical Imaging Cambridge: Cambridge University Press (2002), ISBN 0-521-80362-4
- Sukovic P 2003 Cone beam computed tomography in craniofacial imaging *Orthod Craniofac Res* **6** Suppl 1:31-36; discussion 179-182
- Tskiklakis K, Donta C, Gavala S, Karayianni K, Kamenopoulou V, Hourdakakis C 2005 Dose reduction in maxillofacial imaging using low dose Cone Beam CT *Eur J Radiol* **56** 413-417
- United Nations Scientific Committee on the Effects of Atomic Radiation (UNSCEAR). 2000 Report to the General Assembly, with Scientific Annexes, Volume I: Sources, United Nations Publication, ISBN 92-1-142238-8
- Van Cleynenbreugel J, Haven F, Maes F, Smet M-H, Marchal G, Suetens P 1995 An image registration based approach to assess the geometrical accuracy obtainable from spiral CT imaging the European Spine Phantom. presented at 3rd International Workshop on Rapid Prototyping in Medicine & Computer Assisted Surgery, Erlangen, Germany, October 19-21, 1995
- Van Cleynenbreugel J, Nuyts J, Verbeeck R, Smet M, Marchal G, Suetens P 1997 On the problem of validating computer assisted medical image interpretation. In: Contemporary perspective of validating computer assisted medical image interpretation, Contemporary perspectives in three-dimensional biomedical imaging. Amsterdam: IOS Press 1997 p.311-316
- van Steenberghe D, Naert I, Andersson M, Brajonovic I, Van Cleynenbreugel J, Suetens P 2002 A custom template and definitive prosthesis allowing immediate implant loading in the maxilla: a clinical report *Int J Oral Maxillofac Implants* **17** 663-670
- Verstreken K, Van Cleynenbreugel J, Marchal G, Naert I, Suetens P, van Steenberghe D 1996 Computer-assisted planning of oral implant surgery. An approach using virtual reality *Int J Oral Maxillofac Implants* **11** 806-810
- Verstreken K 2003 Computer-assisted oral implant surgery: a generic concept Proefschrift voorgedragen tot het behalen van het doctoraat in de medische wetenschappen, Departement Parodontologie, Departement Elektrotechniek, K.U.Leuven, October 2003, Leuven, Belgium
- Wiemker R, Zwartkruis A 2001 Optimal Thresholding for 3D Segmentation of Pulmonary Nodules in High Resolution CT. in *Proceedings of CARS 2001*. Amsterdam, the Netherlands Elsevier Publishers, 653-658
- West J, Fitzpatrick JM, Wang MY, Dawant BM, Maurer CR, Kessler RM, et al. 1997 Comparison and evaluation of retrospective intermodality brain image registration techniques. *J Comput Assist Tomogr* **21** 554-566

Curriculum Vitae

Miet Loubele was born on September 5th 1979 in Genk. She completed secondary school in 1997 at Onze-Lieve-Vrouwyceum in Genk (Sciences-Mathematics). In 2002 she graduated with distinction as an engineer in computer sciences at the Katholieke Universiteit Leuven. Afterwards, she joined the Medical Image Computing group of the Katholieke Universiteit Leuven under supervision of prof. Paul Suetens. She also started with a PhD research project in the field of dentomaxillofacial radiology under supervision of professor Reinhilde Jacobs of the Oral Imaging Center of the KULeuven, prof. Paul Suetens and Robert Hermans of the Radiology Departement of Gasthuisberg Leuven. She received the Dentomaxillofacial Research award at the 16th International Congress of Dentomaxillofacial Radiology in Beijing, China (2007). She published a number of papers in national and international journals and presented papers at different national and international meetings. Recently she started working at the research group ELECTA of the KULeuven.

List of Publications

International Journals

- S. De Greef, P. Claes, W. Mollemans, M. Loubele, D. Vandermeulen, P. Suetens, G. Willems, *Semi-automated ultrasound facial soft tissue depth registration : method and validation*, Journal of Forensic Sciences, vol. 50, no. 6, pp. 1282-1288, November 2005
- M.E. Guerrero, R. Jacobs, M. Loubele, F. Schutyser, P. Suetens, D. van Steenberghe, *State-of-the-art on cone beam CT imaging for preoperative planning of implant placement*, Clinical Oral Investigations, vol. 10, no. 1, pp. 1-7, March 2006
- M. Loubele, R. Jacobs, F. Maes, F. Schutyser, D. Debaveye, R. Bogaerts, W. Coudyzer, D. Vandermeulen, J. Van Cleynenbreugel, G. Marchal, P. Suetens, *Radiation dose vs. image quality for low-dose CT protocols of the head for maxillofacial surgery and oral implant planning*, Radiation protection dosimetry, vol. 117, no. 1-3, pp. 211-216, March 14, 2006 (International workshop on optimisation of dose and performance in interventional and digital imaging- DIMOND III, March 25-27, 2004, Leuven, Belgium)
- M. Loubele, F. Maes, F. Schutyser, G. Marchal, R. Jacobs, P. Suetens, *Assessment of bone segmentation quality of cone-beam CT versus multislice spiral CT : a pilot study*, Oral Surgery Oral medicine Oral Pathology Oral radiology and Endodontics, vol. 102, no. 2, pp. 225-234, August 2006
- M. Loubele, N. Van Assche, K. Carpentier, F. Maes, R. Jacobs, D. van Steenberghe, P. Suetens, *Comparative localized linear accuracy of small field cone-beam CT and multislice CT for alveolar bone measurements on an ex-vivo upper jaw bone*, Oral Surgery Oral Medicine Oral Pathology Oral Radiology and Endodontics, vol. 105, no. 4, pp. 512-518
- M. Loubele, F. Maes, D. Vandermeulen, K. Denis, R. Jacobs, S.C. White, D. van Steenberghe, A. Van Bael, D. Loeckx, I. Lambrechts, P. Suetens, *Assessment of bone segmentation quality of CT scanners using laser scanning*, International Journal of Computer Assisted Radiology and Surgery, vol. 1 supplement, pp. 400-402, June 2006 (20th

international congress and exhibition on computer assisted radiology and surgery - CARS 2006, June 28 - July 1, 2006, Osaka, Japan)

- M. Loubele, M.E. Guerrero, R. Jacobs, P. Suetens, D. van Steenberghe, *A comparison of jaw dimensional and quality assessments of bone characteristics with cone-beam CT, spiral tomography, and multi-slice spiral CT*, International Journal of Oral & Maxillofacial Implants, vol. 22, no. 3, pp. 446-454, May/June 2007
- M. Loubele, F. Maes, R. Jacobs, D. van Steenberghe, SC White, P. Suetens, *Comparative study of image quality for MSCT and CBCT scanners for dentomaxillofacial radiology applications* Radiation Protection Dosimetry 2008 Jun 26 [ahead of print], vol. 129, 222-6.
- M. Loubele, R. Bogaerts, E. Van Dijck, R. Pauwels, S. Vanheusden, P. Suetens, G. Marchal, G. Sanderink, R. Jacobs, *Comparison between effective radiation dose of CBCT and MSCT scanners for dentomaxillofacial applications* Eur J Radiol Jul 16 [ahead of print]

International journal abstracts

- M. Loubele, N. Van Assche, K. Carpentier, W. Coudyzer, F. Maes, R. Jacobs, D. van Steenberghe, G. Marchal, P. Suetens, *CBCT compared to MSCT regarding linear measurements on ex-vivo upper jaw bone*, Oral Surgery Oral Medicine Oral Pathology Oral Radiology and Endodontics, vol. 101, no. 1, pp. E8-E9, January 2006 (American Academy of Oral & Maxillofacial Radiology 56th annual session, November 16-20, 2005, Charleston, South Carolina, USA)

International Conference published in proceedings

- D. Vandermeulen, M. Loubele, P. Claes, Q. Wang, W. Mollemans, S. Srivastava, S. De Greef, G. Willems, P. Suetens, *Low-dose CT based soft tissue modeling for craniofacial reconstruction*, Facial Reconstruction - Gesichtsrekonstruktion, proceedings 2nd international conference on reconstruction of soft facial parts - RSFP 2005, pp. 127-140, March 17-18, 2005, Remagen, Germany

International Conference: abstract or not published

- M.E. Guerrero, M. Loubele, R. Jacobs, X. Liang, F. Maes, P. Suetens, D. van Steenberghe, *Analisis comparativo de la calidad osea subjetiva entre cone beam CT, tomografía computarizada multislice y tomografía espiral*, 6th Latin American meeting of dental maxillofacial radiology, April 26 - May 1, 2006, Santiago, Chile
- M. Loubele, R. Jacobs, S. White, F. Maes, K. Denis, I. Lambrichts, D. van Steenberghe, P. Suetens *Accuracy of linear measurements on the lower jaw in CBCT based on a ground-truth acquired with laser scanning : preliminary results*, 10th European Congress of Dentomaxillofacial Radiology, pp. 70, May 31 - June 3, 2006, Leuven, Belgium
- M. Loubele, R. Bogaerts, S. White, R. Jacobs, H. Bosmans, G. Sanderink, P. Suetens, *Evaluation of dose measurement protocols for cone-beam CT scanners*, 10th European Congress of Dentomaxillofacial Radiology, pp. 132, May 31 - June 3, 2006, Leuven, Belgium
- S. Yi, B. De Dobbelaer, O. Nackaerts, M. Loubele, P. Suetens, R. Jacobs, *Development of a preoperative bone quality assessment tool using digital 2D and 3D : decision of design parameters*, 10th European Congress of Dentomaxillofacial Radiology, pp. 113, May 31 - June 3, 2006, Leuven, Belgium

- M. Loubele, R. Jacobs, R. Bogaerts, F. Maes, SC. White, D. van Steenberghe, P. Suetens, *Image quality versus radiation dose of four different CBCT scanners*, Abstractbook 16th International Congress of Dentomaxillofacial radiology, pp. 59, June 26-30, 2007, Beijing, China (winner of IADMFR Maxillofacial Imaging Research Award 2007)
- M. Loubele, W. Mollemans, D. Debaveye, F. Maes, R. Bogaerts, D. Vandermeulen, J. Van Cleynenbreugel, R. Jacobs, G. Marchal, P. Suetens, *Radiation dose versus image quality for low-dose CT-protocols of the head for maxillofacial surgery and oral implant planning*, 4th National Day on Biomedical Engineering, October 22, 2004, Brussels, Belgium

Internal reports

- M. Loubele, F. Maes, R. Jacobs, P. Suetens, SC. White, *Comparative study of image quality for MSCT and CBCT scanners for dentomaxillofacial radiology applications*, Internal report KUL/ESAT/PSI/0701, K.U.Leuven, ESAT, January 2007, Leuven, Belgium
- M. Loubele, R. Bogaerts, S.C. White, F. Maes, H. Bosmans, G. Sanderink, R. Jacobs, W. Coudyzer, G. Marchal, P. Suetens, *Comparative study of image quality and radiation dose of MSCT and CBCT scanners in dentomaxillofacial radiology*, Internal report KUL/ESAT/PSI/0703, K.U.Leuven, ESAT, February 2007, Leuven, Belgium